Postseismic deformation modelling constrained by geodetic and seismic data in central Chile: Implications for lower-crustal rheology

Carlos Peña Hormazábal

Fachbereich Geowissenschaften
Freie Universität Berlin

Dissertation zur Erlangung des akademischen Doktorgrades
"Doctor rerum naturalium" (Dr. rer. nat.)

October 2020

Primary advisor:	Prof. Dr. Onno Oncken[1,2]
Co-advisor:	PD. Dr. Oliver Heidbach[2,3]
Day of disputation:	February 5, 2021

---

[1] Department of Earth Sciences, Freie Universität Berlin, Berlin, Germany

[2] Helmholtz-Centre Potsdam - Deutsches GeoForschungsZentrum GFZ, Potsdam, Germany

[3] Geophysical Institute of the Karlsruhe Institute of Technology KIT, Karlsruhe, Germany

I would like to dedicate this thesis to my loving parents …

Abstract

Spatial and temporal measurements from satellite geodesy observations provide fundamental constraints for investigating the mechanisms that control earthquake-related processes over the seismic cycle. The surface motions, in particular those time-dependent observed following large earthquakes (in the postseismic period), can be used to examine both the frictional behaviour of the fault and the rheological properties in the lithosphere-asthenosphere system by means of geomechanical models. During the postseismic period, afterslip on the fault interface and viscous relaxation in the lithosphere-asthenosphere system are the dominant mechanisms. However, the relative contribution of these processes is not entirely understood, which is primarily due to the challenge of modelling the rheological behaviour of the lithosphere-asthenosphere system following megathrust earthquakes. Accordingly, models of the postseismic period have commonly assumed the whole crust as an elastic material above a viscoelastic upper mantle with linear or non-linear (viscosity) rheology.

In this dissertation, I integrate state-of-the-art geomechanical-numerical models, Global Positioning System (GPS) observations, and aftershock seismicity to investigate the underlying deformation processes controlling the postseismic deformation induced by the 2010 M_w 8.8 Maule earthquake in Chile. I particularly focus on investigating the fundamental discrepancies in the resulting postseismic deformation between linear and power-law rheologies. In contrast to previous works, I use, for the first time, a forward model considering temperature-dependent power-law rheology. Furthermore, I implement a novel approach to discriminate competing postseismic simulations, which incorporates the positive correlation between afterslip and aftershock activity. The resulting stresses from the coseismic and postseismic deformation transferred to the northern segment of the 2010 event rupture area, where the M_w 8.4 Illapel earthquake occurred in 2015, are also studied.

The geomechanical-numerical models consider constitutive equations to simulate the elastic and viscous rock responses of the crust and upper mantle. For the power-law rheology case, the spatial and temporal viscous distributions are modulated by the dislocation creep parameters and the temperature field in the crust and upper mantle. On the other hand, the linear rheology case consists of a material with homogeneous and linear viscosity in the upper mantle, while the whole crust is fully elastic. I employ the Finite Element Method (FEM) to solve the involved partial differential equations, for discrete elements representing the study area. The GPS observations and aftershock seismicity consist of published data spanning six years after the 2010 Maule event.

By using a two-dimensional (2D) model approach, my results reveal crucial variations in the modelled surface postseismic displacements due to the choice of model rheology. When comparing these results with the GPS data, I find that the GPS displacement patterns are notably better explained by the power-law rheology model, particularly the six-years cumulative uplift in the volcanic arc and the high-rate transient displacements in the first two years following the mainshock. The primary deviations in the cumulative patterns are produced because of the location of the viscous relaxation. In the linear rheology case, most of the viscous relaxation occurs in the continental mantle wedge, beneath the forearc. Conversely, in the power-law rheology case, the viscous relaxation mainly occurs in the lower crust, beneath the volcanic arc, due to dislocation creep processes.

In a subsequent study, I extend the 2D model approach to 3D. Here, I choose the preferred postseismic simulation from an innovative approach that accounts not only for the best fit to the GPS observations, but also incorporates the spatial correlation between inverted afterslip distributions and aftershock activity. My results reveal that afterslip inversions strongly depend on the choice of rheology, especially at greater depths (> 60 km depths). I also show that a simulation that exhibits non-linear viscous relaxation, in the continental lower crust, considerably reduces the deep afterslip, which is in agreement with observations of relatively less aftershock moment release and the apparent lack of interseismic locking, at greater depths along the plate interface. Conversely, the linear rheology case results in large afterslip at greater depths. Similar to the 2D model outcomes, I favour a 3D simulation in which non-linear viscous relaxation mostly occurs in the continental lower crust and, to a lesser extent, in the continental upper mantle beneath the volcanic arc, since its better fit to the GPS data and, distinctly better correlation between afterslip and aftershock moment release. Therefore, my results challenge the common belief that the continental crust responds only elastically after megathrust earthquakes.

Finally, I calculate for the first time the transfer of stresses to the Illapel segment due to afterslip and non-linear viscous relaxation associated with the Maule event under the Coulomb Failure (CFS) theory. I show that the patterns of predicted horizontal surface displacement are opposite when using a model with linear and power-law rheology. Predictions from the power-law rheology case agree better with the GPS data. My results reveal that most of the CFS changes are due to the coseismic deformation. I also find that a direct triggering of the Illapel earthquake due to the Maule event is unlikely, since the small, albeit positive (~ 0.05 bar) CFS values calculated at the Illapel hypocenter. Conversely, seismicity $M_w \geq 5.0$ between these two events, in the southern region of the Illapel segment, occurs in areas of CFS > 0.2 bar, suggesting a mechanical triggering.

I conclude that geomechanical-numerical models incorporating temperature-dependent power-rheology with dislocation creep processes in the crust and upper mantle can be used to examine the underlying processes controlling the postseismic deformation. Furthermore, these models can produce deformation patterns that are more consistent with the physical concepts of strength distribution with depth and aftershock activity than earlier models that impose linear and non-linear rheologies without consideration of temperature.

Zusammenfassung

Räumliche und zeitliche Messungen aus satellitengestützten geodätischen Beobachtungen liefern grundlegende Randbedingungen für die Untersuchung der Erdbebenmechanismen und Prozesse während des seismischen Zyklus. Anhand der - insbesondere zeitabhängigen - Oberflächenbewegungen, die nach großen Erdbeben (in der postseismischen Phase) beobachtet werden, können sowohl das Reibungsverhalten der Störung als auch die rheologischen Eigenschaften im Lithosphäre-Asthenosphäre-System mit Hilfe geomechanischer Modelle untersucht werden. Während der postseismischen Phase sind Afterslip (transientes Gleiten nach dem Hauptbeben) an der Störungsgrenze und viskose Relaxation im Lithosphäre-Asthenosphäre-System die dominanten Mechanismen. Der relative Beitrag dieser beiden Prozesse ist jedoch nicht abschließend untersucht, was vor allem auf die Herausforderung zurückzuführen ist, das rheologische Verhalten des Lithosphäre-Asthenosphäre-Systems nach großen Subduktionsbeben zu modellieren. Dementsprechend nehmen Modelle der postseismischen Phase üblicherweise die gesamte Kruste als elastisches Material über einem viskoelastischen oberen Mantel mit linearer oder nichtlinearer Rheologie (Viskosität) an.

In dieser Dissertation integriere ich modernste geomechanisch-numerische Modelle, Global Positioning System-Beobachtungen (GPS) und Nachbebenseismizität, um die zugrunde liegenden Verformungsprozesse zu untersuchen, welche die postseismische Verformungen kontrollieren, die durch das Erdbeben von Maule 2010 (M_w 8.8 in Chile) induziert wurden. Ich konzentriere mich insbesondere auf die Untersuchung der grundlegenden Diskrepanzen in der resultierenden postseismischen Deformation zwischen linearen und Power-Law-Rheologien. Im Gegensatz zu früheren Arbeiten verwende ich zum ersten Mal ein Vorwärtsmodell, das die temperaturabhängige Power-Law-Rheologie berücksichtigt. Darüber hinaus implementiere ich einen neuartigen Ansatz zur Bewertung unterschiedlicher postseismischer Simulationen, indem ich die positive Korrelation zwischen Afterslip- und Nachbeben-Aktivität einbeziehe. Die aus der koseismischen und postseismischen Deformation resultierenden Spannungen nördlich der Bruchgebiets des Erdbebens von 2010, wo sich das M_w 8.4 Erdbeben von Illapel im Jahr 2015 ereignete, werden ebenfalls untersucht.

Die geomechanisch-numerischen Modelle berücksichtigen konstitutive Gleichungen, um die elastischen und viskosen Gesteinsreaktionen der Kruste und des oberen Mantels nach dem Hauptbeben zu simulieren. Im Falle der Power-Law-Rheologie werden die räumliche und zeitliche Verteilung der Viskosität durch die Dislokationskriechparameter und das Temperaturfeld in der Kruste und im oberen Mantel beeinflusst. Im Gegensatz dazu besteht der Fall der linearen Rheologie aus einem Material mit homogener und linearer Viskosität im oberen Mantel, während

die gesamte Kruste voll elastisch ist. Ich wende die Finite-Elemente-Methode (FEM) an, um die beteiligten partiellen Differentialgleichungen für diskrete Elemente, die das Untersuchungsgebiet repräsentieren, zu lösen. Die GPS-Beobachtungen und die Nachbebenseismizität bestehen aus veröffentlichten Daten, welche die sechs Jahre nach dem Maule-Ereignis von 2010 abdecken.

Durch die Verwendung eines 2D Modellansatzes zeigen meine Ergebnisse entscheidende Abweichungen in den modellierten postseismischen Oberflächenverschiebungen je nach Wahl der Modellrheologie. Durch Vergleich der Ergebnisse mit den GPS-Daten stelle ich fest, dass die GPS-Verschiebungsmuster durch die Simulation der Power-Law-Rheologie deutlich besser erklärt werden können, insbesondere die kumulative Hebung im vulkanischen Bogen über sechs Jahre und die schnellen transienten Verschiebungen in den ersten zwei Jahren nach dem Hauptbeben. Die primären Abweichungen in den kumulativen Mustern ergeben sich aufgrund des Ortes der viskosen Relaxation. Im Fall der linearen Rheologie findet der größte Teil der viskosen Relaxation im kontinentalen Mantelkeil unterhalb des Forearc statt. Umgekehrt tritt die viskose Relaxation im Fall der Power-Law-Rheologie hauptsächlich in der unteren Kruste, unterhalb des vulkanischen Bogens, aufgrund von Dislokationskriechprozessen auf.

In einer nachfolgenden Studie erweitere ich den 2D-Modellansatz auf 3D. Hier wähle ich die bevorzugte postseismische Simulation eines neuen Ansatzes aus, der nicht nur die beste Anpassung an die GPS-Beobachtungen berücksichtigt, sondern auch die räumliche Korrelation zwischen invertierten Afterslipverteilungen und Nachbebenaktivitäten einbezieht. Meine Ergebnisse zeigen, dass die Afterslip-Inversion stark von der Wahl der Rheologie abhängt, insbesondere in größeren Tiefen (> 60 km Tiefe). Ich zeige auch, dass eine Simulation mit nichtlinearer viskoser Relaxation in der kontinentalen unteren Kruste den tiefen Afterslip erheblich reduziert, was mit Beobachtungen eines relativ geringeren kumulativen Moment der Nachbeben und dem scheinbaren Fehlen einer interseismischen Locking in größeren Tiefen entlang der Plattengrenzfläche übereinstimmt. Umgekehrt führt der Fall der linearen Rheologie zu einem großen Afterslip in größeren Tiefen. Ähnlich wie bei den Ergebnissen des 2D-Modells bevorzuge ich eine 3D-Simulation, bei der die nichtlineare viskose Relaxation hauptsächlich in der unteren kontinentalen Kruste und in geringerem Maße im oberen kontinentalen Mantel unterhalb des vulkanischen Bogens auftritt, da sie besser zu den GPS-Daten passt und eindeutig die bessere Korrelation zwischen Afterslip und Nachbeben Momentabgabe aufweist. Daher stellen meine Ergebnisse die weit verbreitete Annahme in Frage, dass die kontinentale Kruste nach großen Subduktionsbeben nur elastisch reagiert.

Schließlich berechne ich zum ersten Mal die Übertragung von Spannungen auf das Illapel-Segment aufgrund von Afterslip und nichtlinearer viskoser Relaxation im Zusammenhang mit dem Maule-Ereignis nach der Coulomb-Versagens-(Coulomb Failure Stress - CFS)Theorie. Ich zeige, dass die Muster der vorhergesagten horizontalen Oberflächenverschiebung entgegengesetzt sind, wenn ein Modell mit linearer und Potenzgesetz-Rheologie verwendet wird. Vorhersagen aus dem Fall der Power-Law-Rheologie stimmen besser mit den GPS-Daten überein. Meine Ergebnisse zeigen, dass die meisten der CFS-Veränderungen auf die koseismische Deformation zurückzuführen sind. Ich zeige auch, dass eine direkte Auslösung des Illapel-Erdbebens durch das Maule-Beben unwahrscheinlich ist, da zwar positive, jedoch sehr kleine ($\sim$0.05 bar) CFS-Werte am Illapel-Hypozentrum berechnet wurden. Umgekehrt tritt die Seismizität $\mathrm{M_w} \geq 5.0$ zwischen diesen beiden Ereignissen in der südlichen Region des Illapel-Segments in Gebieten mit CFS > 0.2 bar auf, was auf eine mechanische Auslösung hindeutet.

Ich komme zu dem Schluss, dass geomechanisch-numerische Modelle, die eine temperaturabhängige Power-Law-Rheologie mit Dislokationskriechenprozessen in der Kruste und im oberen Mantel beinhalten, zur Untersuchung der zugrunde liegenden Prozesse, welche die postseismische Deformation steuern, verwendet werden können. Darüber hinaus können diese Modelle Verformungsmuster erzeugen, die mit den physikalischen Konzepten der Festigkeitsverteilung mit Tiefen- und Nachbebenaktivität konsistenter sind als frühere Modelle, die lineare und nichtlineare Rheologien ohne Berücksichtigung der Temperatur vorgeben.

Table of contents

List of figures

List of tables

Chapter 1

Introduction

1.1 Motivation

Earthquakes are a magnificent example of a living Earth and we, as human beings, have been living with them from ancient times. Nevertheless, the exponential worldwide population growth in the last century, in particular in seismically active zones, has largely increased the vulnerability of modern industrial societies to seismic and tsunami phenomena. Concretely, this results in massive loss of life, infrastructure damage, and financial instability, as witnessed in the past two decades from megathrust events such as the 2011 Mw 9.0 Tohoku-Oki, in Japan (Ohzono et al., 2012), the 2004 Mw 9.3 Sumatra-Andaman, in Indonesia (Lay et al., 2005), and the 2010 Mw 8.8 Maule, in Chile (Vigny et al., 2011). For instance, the case of the 2010 Maule earthquake in Chile, alongside its subsequent tsunami, resulted in a death toll of about 500 people and economic losses of USD 30 billion, which in the economical context of the country represented 15% of its nominal Gross Domestic Product at that time (Daniell et al., 2010). Additionally, population migration has been observed as an active natural response to earthquakes, affecting in turn the socio-economical configuration of the region by the large amount of people displaced. As shown by Bilak et al. (2016), the 2015 Mw 7.5 Gorka (Nepal) and the 2015 M_w 8.3 Illapel (Chile) earthquakes forced the displacement of 2,630,000 and 1,000,000 people, respectively. Consequently, earthquakes are far from being merely a scientific concern.

To understand earthquake mechanisms, unprecedented networks of cutting-edge seismometers and GPS stations have been installed at subduction zones, especially in the past two decades, through international collaborative efforts (e.g., Bedford et al., 2013; Loveless and Meade, 2010; Moreno et al., 2010; Métois et al., 2012; Schurr et al., 2014; Vigny et al., 2005, 2011). These geophysical instruments have recorded the deformation produced by the aforementioned earthquakes, and over their interseismic and postseismic periods as well, facilitating thus the investigation of the processes controlling the accumulation and release of strain on the fault interface over the seismic cycle. In particular, the integration of surface geodetic data, alongside geomechanical models, has become a powerful framework to investigate these earthquake cycle kinematics (Avouac, 2015, and references therein). Here, geodetic data provide insightful measurements of the crustal surface displacement field during the different stages of the seismic cycle (Fig.

1.1), and are used as constraints to simulate and explore the physical parameters involved in the accumulation and release of such a strain over seismic cycle by means of geomechanical models. Despite the number of great subduction earthquakes captured by seismic and geodetic networks, our knowledge of the underlying processes over the seismic cycle remains incomplete, especially the understanding of the behaviour and strain (or slip) budgets on the fault interface between the down-going oceanic and overriding continental plates. Two end-member fault behaviours involve a fault freely slipping and a fault fully locked. Particularly, the latter has been used as a proxy to forecast earthquake magnitude and size (Loveless and Meade, 2010; Moreno et al., 2010). A transition region between these two regions is also of vital importance since it can transiently release the strain through aseismic slip processes (e.g., slow slip and afterslip) (Peng and Gomberg, 2010; Scholz, 1998, and references therein), which may account for as much as 50–70% of the total slip budget on the seismogenic zone, as estimated by Perfettini et al. (2010) for the case of the M_w 8.0 Pisco earthquake in Peru. Therefore, characterizing and inferring the fault behaviour and strain budgets over the seismic cycle is critical for improving seismic hazard estimates as the available slip budget is proportional to earthquake magnitude and size (Avouac, 2015; Loveless and Meade, 2010; Moreno et al., 2010).

Slip quantification on the fault interface, as a measure of strain budgets and fault behaviour, is commonly inferred from the inversion of geodetic observations using geomechanical models. Unlike the interseismic and coseismic geodetic observations (Fig. 1.1a, b), where the imprint deformation is primarily due to fault-slip processes (e.g., Loveless and Meade, 2010; Moreno et al., 2012; Métois et al., 2012; Vigny et al., 2005), the postseismic geodetic observations also contain the transient contribution of viscous relaxation processes triggered by the main shock (Fig. 1.1c; and (e.g.), Barbot, 2018a; Sun et al., 2014; Wang et al., 2012). Thus, postseismic periods also provide a unique opportunity to investigate viscous relaxation processes in the lithosphere and asthenosphere. Accordingly, an accurate analysis of the relative contribution of afterslip and viscous relaxation processes to the geodetic observations is essential for assessing the remaining slip budgets on the fault interface after the main shock. This is of particular importance in seismic hazard research, since the remaining slip budget can promote destructive aftershocks, as the case of the M_w 7.3 aftershock that followed the 2015 M_w 7.8 Gorkha earthquake in Nepal (Feng et al., 2015; Mandal, 2018). However, determining the relative contribution of fault slip and viscous deformation is challenging, especially given that rheology of the lithosphere-asthenosphere system is poorly understood.

Nevertheless, the enormous increase of geophysical observations from megathrust earthquakes in the past two decades, especially for the case of the 2010 Maule earthquake, along with much progress made into investigating postseismic kinematics, provide an unique opportunity to improve our understating of both afterslip and viscous relaxation processes at subduction zones. These data provide insightful constraints to implement models with temperature-dependent power-law rheology, which has been scarcely studied in the lithosphere-asthenosphere system at subduction zones. More importantly, postseismic studies have widely assumed the whole crust as a fully elastic material, which is, in principle, in contrast to the crustal rock strength obtained from laboratory experiments (Bürgmann and Dresen, 2008; Kirby and Kronenberg, 1987; Ranalli, 1997; Rybacki and Dresen, 2000).

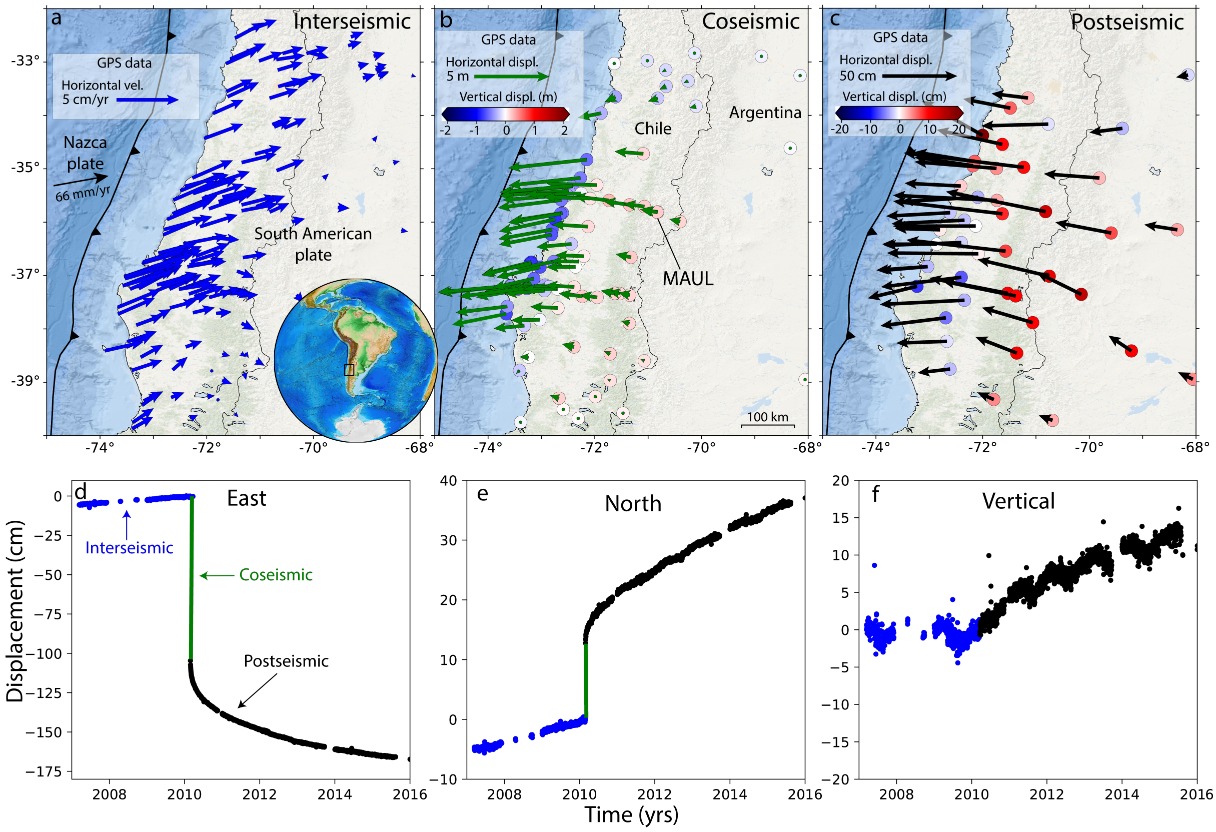

Fig. 1.1 GPS data in the rupture area of the 2010 M_w 8.8 Maule earthquake in Chile, illustrating the surface displacements over the seismic cycle. Similar patterns can be found at subduction zones in Indonesia and Japan (e.g., Loveless and Meade, 2010; Sun and Wang, 2015; Vigny et al., 2005). Upper panel shows the GPS observations for the interseismic (a), coseismic (b), and postseismic (c) periods. The interseismic GPS data corresponds to the annual velocity from Moreno et al. (2011, 2010). The coseismic GPS data are obtained from (Moreno et al., 2012; Vigny et al., 2011). The postseismic GPS are six-years cumulative displacements following the Maule mainshock from Li et al. (2017) and Peña et al. (2020). Lower panel exhibits the time series at GPS station MAUL (volcanic arc) from the daily solutions of Blewitt (2018) for the east (d), north (e), and vertical (f) components. Note the variability in cumulative vertical patterns (c) and the high-rate transient displacements in the first two years following the mainshock (black dots in d,e,f).

1.2 State of the art

Earthquakes are the sudden release of the strain at plate interfaces accumulated over decades or centuries (Ruiz and Madariaga, 2018; Scholz, 1998). In particular, subduction zones, where the failure mechanism involves thrust faulting, account for almost 90% of the total seismic moment release worldwide (Pacheco and Sykes, 1992). In the years following the main shock, the coseismically imposed stresses in the crust and upper mantle are gradually relaxed with the amplitude of postseismic deformation, generally decaying with time as recorded by GPS data (Fig. 1.1d,e,f). These processes primarily involve the continuous slip of the fault in the same direction of the main shock, the so-called afterslip, and viscous relaxation in the lithosphere-asthenosphere system (Bedford et al., 2013; Hsu et al., 2006; Masuti et al., 2016a; Pollitz, 2003; Wang et al., 2012). Although postseismic poroelastic rebound also occurs in the crust, its contribution to the observed surface displacements is small compared to afterslip and viscous processes (Freed et al., 2017; Rousset et al., 2012b; Sun et al., 2014). However, the relative contribution of afterslip and viscous relaxation processes to the postseismic observations is still poorly understood.

Insightful Global Positioning System (GPS) observations before, during, and after megathrust earthquakes have indeed facilitated the investigation of the relative contributions of afterslip and viscous relaxation processes to the geodetic observations. Particularly, postseismic observations following the 2010 Maule (Chile, Fig. 1.1c) and 2011 Tohoku-Oki (Japan) earthquakes marked a turning point in the investigation of postseismic processes at subduction zones. Before these two events, sparse GPS and/or tide gauge records were available to investigate postseismic processes globally (Barrientos et al., 1992; Hsu et al., 2006; Khazaradze et al., 2002; Perfettini and Avouac, 2007; Suito and Freymueller, 2009), where only a few stations had time series spanning several years or decades. First studies showed that afterslip processes are dominant in the short term (months; e.g., Perfettini et al., 2010), while viscoelastic processes in the upper mantle dominates at long term (decades; e.g., Hu et al., 2004; Khazaradze et al., 2002). Nonetheless, these studies mostly used the horizontal component of the GPS observation, and considered models with fully elastic material properties or a fully elastic crust above a homogeneous viscoelastic mantle with linear Maxwell rheology.

The GPS data acquired following the 2010 Maule and 2011 Tohoku-Oki earthquakes, especially from vertical displacements and time series, have provided essential constraints for investigating postseismic processes. Here, time series provide key information of the postseismic controlling processes, as they exhibit non-linear patterns, decaying at variable scales and periods (Fig. 1.1d–f). Additionally, the similar surface displacement patterns in the cumulative vertical component, as shown from the Maule and Tohoku-Oki events, notably the fast uplift in the volcanic arc (Fig. 1.1c), suggest that common non-linear processes control the postseismic deformation after megathrust earthquakes. Following previous findings, short-term postseismic models only focused on investigating afterslip processes using fully elastic models (Bedford et al., 2013; Lin et al., 2013; Ozawa et al., 2011). Nevertheless, the assumption that afterslip processes dominate the short term and near field was questioned by the offshore GPS observations in the Tohoku-Oki region, as they exhibit landward motion, i.e., opposite to afterslip, one year following the main shock (Sun et al., 2014; Watanabe et al., 2014). Here, Sun et al. (2014) showed that this horizontal pattern can be explained by viscoelastic processes in the upper mantle using bi-viscous Burgers rheology, but their study neglected the vertical GPS component. Furthermore, the results from Sun et al. (2014) also indicated that Burgers rheology is a good candidate to explain the transient postseismic deformation, as it combines (short-term) transient viscosity and (long-term) steady-state viscosity, also in agreement to other studies (e.g., Hu et al., 2016; Klein et al., 2016; Sun and Wang, 2015). Nevertheless, the model of Sun et al. (2014) also considered a fully elastic crust above an upper mantle with Burgers rheology, whose transient and steady-state viscosities are not a function of temperature at depths, rather than are homogeneously distributed in the mantle wedge, oceanic mantle, as well as a thin layer between the lithosphere and asthenosphere. On the other hand, the incorporation of second order power-law rheology, where the distribution, magnitude and decay law of the viscosity depend mainly on the temperature field and the stress exponent (creep constant related to the decay of the stress relaxation), was difficult to validate using megathrust earthquakes postseismic data prior to the 2010 Maule and 2011 Tohoku-Oki earthquakes.

Upon beginning this work in 2016, a number of works on the postseismic kinematics of the Maule, Tohoku-Oki, and other earthquakes had been published. These previous studies have used linear Maxwell or Burgers rheologies to investigate afterslip and viscous relaxation processes after megathrust earthquakes (e.g., Diao et al., 2014; Hu and Wang, 2012; Klein et al., 2016; Pollitz et al., 2006b; Sun and Wang, 2015; Trubienko et al., 2014; Tsang et al., 2016; Wang and Fialko, 2014; Wang et al., 2012; Yamagiwa et al., 2015). Generally speaking, models that consider these rheologies in the upper mantle and a completely elastic crust tend to overestimate afterslip at down-dip regions and underestimate it at up-dip regions (e.g., Sun et al., 2014; Tsang et al., 2016). However, the role of temperature-dependent power-law rheology in the postseismic deformation processes in the aftermath of megathrust earthquakes had barely been investigated (Hergert and Heidbach, 2006; Montesi, 2004), particularly in the estimation of afterslip distribution and viscous patterns. These few power-law rheology studies at subduction zones showed that power-law rheology is critical for explaining the non-linear decay of the displacements over time observed by GPS data. Conversely to previous studies, the study of Hergert and Heidbach (2006) also showed that non-linear viscous relaxation in the continental lower crust may explain the postseismic deformation following the 2001 M_w 8.4 Southern Peru earthquake. However, in their study they used a 2D modelling approached constrained only by one continuous GPS station, whereas afterslip was not considered. Montesi (2004) also used a limited GPS network, and this work focused purely on investigating the shear zones between the plates interface with velocity-strengthening friction laws, linear and power-law rheology from a simple spring-slider model. Similarly, at strike-slip systems, previous studies employing power-law rheology also concluded that non-linear rheology could considerably better explain the GPS signal compared to linear rheology, for the case of the 1992 M_w 7.3 Landers and 1999

M_w 7.1 Hector Mine earthquakes in eastern California, USA (e.g., Freed and Bürgmann, 2004; Freed et al., 2012; Takeuchi and Fialko, 2013). Nevertheless, these studies did not investigated the impact of rheology on afterslip distributions.

Up to now, a few more studies have employed power-law rheology to investigate postseismic processes at subduction zones (Agata et al., 2019; Barbot, 2018b, 2020; Muto et al., 2019; Qiu et al., 2018; Shi et al., 2020a; Weiss et al., 2019). Comparable to models accounting for Maxwell or Burgers rheology in the upper mantle, the inclusion of power-law rheology in the upper mantle, while the crust is considered fully elastic, reduces the afterslip at greater depths (> 60 km) and increases it at shallower regions, as shown by Qiu et al. (2018) for postseismic periods occurring in the Sumatra-Andaman region, Indonesia. Yet, large-magnitude afterslip distributions still result at greater depths when only considering Maxwell, Burgers, or power-law rheologies in the upper mantle, which is in contrast to the frictional behaviour obtained from aftershocks (Lange et al., 2012; Lay et al., 2012), seismic wave radiation (Lay et al., 2012), rate-and-state friction laws (Avouac, 2015; Scholz, 1998), and interseismic locking maps (Loveless and Meade, 2010; Moreno et al., 2010; Métois et al., 2012). Conversely, Agata et al. (2019) employed a stress-driven afterslip rather than an afterslip inversion approach, and also power-law in the upper mantle and a crust fully elastic, to show that afterslip is primarily distributed at regions shallower than 60 km depth on the fault interface for the case of the Tohoku-Oki event. Similarly, the study of Muto et al. (2019) also indicated that afterslip mostly occurs at depths < 60 km, but still considerable afterslip of approximately 50 cm occurs at 100 km depths. The model of Muto et al. (2019) considered power-law rheology in the upper mantle and only a small region in the lower crust beneath the volcanic arc, i.e., most of the crust was considered fully elastic, although they considered a 2D planar-strain model almost perpendicular to the trench, and thus no lateral deformation variations were investigated.

On the 27 of February, of 2010 a megathrust earthquake magnitude M_w of 8.8 struck central Chile (Fig. 1.2; and, e.g., Moreno et al., 2012; Vigny et al., 2011). It was the first great event to be captured by a modern, denser geodetical network (Moreno et al., 2012; Vigny et al., 2011). The Maule earthquake broke a mature segment, of about 500 km along strike (Fig. 1.2), where the last great earthquake in this region occurred in 1835, with a magnitude of approximately 8.5 (Ruiz and Madariaga, 2018, , and references therein). The Maule earthquake have triggered a number of studies examining the processes controlling the interseismic, coseismic, and especially postseismic deformation. The afterslip distribution on the fault interface following the 2010 Maule event has been investigated by studies considering models with fully elastic material properties (Aguirre et al., 2019; Bedford et al., 2013; Lin et al., 2013; Vigny et al., 2011), linear rheology in the upper mantle and an elastic crust (Bedford et al., 2016), Burgers rheology in the upper mantle and an elastic crust as well (Klein et al., 2016), and recently power-law rheology in the lower crust and upper mantle (Weiss et al., 2019). The resulting afterslip distributions from these studies show important variations. For instance, the model of Bedford et al. (2013) results in afterslip with a maximum magnitude of about 2 m, mainly occurring between 25–60 km depths, but also at greater depths. In contrast, the model of Klein et al. (2016) results in approximately

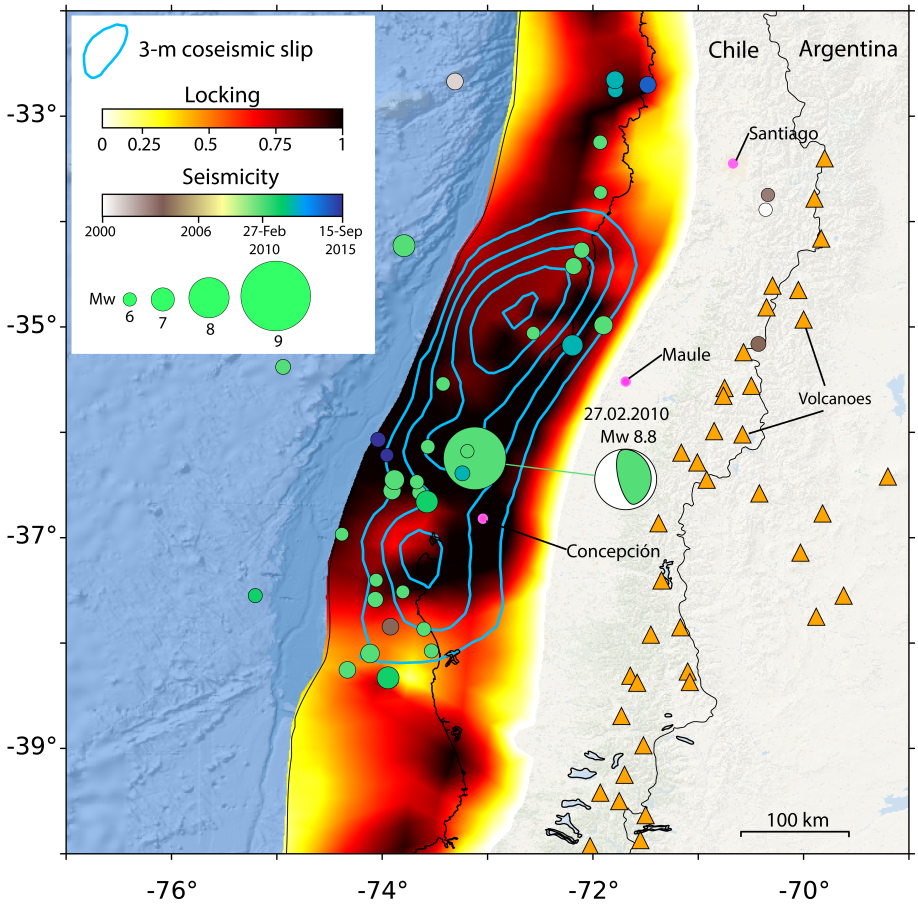

Fig. 1.2 The 2010 M_w 8.8 Maule earthquake, central Chile. Background color-coded represents the interseismic locking obtained from Tilmann et al. (2016). Blue contour lines depict the coseismic slip of the 2010 Maule event from Moreno et al. (2012). Location of main cities (Santiago, Maule and Concepción) is also shown in pink. Color-coded circles display the seismicity from 2000 to September 15, 2015, obtained from the National Seismological Center (CSN), Chile. The size of green circles in the white rectangle illustrates the magnitude of earthquakes.

8-9 m of afterslip in the shallower 55 km depths, with large amount also in the vicinity of the trench at regions < 20 km depth. Additionally, the model of Klein et al. (2016) employed a low-viscosity subduction channel, from 55–135 km depth on the fault interface. Similarly, the resulting afterslip distribution from Weiss et al. (2019) also show afterslip patterns up to 8 m. On the other hand, the model of Weiss et al. (2019) did not incorporate power-law rheology in the whole model, rather than in a region in the lower crust and upper mantle. Therefore, the role of temperature-dependent power-law rheology, in the whole lithosphere-asthenosphere system, in the postseismic deformation after megathrust earthquakes remains unclear.

1.3 Scientific research questions

This dissertation aims at bringing together the available observational evidence (geodetic and seismological) and state-of-the-art geomechanical-numerical models to examine the underlying processes controlling the postseismic deformation, with a case of study the 2010 Maule earthquake. I focus on investigating the rheology of the lithosphere-asthenosphere system, with special attention in the continental crust. Additionally, I investigate the impact of rheology on magnitude, distribution, and patterns of afterslip and viscous relaxation, as well as on the transfer of stresses to neighbouring segments, within a range of realistic rock parameters, data uncertainty, and model resolution. In the following, I summarize the scientific research questions investigated through this dissertation:

- Can power-law rheology be used to investigate the postseismic deformation associated to the 2010 Maule event, and what are the principal differences in the resulting postseismic displacements from models considering linear or power-law rheologies?
- What is the rheology model's role in location, magnitude, and patterns of afterslip and viscous relaxation following megathrust earthquakes, especially when a continental crust with power-law rheology is also considered?
- How can additional information from independent observations such as aftershock activity be integrated to assess postseismic models better?
- How much stresses are transferred to neighbouring segments due to afterslip and viscous relaxation, and to what extent are they related to postseismic seismicity and ultimately to megathrust earthquakes?

1.4 Structure of the dissertation

This original dissertation is a publication-based work from two published peer-reviewed papers and one in preparation (see Table 1.1 for further details), which are reformatted from its original form in the present document. The core work is presented in Chapters 3, 4, and 5, while Chapter 2 introduces the basic concepts of the scientific principles and methods to carry out this work: The seismic cycle, Global Positioning System (GPS) observations, and Finite Element Method (FEM). In Chapters 3 and 4, I present the investigation on the understanding of the underlying processes controlling the postseismic displacements. In Chapter 3, I use a two-dimensional (2D) model approach, while in Chapter 4, the 2D model is extended into a three dimensional (3D) approach. These two Chapters focus on the investigation of the kinematics. On the other hand, Chapter 5 focus on the dynamics, in this context, the investigation of the stress field. In Chapter 6, I synthesize the main results from Chapters 3, 4, and 5, as well as their implications in the current state of our knowledge are discussed. Finally, a summary with key conclusions and potential future work are extracted and presented in Chapter 7. A brief description of core Chapters is presented in the following.

- In chapter 3, I use for first time a 2D geomechanical-numerical model with power-law rheology to investigate the postseismic deformation following the 2010 Maule earthquake. Afterslip and relocking processes are also incorporated into the model, as prescribed displacements on the fault interface. To constrain the model results, I use GPS data. Furthermore, the linear rheology case is considered for comparison. This chapter examines the main differences in displacement patterns from the use of linear or power-law rheologies, and the location and magnitude of afterslip and viscous relaxation.

- In Chapter 4, I extend the 2D to a 3D model approach. I have also extended the dislocation creep parameters in the crust and upper mantle. Additionally, I employ an inversion approach to obtain the afterslip distribution on the fault interface. I investigate the main differences in the resulting afterslip distribution from the choice of rheology model and dislocation creep parameters. Moreover, I use an integrated, innovative analysis, which considers the assumption that afterslip processes primarily drive aftershocks, to discriminate competing simulations.

- In Chapter 5, I examine the transfer of stresses to the northern (Illapel) segment of the 2010 Maule rupture zone, due to the coseismic and postseismic deformation of the Maule event. This is the first study to investigate the mechanical connection between the Maule and Illapel events under the Coulomb Failure Stress (CFS) theory, integrating afterslip and power-law rheology into a 3D model.

1.5 Description of manuscripts

In the following, I list the three manuscript that compromise the core of this cumulative dissertation, where I am the first author. Furthermore, an additional peer-reviewed publication as co-authors is also listed. The latter is not include in the present document, as most of my contribution to this publication was done before the PhD program.

Table 1.1 Three main publication as first and corresponding author that compromise this manuscript-based dissertation. Author's contribution follows the approach of Ghan et al. (2016).

Title	Role of the Lower Crust in the Posteismic Deformation of the 2010 Maule Earthquake: Insights from a Model with Power-Law Rheology
Authors	**Carlos Peña**, Oliver Heidbach, Marcos Moreno, Jonathan Bedford, Moritz Ziegler, Andrés Tassara, Onno Oncken
Year	2019
Journal	Pure and Applied Geophysics
Volumen	176, 3913–3928
DOI	https://doi.org/10.1007/s00024-018-02090-3
Status	Published
Contribution	Conceptualization, Methodology, Software, Validation, Formal analysis, Investigation, Writing (original draft, review and editing), Visualization, Project administration
Title	Impact of Power-Law Rheology on the Viscoelastic Relaxation Pattern and Afterslip Distribution following the 2010 M_w 8.8 Maule Earthquake
Authors	**Carlos Peña**, Oliver Heidbach, Marcos Moreno, Jonathan Bedford, Moritz Ziegler, Andrés Tassara, Onno Oncken
Year	2020
Journal	Earth and Planetary Science Letters
Volumen	542, 116292
DOI	https://doi.org/10.1016/j.epsl.2020.116292
Status	Published
Contribution	Conceptualization, Methodology, Software, Validation, Formal analysis, Investigation, Writing (original draft, Review and Editing), Visualization, Project administration
Title	Transient Stress Pattern induced in the Illapel Segment by the 2010 Maule Earthquake
Authors	**Carlos Peña**, Oliver Heidbach, Marcos Moreno, Daniel Melnick, Onno Oncken
Year	2020
Journal	Frontiers in Earth Sciences or Geophysical Journal International
Volumen	–
DOI	–
Status	In preparation
Contribution	Conceptualization, Methodology, Software, Validation, Formal analysis, Investigation, Writing (original draft, Review and Editing), Visualization, Project administration

Table 1.2 Additional publication as co-author.

Title	Kinematics of subduction processes during the earthquake cycle in Central Chile
Authors	Leonardo Aguirre, Klaus Bataille, Camila Novoa, **Carlos Peña**, Felipe Vera
Year	2019
Journal	Seismological Research Letters
Volumen	90(5), 1779–1791
DOI	https://doi.org/10.1785/0220180391
Status	Published
Contribution	Conceptualization, Software, Validation, Formal analysis, Investigation, Writing (review and editing)

Chapter 2

Scientific principles and methods

2.1 The seismic cycle

Earthquakes have been a matter of concern since time immemorial, dating from 2000 B.C. Earthquake mechanisms were first attributed to mythical and astrological causes. For instance, the believe that they were the result of the angry of Poseidon by shaking the surface ground with his trident in Greek mythology. In contrast to this view, many philosophers addressed earthquake mechanism from a rational perspective in Ancient Greece, of which the formulation from Aristotle (ca. 330 B.C.) was the most influential and extensive occidental research up to the Middle Ages (Oeser, 1992). In his view, earthquakes are produced by the shaking of air trapped inside the Earth as it tries to escape. Nevertheless, it was not until the 1780s where earthquakes such as the 1746 Lima in Peru, 1755 Lisbon in Portugal, and 1783 Calabria in Italy triggered an enlightened discussion on earthquake causes (Oeser, 1992). In particular, pioneers research by Michell (1761) and Young (1807), from the 1755 Lisbon earthquake, gave the first basic ideas about earthquake wave propagation inside the Earth. Thereafter, essential breakthroughs on earthquake mechanisms were made by several researchers such as F. Omori, Ernst yon Rebeur-Pasebwitz, J. Milne, Rayleigh, Love, Gutenberg, Oldham, Mohorovicic, among many others (Ben-Menahem, 1995, and references therein).

Currently, the accepted earthquake mechanisms rely on elastic rebound (Reid, 1910) and plate tectonics (Isacks et al., 1968) theories. Plate tectonics provides the driving forces to explain plate movements and elastic loading, while elastic rebound the concepts for seismic energy loading and unloading through dislocation at plate boundaries. Reid's theory suggests that the elastic energy or strain is accumulated at plate boundaries for tens or hundreds of years, in a period called interseismic (Fig. 1.1a and Fig. 2.1), which is suddenly released as large earthquakes, the so-called coseismic period (Fig. 1.1b and 2.1). In this light, the crustal displacement field experiences opposite sense in both periods. Right after the main shock, a period that exhibits time-dependent surface deformation is observed, similar to the one from aftershocks, as described long ago by Omori in 1894 (Omori, 1894). This postseismic period may last from years to decades (e.g., Perfettini et al., 2010; Wang et al., 2012).

Seismic and aseismic processes balance the total seismic energy throughout the seismic cycle. The terms seismic and aseismic may be misleading, especially when talking about aftershock and afterslip (postseismic processes). I will therefore summarize their main features. A particular quality of seismic and aseismic processes, is their duration. Seismic processes (e.g., earthquakes, foreshocks, aftershocks) are associated to events less than 5-10 minutes. On the other hand, aseismic (Slow Slip Events (SSE) and afterslip) to longer periods, lasting from days to years (see Fig. 5 in Peng and Gomberg, 2010, and references therein). Although aftershocks also produce slip on the fault interface after the mainshock, the nature of the overall postseismic slip on the fault interface is predominantly aseismic, since the moment release by afterslip exceeds the one from aftershocks by a large factor (e.g., Bedford et al., 2013; Lange et al., 2014; Perfettini et al., 2010; Peña et al., 2020). Afterslip is a frictional process that has been successfully modelled by geomechanical models considering laboratory-derived rate-and-state (friction) laws (e.g., Agata et al., 2019; Avouac, 2015; Perfettini and Avouac, 2007). Additionally, afterslip processes have been attributed to primary drive aftershocks (e.g., Agurto-Detzel et al., 2019; Hsu et al., 2006; Kato, 2007; Lange et al., 2014; Perfettini and Avouac, 2007). Moreover, large earthquake imposed differential stresses in the lithosphere-asthenosphere system, which are gradually relaxed by (volumetric) viscous relaxation processes during the postseismic period (e.g., Khazaradze et al., 2002; Sun et al., 2014; Wang et al., 2012). These postseismic processes, afterslip and viscous relaxation, are the processes controlling the postseismic deformation at subduction zones (Freed et al., 2017; Sun et al., 2014; Wang et al., 2012). The main processes across the seismic cycle are schematised in Fig. 2.1.

The investigation of these processes is possible due the integration of geomechanical models and essential constraints provided by geodetic observations (e.g., GPS, InSAR). The work presented in this dissertation considers, especially, GPS observations and geomechanical-numerical models to examine postseismic deformation processes. Hence, in the following sections I will further describe the GPS observations and geomechanical-numerical model implantation.

2.2 Global Positioning System observations

Geodetic measurements have been widely applied to geophysical purposes. First surface geodetic measurements date from the 1880´s in the Nankai Trough, Southwest Japan, consisting of relative vertical leveling of the Earth’s surface (Okada, 1960; Thatcher, 1984). Those pioneering observations captured the surface deformation before, during, and after large earthquakes, providing thus the first picture of the strain buildup over the seismic (Okada, 1960; Okada and Nagata, 1953; Thatcher, 1984).

Significant advances in geodetic techniques in the last century, particularly with the birth of Satellite Geodesy in the 1960’s, have revolutionised the Earth sciences. Modern-day Global Navigation Satellite System (GNSS) consists of a global coverage network of satellites providing signals from space that transmit positioning and timing data to GNSS receivers (Fig. 2.1). This information is then used by the receivers to determine geo-location with millimetre precision.

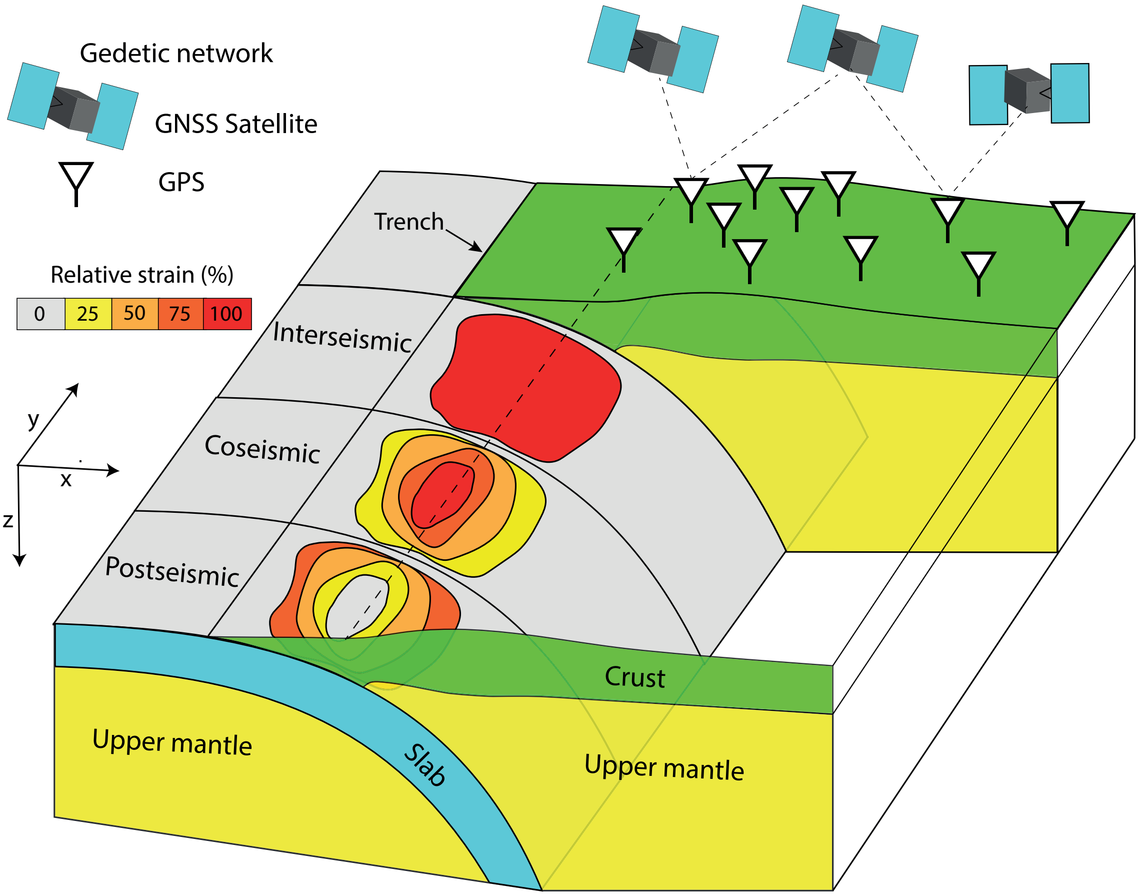

Fig. 2.1 Sketch of the periods and main processes throughout the seismic cycle. For the interseismic periods, it is shown at a very advanced stage. Furthermore, in the interseismic period, studies have demonstrated the existence of aseismic slip processes (Sow Slip Events, SSE), which can transiently release a substantial amount of energy (e.g., Dragert et al., 2001; Peng and Gomberg, 2010). For the Maule case, however, such processes have not been discovered yet. In color-coded, on the fault interface, the strain over the seismic cycle is also illustrated. Viscous relaxation also occurs in the postseismic periods in the lithosphere-asthenosphere system.

Examples of GNSS receivers are Europe's Galileo, Russia's Global'Naya Navigatsionnaya Sputnikovaya Sistema (GLONASS), and the USA's NAVSTAR Global Positioning System (GPS). The latter is the most utilized GNSS, and can offer high-level accuracy (1-2 mm), high-rate sampling (1 Hz), and three-dimensional relative displacements of Earth's surface. GPS measurements can either be taken continuously (cGPS) or repeat survey (sGPS) points.

In several subduction zones, extensive cGPS and sGPS networks have been deployed (Fig 1.1; and e.g., Bedford et al., 2016; Klotz et al., 1999; Loveless et al., 2009; Moreno et al., 2010). This has enabled to capture the lithosphere response due to the deformation processes over the seismic cycle (e.g., earthquakes, afterslip, and viscous relaxation), as shown in Fig. 1.1 and Fig. 2.1. In particular, in the last two decades, GPS data have provided key observations to demonstrate that: interseismic locking maps can be used as first-order predictions of magnitude and location of earthquakes (Loveless and Meade, 2010; Moreno et al., 2010); slow slip events generally occur worldwide (Dragert et al., 2001; Peng and Zhao, 2009; Schurr et al., 2014), afterslip and poroelastic processes could trigger aftershocks (Hughes et al., 2010; Kato, 2007), and viscous relaxation in the upper mantle also occurs in short-term periods (months; Sun et al., 2014).

In this dissertation, I use the GPS data published by several authors in central Chile (Bedford et al., 2013; Blewitt, 2018; Li et al., 2017; Melnick et al., 2017; Moreno et al., 2012, 2010; Métois et al., 2012; Vigny et al., 2011). These GPS data sets are employed to thoroughly investigate the controlling postseismic processes, focusing on the 2010 Maule earthquake. Description of the GPS observations used in this dissertation are extensively described in Chapters 3, 4, and 5. An outline of these GPS data sets can be found in Table 2.1.

Table 2.1 Summary of the GPS observations

Chapter	Source	Period	Comment
III	Moreno et al. (2012)	Coseismic	Data selected along a 2D profile perpendicular to the trench in the center of the 2010 rupture zone
	Li et al. (2017)	Postseismic	Same af before
IV	Moreno et al. (2010); Métois et al. (2012)	Interseismic	Used to remove the interseismic component from the postseismic GPS data from Li et al. (2017)
	Moreno et al. (2012)	Coseismic	All data
	Li et al. (2017)	Postseismic	All data
V	Melnick et al. (2017)	Postseismic	Postseismic data focused on the Illapel segment. Unlike Melnick et al. (2017), I also used the exponential components of the GPS data in this study

2.3 Finite Element Method

2.3.1 Introduction

Finite Element Method (FEM) is used to solve complex mathematical problems. Although it is difficult to date its origin, first developments can be traced back to the early 1940', from the need to solve challenging elasticity and structural analysis problems in civil and aeronautical engineering (Courant, 1943; Hrennikoff, 1941). In these works (Courant, 1943; Hrennikoff, 1941), the first ideas of the method were introduced, i.e., discretization of a continuous domain into a set of discrete sub-domains called elements. FEM has become one of the most used methods in engineering, and geosciences as well. This is because its wide range of offer and accuracy to solve partial differential equations (PDE), such as those associated to thermal, fluids, and electromagnetic problems, in addition to its capability to consider challenging domain geometries.

Along with GPS observation, as previously described, the implementation of FEM in geomechanical models has also enabled us to expand our knowledge in earthquake-related processes considerably. Common problems associated to earthquakes-processes are the elastic deformation due to earthquakes, time-dependent viscous deformation during postsesmic periods, thermal state of the lithosphere and asthenosphere, fluids propagation in the upper crust, formation of main cordilleras, and so on. In particular, the use of geomechanical-numerical models incorporating FEM, to investigate deformation processes over the seismic cycle, has large advantages compared to, for instance, analytical geomechanical models (e.g., Okada, 1985), since FEM can take into account different types of material properties in the problem domain, challenging geometries, and multi-physical approaches (e.g., elastic, poroelastic, and plastic rheologies) (Masterlark, 2003). In contrast, some of its disadvantages are: large amount of sub-domain (elements) is required to achieve optimal solutions and may be time-consuming.

In the following, I will describe the key ingredients to setup a geomechanical-numerical model incorporating FEM: Finite elements, governing equations, and the implementation of rheological models.

2.3.2 Concept of FEM

Elements are the cornerstone of FEM. Here, an adequate election of the amount and type of elements is critical for achieving accurate solutions, as represented in Fig. 2.2. They compose the domain problem, using geometric forms connected by point in the space, usually called nodes. Most of the geometries used in 2D problems are triangles and quadrilaterals. On the other hand, in its 3D version, tetrahedrons and brick elements are employed (see example in Fig. 2.3, with tetrahedrons). The deformable shape, composed of finite elements, can be approximate with a good level of accuracy, by assuming a limited number of nodal displacements. The finite number of displacements at nodes is called number of degrees of freedom n (DOF) of the structure or the model domain. The numerical problem in the continuum with finite number of elements and degrees of freedom can be written as a system of linear equations:

$$[K]_{n\times n} \cdot \mathbf{u}_{n\times 1} = \mathbf{F}_{n\times 1} \tag{2.1}$$

where $[K]$ is a symmetric matrix with dimensions $n \times n$ and called stiffness matrix, while $\mathbf{u}$ and $\mathbf{F}$ are vectors comprising the nodal displacements and the applied forces, respectively (Zienkiewicz et al., 2005). The stiffness matrix K relates properties of each finite element, such as area and length of the elements, Young´s modulus, and density.

2.3.3 Geomechanical-numerical model implementation

The setup of a geomechanical-numerical model incorporating FEM consists of three main steps: pre-processing, processing or numerical solution, and post-processing. In Fig. 2.4, I illustrate these steps with the principal tasks. Pre-processing corresponds to the creation of the geometries and mesh of the model. Furthermore, in this step, the model domain is discretized in finite elements, and the material properties and initial conditions are assigned. In the second step, numerical solution, the involved PDEs in the numerical problem are solved. An example of the PDEs of motion can be found in Fig. 2.4. Finally, in the post-processing step, the modelled

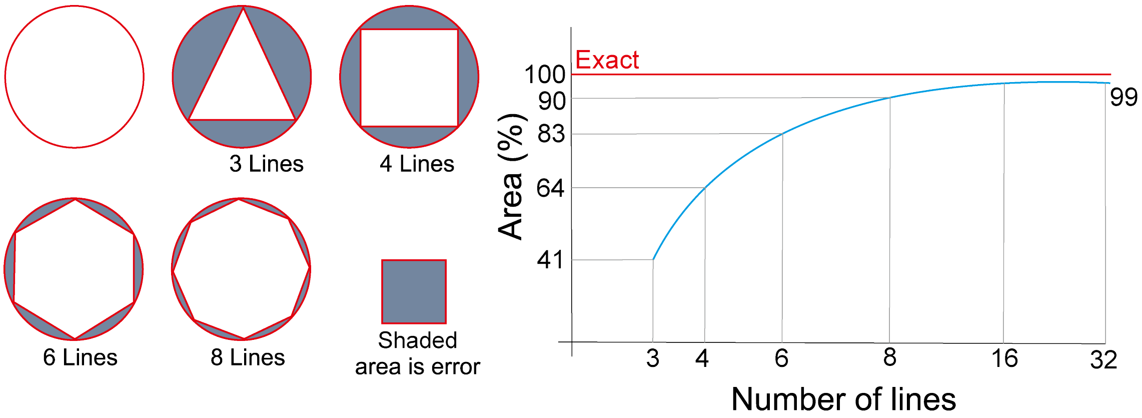

Fig. 2.2 Accuracy as a function of element lines to reproduce a given area (red circle). Here, the number of lines is analogous to the number of elements. It can be observed that the more elements, the better solutions. Figure modified from Gokhale (2008) and Moreno (2010).

results are extracted and compared against the geophysical observations to adjust and validate the model. After that, the model results are interpreted. Fig. 2.4 also exhibits the main softwares

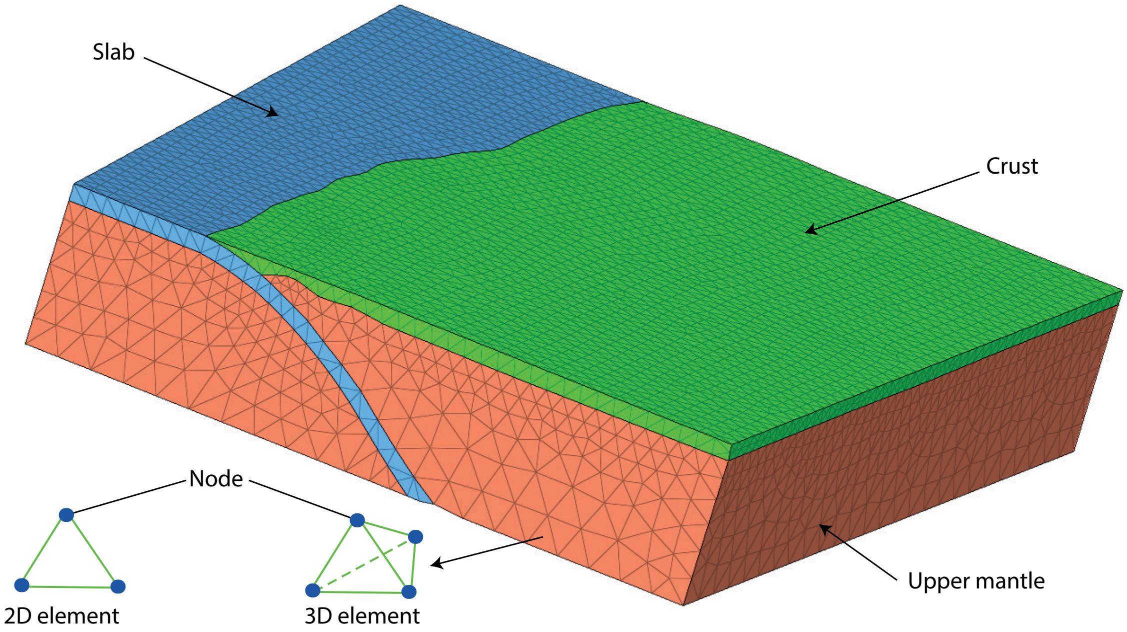

Fig. 2.3 Example of mesh in a 3D subduction zone model domain. The 3D model consists of 90,000 (tetrahedrons) finite elements.

that I use to investigate postseismic processes in this dissertation. In the pre-processing step, I use Hypermesh versions 2015 and 2019. I consider triangles and tetrahedrons elements in the 2D and 3D models, respectively. Here, the elements are small enough in the area of key interest to avoid numerical problems. Additionally, I tested second-order type of elements to explore the accuracy of the results. However, I find a negligible impact from the amount of elements used in the 2D and 3D models. For the processing, I use Abaqus^{TM} versions 6.11 and 6.14. Abaqus^{TM} is a powerful software employed in industry, engineering, as well as in science. It also provides pre-processing (geometry creation and meshing) and post-processing (visualization).

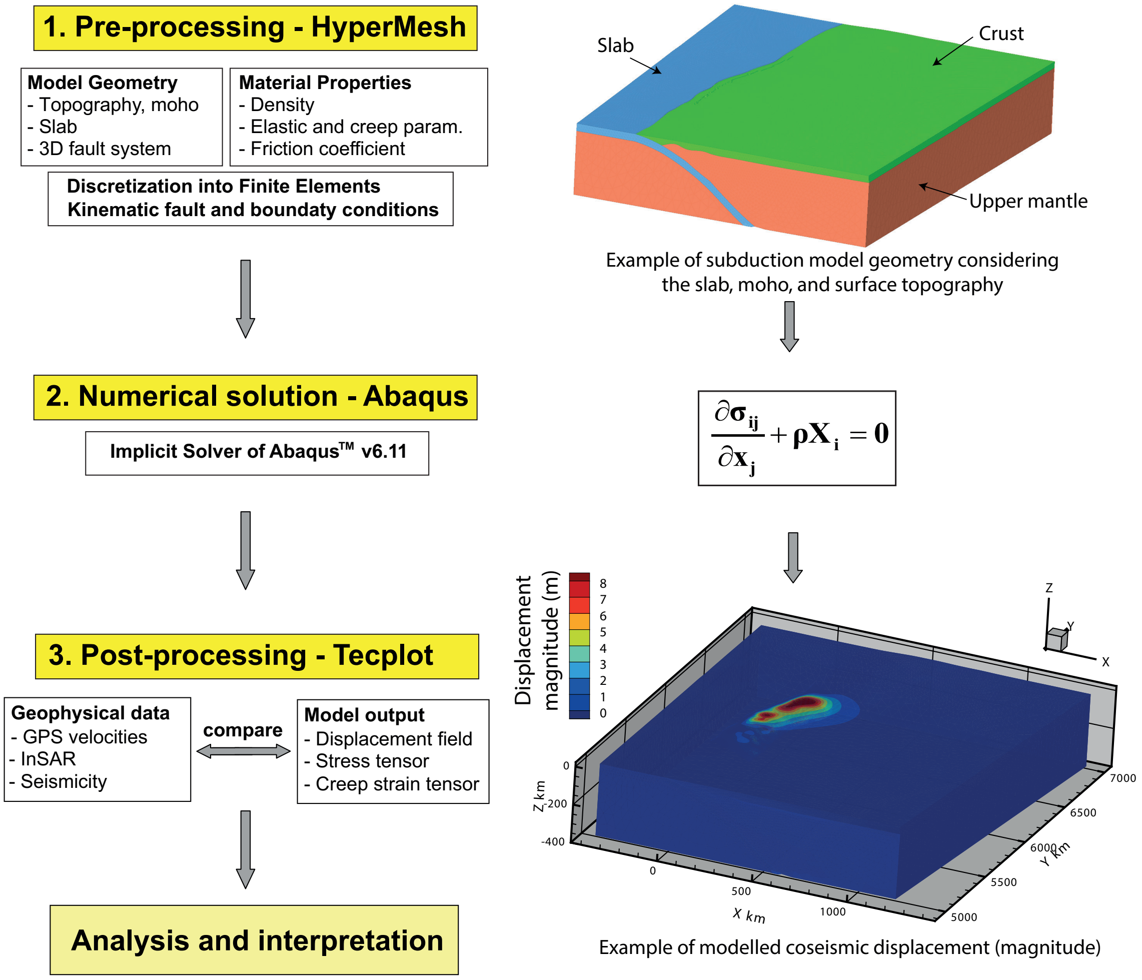

Fig. 2.4 Workflow of geomechanical-numerical model setup.

Nevertheless, I minimally employ them in this work. Instead, I use Tecplot 360 EX versions 2015 and 2019 for the data post-processing and visualization. The Basemap matplotlib Toolkit libraries from python and Matlab are also employed.

2.4 Rheological models

Rheology is the branch of physics that investigates the way materials deform or flow in response to applied forces or stresses. Materials can experience different responses such as elastic (time-independent), viscous (time-dependent), or both. In the context of earthquake phenomena, the instantaneous response of the lithosphere is elastic, which is accompanied in the incoming months and years by a time-dependent viscoelastic response. To understand viscous properties of a rock material, a critical concept is viscosity, which is a measurement of the resistance of a material or fluid to deform at a given rate. In the following, I will summarize the concepts and equations of key rheologies used in this dissertation: linear elasticity, linear Maxwell, and power-law.

2.4.1 Elastic material

The linear elastic behavior is based on elasticity Hooke´s law. For an isotropic material, two constants are required to characterize the stress-strain relationship completely: the Lamé constant λ and G shear modulus. The resulting relationship between these constants can be written in the following form:

$$\sigma = \lambda e \mathbf{I} + 2G\varepsilon \tag{2.2}$$

where σ and ε are the stress and strain matrices (tensors), respectively, and e is the trace of ε, i.e., the volumetric strain. Other elastic constants are the Young´s modulus E, the Poisson´s ration ν and the bulk modulus B described by:

$$\begin{aligned} E &= \frac{G(3\lambda + 2G)}{\lambda + G} \\ \nu &= \frac{\lambda}{2(\lambda + G)} \\ B &= \lambda + \frac{2}{3}G \end{aligned} \tag{2.3}$$

Therefore, if the values of λ and G are known, E, ν and K can be also calculated. Alternatively, we can write λ and G as a function of E and ν as:

$$\begin{aligned} \lambda &= \frac{\nu E}{(1+\nu)(1-2\nu)} \\ G &= \frac{E}{2(1+\nu)} \end{aligned} \tag{2.4}$$

2.4.2 Viscoelastic material

Viscoelastic materials combine elastic and viscous properties. The elastic part is recoverable, while permanent deformation can be also observed from the viscous component. Depending on the microscopic properties of the material and the ambient conditions under which the material is set (e.g., temperature and pressure), the viscous response can be linear (Newtonian) or non-linear (Non-Newtonian). Studies investigating the viscoelastic response of the lithosphere-asthenosphere after large earthquakes have widely used linear Maxwell and Burgers rheologies (Bürgmann and Dresen, 2008, and references therein). These rheologies were introduced by Maxwell (1867) and Burgers (1935), respectively. The basic strain-strain representation of the Maxwell and Burgers rheologies can be found in Fig. 2.5. These rheologies combine springs and dashpots elements, representing the linear elastic and linear viscous responses, respectively. However, these rheologies do not consider the physical mechanism (e.g., activation energy, temperature) controlling plastic deformation in rocks at high temperatures (Bürgmann and Dresen, 2008; Karato, 2010).

In contrast to linear Maxwell and Burgers rheologies, power-law rheology corresponds to a strain-stress representation, empirically derived from laboratory experiments, investigating the physical mechanisms controlling rock deformation at high-temperature conditions (e.g., Chopra,

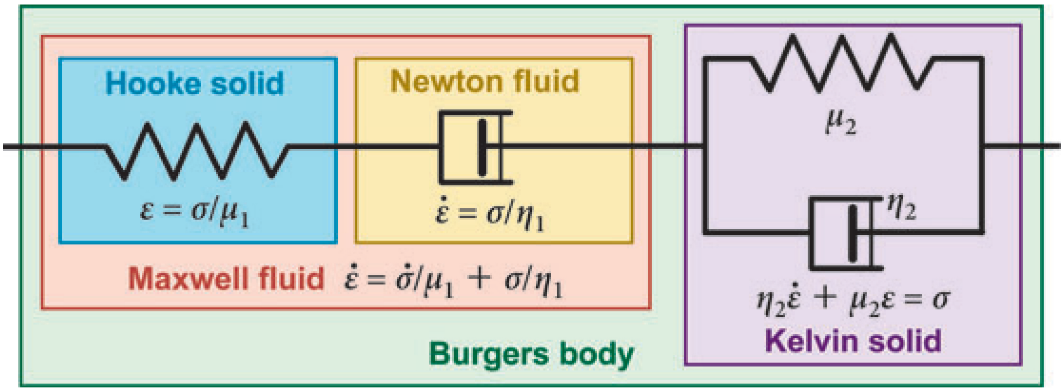

Fig. 2.5 Schematic representation of the Maxwell and Burgers rheologies. Figure modified from Bürgmann and Dresen (2008). The Burgers rheology is the combination of Maxwell and Kelvin elements connected in series. The Maxwell element (body) represents the steady-state (long-term) part, with viscosity η_1 and shear modulus μ_1. The transient (short-term) part is composed by the Kelvin body, with viscosity η_2 and shear modulus μ_2. The strain rate and differential stress are represented by $\dot{\varepsilon}$ and σ, respectively.

1997; Hirth and Kohlstedt, 1996; Karato and Wu, 1993; Rybacki and Dresen, 2000). These experiments have enormously facilitated our understating of the mechanism controlling plastic deformation in rocks. For instance, they showed that, under relatively low stresses, the dominant deformation mechanism is (linear viscous) diffusion creep. Conversely, at relatively high stresses, (non-linear viscous) dislocation creep processes prevail (e.g., Hirth and Kohlstedt, 2003; Karato and Wu, 1993). The total creep strain is given by:

$$\dot{\varepsilon}_{total} = \dot{\varepsilon}_{diffusion} + \dot{\varepsilon}_{creep} \tag{2.5}$$

where $\dot{\varepsilon}_{diffusion}$ and $\dot{\varepsilon}_{dislocation}$ are the strain rate from diffusion and dislocation creep processes, respectively. Nevertheless, during postseismic periods, dislocation creep processes prevail over diffusion creep (Agata et al., 2019; Freed and Bürgmann, 2004; Freed et al., 2017, 2012; Karato, 1986). Consequently, the total creep strain during the postseismic period can be approximated as:

$$\dot{\varepsilon}_{total} = \dot{\varepsilon}_{creep} = A\sigma^n e^{\frac{-Q}{RT}} \tag{2.6}$$

where A is a material constant, σ is the differential stress, n the stress exponent, Q the activation energy, R the gas constant, and T is the temperature (Bürgmann and Dresen, 2008; Hirth and Kohlstedt, 2003; Karato and Wu, 1993). We can also write Equation 2.6 in terns of the effective viscosity η as:

$$\begin{aligned} \eta &= \frac{\sigma}{2A\dot{\varepsilon}} \\ &= \frac{\sigma^{1-n} e^{\frac{Q}{RT}}}{2A} \end{aligned} \tag{2.7}$$

In this dissertation, the jointly effect of elastic and viscous (dislocation creep) responses are combined in the 2D and 3D geomechanical-numerical models. Elastic and dislocation creep parameters used in this dissertation are shown in sections 3.2.1 and 4.2.4.

2.5 Inversion of GPS data

GPS observations and geomechanical-numerical models are commonly combined to investigate postseismic processes through inversion approaches, using the so-called Green´s functions. Green´s functions are a mathematical representation of an impulse response of a linear differential operator, defined on the model domain, with pre-defined initial conditions (Menke, 2018). For instance, in Chapter 4, the Green´s functions are used to obtain the afterslip distribution on the fault interface. Here, the impulse response consists of a unity of (after)slip at each node on the fault interface, generating a response (displacement) in the surface of the 3D model domain. The response in the surface of the model is calculated at each node resembling the position of each GPS. The impulse response is then used to generate a matrix **G**, which contains information that relates the surface displacement at each GPS due to the slip on the fault interface. Mathematically, the linear system of equation between Green´s functions and the observed displacements can be expressed as:

$$\mathbf{G}_{ij}\mathbf{m}_{j\times 1} = \mathbf{d}_{i\times 1} \tag{2.8}$$

where the matrix **G** corresponds to the surface displacement at each node in the model, representing the GPS data locations, due to each unity of slip, at each node on the fault interface. Equation 2.8, however, is usually undetermined, as there is a higher number of unknown parameters than observations. Thus, additional constraints need to be considered to ensure convergence. As afterslip does not vary dramatically among nodes forming the fault, a smoothing Laplacian operator **L**, which minimizes large slip among nodes, can be added to Equation 2.8 (Bedford et al., 2013; Masterlark, 2003; Moore et al., 2017). Therefore, the linear system of equations to be solved is:

$$\begin{bmatrix} \mathbf{G}_{ij}\mathbf{m}_{j\times 1} \\ \lambda \mathbf{L} \end{bmatrix} = \begin{bmatrix} \mathbf{d}_{i\times 1} \\ \mathbf{0} \end{bmatrix} \tag{2.9}$$

where λ is a damping operator and **L** can be written in terms of a finite difference operator of a two-dimensional array **s** as:

$$\nabla^2 \mathbf{s} = \frac{\mathbf{s}_{xi-1,yi} - 2\mathbf{s}_{xi,yi} + \mathbf{s}_{xi+1,yi}}{\triangle x^2} + \frac{\mathbf{s}_{xi,yi-1} - 2\mathbf{s}_{xi,yi} + \mathbf{s}_{xi,yi+1}}{\triangle y^2} \tag{2.10}$$

with $\triangle x$ and $\triangle y$ correspond to the respective along-strike xi and along-dip yi surface projections patches (nodes) of the fault interface. Equation 2.9 will be inverted, using a standard inversion approach and GPS observations. Election of the operator λ are found and further details can be found in Chapter 4.

Chapter 3

Role of Lower Crust in the Postseismic Deformation of the 2010 Maule Earthquake: Insights from a Model with Power-Law Rheology

Abstract

The surface deformation associated with the 2010 M_w 8.8 Maule earthquake in Chile was recorded in great detail before, during and after the event. The high data quality of the continuous GPS (cGPS) observations has facilitated a number of studies that model the postseismic deformation signal with a combination of relocking, afterslip and viscoelastic relaxation using linear rheology for the upper mantle. Here, we investigate the impact of using linear Maxwell or power-law rheology with a 2D geomechanical-numerical model to better understand the relative importance of the different processes that control the postseismic deformation signal. Our model results reveal that, in particular, the modeled cumulative vertical postseismic deformation pattern in the near field (< 300 km from the trench) is very sensitive to the location of maximum afterslip and choice of rheology. In the model with power-law rheology, the afterslip maximum is located at 20—35 km rather than > 50 km depth as suggested in previous studies. The explanation for this difference is that in the model with power-law rheology the relaxation of coseismically imposed differential stresses occurs mainly in the lower crust. However, even though the model with power-law rheology probably has more potential to explain the vertical postseismic signal in the near field, the uncertainty of the applied temperature field is substantial, and this needs further investigations and improvements.

3.1 Introduction

At subduction zones, the sudden release of strain that has accumulated over tens to hundreds of years repeatedly produces the failure of large areas of the boundary interface, resulting in great ($M_w > 8.5$) or even giant (M_w 9.0) earthquakes (Barrientos and Ward, 1990; Chlieh et al., 2007; Moreno et al., 2012; Schurr et al., 2014). This sudden slip is followed by postseismic deformation that gradually relaxes the coseismically induced stress perturbations. The rate of postseismic deformation is time-dependent and has been attributed to three primary processes: (1) afterslip ((Bedford et al., 2013; Perfettini et al., 2010) Hsu et al. 2006; Tsang et al. 2016), (2) poro-elastic rebound (Hu et al., 2014; Hughes et al., 2010) and (3) viscoelastic relaxation (Hu et al., 2004; Pollitz et al., 2006b; Qiu et al., 2018; Rundle, 1978; Wang et al., 2012). Interseismic relocking or simply relocking is another process that may occur shortly after megathrust events. Bedford et al. (2016) inferred that the fault interface relocked within the first year after the 2010 Maule earthquake. A similar finding was obtained by Remy et al. (2016) after the 2007 Pisco, Peru, earthquake. In the past decade, the increased spatial density of continuous GPS (cGPS) instrumentation at subduction zones together with the implementation of geomechanical-numerical models has allowed us to test the relative importance of these processes in time and space (Bedford et al., 2013; Govers et al., 2018; Klein et al., 2016; Li et al., 2018, 2017; Sun et al., 2014). In these studies, linear viscoelastic relaxation has been used to infer the viscosity structure of the upper mantle and to understand the postseismic deformation signal in the near, middle and far field. These models assume that the crust is purely elastic and that the relaxation in the upper mantle can be described with a linear viscoelastic rheology using either the Maxwell (Govers et al., 2018; Hu et al., 2004; Li et al., 2018, 2017) or Burgers body (Klein et al., 2016; Sun et al., 2014). Furthermore, most of these models consider an inversion scheme to estimate the location and magnitude of afterslip as well as the viscosity structure of the mantle that results in a best fit of the observed cumulative postseismic deformation signal derived from GPS observations. Alternatively, in their 2D geomechanical-numerical forward model Hergert and Heidbach (2006) showed that a power-law rheology with dislocation creep can also fit the vertical and horizontal time series of the postseismic relaxation after the 2001 Arequipa earthquake. However, for their study only one cGPS station at 225 km distance from the trench was available and no afterslip was considered.

The 2010 M_w 8.8 Maule earthquake that struck south-central Chile was one of the first great events to be captured by modern space-geodetic monitoring networks (Moreno et al., 2012; Vigny et al., 2011). Through a rapid international collaborative effort, a dense cGPS network of 67 stations (Bedford et al., 2013; Bevis et al., 2010; Vigny et al., 2011) was installed to monitor the postseismic surface deformation (Fig. 3.1). Recent analyses of the postseismic deformation signal from the Maule earthquake have drawn attention to the limits posed by using a linear viscoelastic relaxation with homogeneous viscosity distribution in the mantle (Klein et al., 2016; Li et al., 2018, 2017) to explain the heterogeneity of the vertical postseismic signal, showing that a simple process is not a candidate to explain the postseismic signal associated with the 2010 Maule case. The best-fit model from Klein et al. (2016) results in a heterogeneous viscosity structure with a deep viscoelastic channel up to 135 km depth along the fault interface and afterslip at regions close to the up- and down-dip limits to explain in particular the pattern of the observed vertical displacement and the displacement over time in the north, east and vertical components recorded by the cGPS time series. On the other hand, Li et al. (2018, 2017) showed how lateral viscosity variations improve the fit of the observed cumulative postseismic vertical deformation while having less effect on the horizontal predictions. Furthermore, they speculate that a power-law rheology could also explain the postseismic relaxation, in agreement with results from laboratory experiments (Bürgmann and Dresen, 2008; Hirth and Tullis, 1994; Karato and Wu, 1993; Kirby and Kronenberg, 1987).

In this article, we investigate the general differences that result from the use of a power-law rheology compared with a linear viscoelastic relaxation in a Maxwell body for the purpose of better understanding the processes controlling the spatio-temporal patterns of the postseismic deformation signal. We construct a 2D geomechanical-numerical model along a cross section perpendicular to the strike of the subduction zone at 36°S sub-parallel to the maximum of the coseismic slip of the Maule earthquake (Fig. 3.1). We model the first 6 years of postseismic deformation and compare our model results with the vertical and horizontal components of the cumulative and time series displacements of cGPS sites as a function of distance from the trench. The primary focus of this study is not to achieve a best-fit solution of the cGPS signal using an inversion scheme; instead, we use forward models to study the principal differences between a linear Maxwell and power-law rheology. However, the results of our test series to study the sensitivity due to linear Maxwell versus power-law rheology as well as due to the location and magnitude of afterslip partly show a remarkably good fit to the observed postseismic signals.

Our model results indicate that the overall contribution of relocking to the cumulative postseismic deformation signal is small compared with the impact of afterslip and viscoelastic relaxation. Our model results confirm previous studies (Klein et al., 2016; Li et al., 2018, 2017; Qiu et al., 2018) that showed that the vertical postseismic deformation signal is the key to better assess the relative importance of the involved processes, i.e., the viscosity, effective viscosity, maximum magnitude and location of afterslip. We show that in particular the predicted cumulative vertical postseismic signal in the near field (distance < 300 km from the trench) is very sensitive to the choice of model rheology as well as the afterslip location and maximum. The model with power-law rheology favors afterslip at depths of 20–35 km rather than at the down-dip limit of the seismogenic zone > 50 km. This shift of afterslip location is explained with the dislocation creep process that occurs in the deeper part of the lower crust and the uppermost mantle.

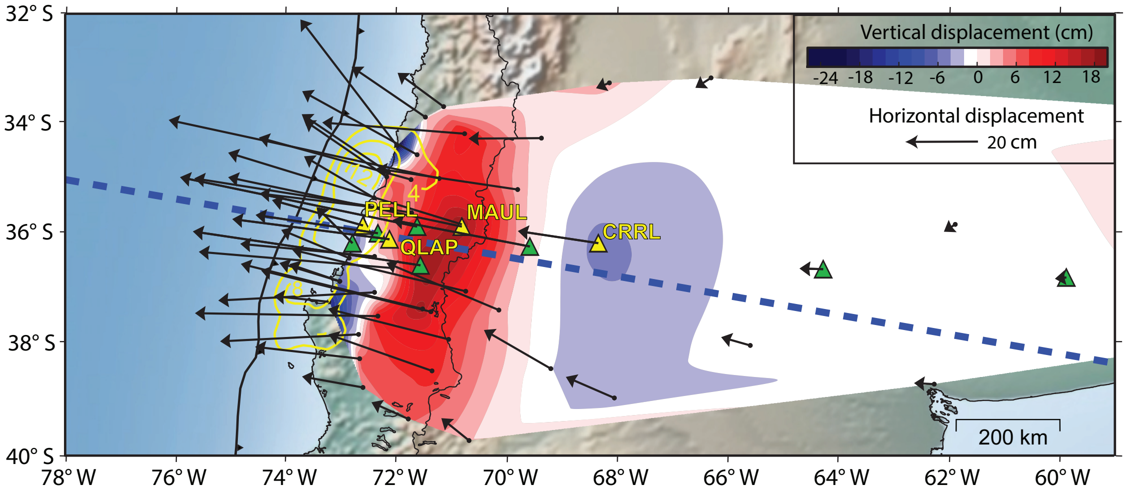

Fig. 3.1 Study area and cumulative postseismic displacement after 6 years of the Maule event derived from cGPS observations in the stable South American reference frame. Horizontal (black arrows) and interpolated vertical displacements (color coded) show the cumulative postseismic deformation in the first 6 years after the M_w 8.8 Maule earthquake. Green and yellow triangles display the 11 cGPS sites used in this study. Yellow triangles show the four cGPS sites considered for the time series analysis. Yellow contour lines depict the 2010 Maule earthquake coseismic slip from Moreno et al. (2012). Blue dotted line represents the 2D model cross section oriented parallel to the horizontal postseismic deformation

3.2 Model Description

3.2.1 Model setup

In the first 6 years following the Maule event, the postseismic surface displacement is almost perpendicular to the strike of the trench. We thus choose a 2D model cross section oriented parallel to the direction of the observed horizontal cumulative postseismic displacement vector.

The model geometry is derived from the model of Li et al. (2017). The cross section is almost perpendicular to the trench and cuts through the center of the coseismic rupture where the key postseismic deformation processes take place (Fig. 3.1). The model geometry takes into account the geometry of the slab (Hayes et al., 2012) and extends 3800 km in the horizontal and 400 km in the vertical direction to avoid boundary effects (Fig. 3.2a).

The model is discretized with 112,000 finite elements with a high resolution close to the slab interface where the coseismic displacement occurs and a significantly coarser resolution at the model boundaries where no deformation is expected. We assign to each element the rock properties presented in Table 1 differentiating the continental crust, oceanic crust/slab and upper mantle. At the lower and lateral model boundaries, the model cannot displace in the normal direction, but it is free to move parallel to the model boundaries; the model surface is free of constraints (Fig. 3.1).

The temperature field of the model is taken from Springer (1999) by interpolating the temperature contours and assigning the according temperature to each node of the finite elements (Fig. 3.2b). The temperature field is assumed to be time-independent as no significant changes are expected within 6 years. Coseismic slip models for the Maule earthquake (Bedford et al., 2013; Klein et al., 2016; Moreno et al., 2012; Vigny et al., 2011; Yue et al., 2014) show some differences, mainly in magnitude and location of maximum slip. This is most probably due to the use of different data sets and regularization methods in the inversion process. Postseismic deformation modeled with power-law rheology depends on the coseismic stress changes, and therefore may vary depending on the coseismic slip distribution. In this study, we decided to implement the coseismic slip distribution from the inversion of Moreno et al. (2012) as a displacement boundary condition on the fault plane (Fig. 2c), because our study shares the same numerical approach (FEM), margin geometry (slab and Moho discontinuities) and elastic material parameters as Moreno et al. (2012). To fit the observed coseismic displacement from previous studies (Moreno et al., 2012; Vigny et al., 2011), we assign 70% of the coseismic slip to the upper side of the fault plane toward the up-dip direction and 30to the bottom side toward the down-dip direction (Govers et al., 2018; Hergert and Heidbach, 2006; Sun and Wang, 2015). The same ratio is applied to simulate afterslip and relocking.

The afterslip is modeled with a Gaussian distribution curve and decays exponentially to the 2nd year as explained by Marone et al. (1991). The afterslip decay law also is in agreement with the aftershock seismicity (Fig. 3.2), which is a first-order approximation for the afterslip decay law for the 2010 Maule case (Bedford et al., 2013; Lange et al., 2014). Klein et al. (2016) found cumulated afterslip values on the order of 100 cm at 45 km depth between 2011 and 2012 for the postseismic deformation associated with the Maule event. Thus, we start with 100 cm of maximum afterslip centered at 48 km depth, but vary these values in different model scenarios. Different afterslip decay laws may achieve a better fit to the data; however, we do not explore this parameter since the main focus of this study is to investigate the first order differences between the models that use linear Maxwell or power-law rheology instead of perfectly fitting the observations. Relocking is assumed as backslip on the rupture plane with a convergence velocity of 6 cm year $^{-1}$ and takes place linearly up to the 6th year. With these kinematic boundary conditions, i.e., the coseismic rupture, afterslip distribution and relocking, the model simulates the postseismic relaxation of stresses during 6 years. The resulting numerical problem is solved using the commercial finite element code ABAQUS$^{\text{TM}}$, version 6.11.

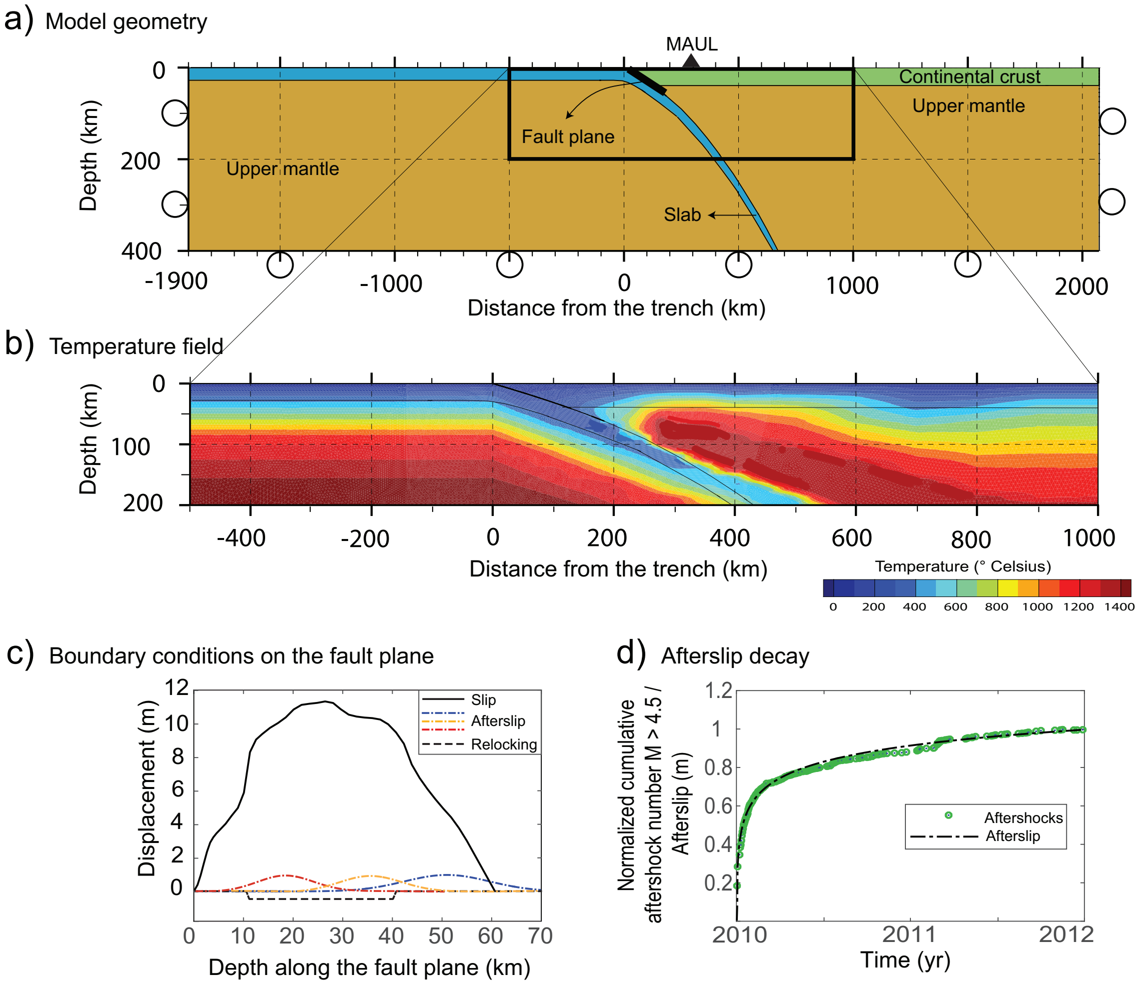

Fig. 3.2 Model setup. a) The 2D model geometry along the cross section shown in Fig. 1. Circles indicate that no displacement is allowed perpendicular to the model boundary. Fig. 2a is exaggerated in the vertical by a factor of two. b) The implemented temperature field according to Springer (1999) in the area of key interest. c) Distribution of coseismic slip taken from the inversion of Moreno et al. (2012) and afterslip distributions. d) Afterslip decay law used in this study. The aftershocks seismicity corresponds to Mw > 4.5 taken from the NEIC catalogue (www.usgs.gov).

3.2.2 Model rheology

We implement the dislocation creep law for models with power-law rheology using the expression stated in Kirby and Kronenberg (1987)

$$\dot{\varepsilon} = A\sigma^{n} e^{\frac{-Q}{RT}} \tag{3.1}$$

Table 3.1 Elastic and creep parameters

Layer	Rock type[b]	Young's module E (MPa)[a]	Poisson's ratio[b]	Pre-exponent A (MPa^{-n} s^{-1})[b]	Stress exponent n[b]	Activation enthalpy Q (kJ mol^{-1})[b]
Continental Crust	Wet quartzite	1.0×10^{-5}	0.265	3.2×10^{-4}	2.3	154
Oceanic crust/slab	Diabase	1.2×10^{-5}	0.3	2.0×10^{-4}	3.4	260
Continental mantle	Wet olivine	1.6×10^{-5}	0.25	2.0	3	433

[a] Reference source from Christensen (1996) and Khazaradze et al. (2002)
[b] Reference source from Ranalli (1997) and Karato and Wu (1993)

where $\dot{\varepsilon}$ is the strain rate, A is a pre-exponent parameter, σ the differential stress, n the stress exponent, Q the activation enthalpy for creep, R the gas constant and T the absolute temperature. The key control is the stress exponent n and the temperature field. In particular, the latter controls were in the continental crust where the brittle-ductile transition (BDT) zone is located (Brace and Kohlstedt 1980; Ranalli 1997). Below the BDT the differential stress is relaxed by dislocation creep processes. Our models with linear Maxwell rheology use a viscosity of 1.3×10^{19} Pa s for the uppermost mantle and elastic parameters for the crust and oceanic/slab. This value is in agreement with previous studies on the Chilean subduction zone (Bedford et al., 2016; Hu et al., 2004) that found viscosity values on the order of 10^{19} Pa s. We emphasize that the main difference is the fact that in our model with linear Maxwell rheology the whole crust is considered as an elastic material above a viscous mantle, while in the model with power-law rheology the viscosity distribution is controlled by the implemented temperature field. Elastic and creep parameters used in the model area are listed in Table 3.1.

3.2.3 GPS observations

The cGPS observations in the Maule region show trench-ward motion in the horizontal component and different patterns of deformation in the vertical component along longitude, with a pronounced uplift in the Andean region (Fig. 3.1). We use the first 6 years of postseismic surface displacements observed by cGPS as reported by Li et al. (2017). In this data set, the effect of aftershocks was removed by applying the trajectory model of Bevis and Brown (2014). To compare with the prediction of our 2D model, we selected 11 cGPS sites distributed in the near, middle and far field for comparison with our model (yellow triangles in Fig. 3.1).

3.3 Results

Based on the model described in the previous section, we set up three different model groups to test the general difference when using linear Maxwell or power-law rheology in the model. An overview of different model parameters is provided in Table 3.2. In the first test group we focus on models with powerlaw rheology and investigate the relative impact of relocking and afterslip on the postseismic deformation pattern (Section 3.3.1 and Fig. 3.3). In the second test group we focus on differences when using linear Maxwell or power-law model rheology and different afterslip magnitudes (Section 3.3.2 and Fig. 3.4), and in the third test group we investigate the differences when using linear Maxwell or power-law model rheology and different depth locations of the maximum afterslip (Section 3.3.4 and Fig. 3.5).

Table 3.2 Description of the model parameters (rheology, afterslip and relocking) used in this study.

Model	Maximum of afterslip (cm)	Depth of the maximum afterslip (km)	Relocking (cm/year)	Temperature °C	Graph color and type
NLA100D48R	100	48	6	T	Figs. 3, 4 and 5: solid blue
NLA100D35R	100	35	6	T	Fig. 5: solid orange
NLA100D20R	100	20	6	T	Figs. 5 and 6: solid red
NLA100D48	100	48	-	T	Fig. 3: solid thin blue
NLA20D48R	20	48	6	T	Figs. 3 and 4: solid cyan
NLA20D48	20	48	-	T	Fig. 3: solid thin cyan
NLA0R	0	-	6	T	Figs. 3 and 4: solid green
NLA0	0	-	-	T	Figs. 3, 6 and 8: solid thin green
NLA0T + 100	0	-	-	T + 100	Fig. 8: solid dark red
NLA0T - 100	0	-	-	T - 100	Fig. 8: solid pink
LA100D48R	100	48	6	T	Figs. 4 and 5: dashed blue
LA100D35R	100	35	6	T	Fig. 5: dashed orange
LA100D20R	100	20	6	T	Figs. 5 and 6: dashed red
LA20D48R	20	48	6	T	Fig. 4: dashed cyan
LA0R	0	-	6	T	Fig. 4: dashed green
LA0	0	-	-	T	Fig. 6: dashed pink

The rheology, linear (L, Maxwell) and non-linear (NL, power-law), the maximum afterslip (A), the relocking (R), and changes in the initial temperature field from Springer (1999) model (T) are indicated in the model name. If relocking is considered it is always with a rate of 6 cm/yr

3.3.1 Relative Impact of Relocking and Afterslip in Models with Power-Law Rheology

Fig. 3.3 shows the comparison of the cumulative postseismic surface displacement after 6 years between the model results and the data from the cGPS stations. We used three different maximum amplitudes of afterslip at 48 km depth. To evaluate the relative contribution of relocking, we fully and uniformly locked the fault interface as backslip between 10 and 40 km depth (Govers et al., 2018; Tichelaar and Ruff, 1993). We also perform tests without relocking to assess its relative impact on the cumulative vertical and horizontal postseismic displacement signal (Fig. 3.3). The models with and without relocking produce landward motion in the very near field (< 50 km from the trench). In general, our results indicate that relocking does not affect the deformation field significantly (see continuous versus dashed lines in Fig. 3.3). A small signal is seen close to the trench (< 80 km from the trench), and it vanishes at distances 200 km from the trench for both the horizontal and vertical displacements. Changing the maximum of the afterslip does not change the pattern of the horizontal surface deformation at distances 600 km from the trench, but it changes the magnitude of trench-ward motion at distances between 150 and 400 km from the trench. Beyond distances of 600 km from the trench, the results show trench-ward motion when 100 cm of maximum afterslip is used, but small landward motion when it is reduced to 20 and 0 cm, respectively. Interestingly, our results show that the vertical deformation is the component most sensitive to the afterslip maximum. The afterslip centered at the down-dip limit of the seismogenic zone produces maximum uplift around 100 km from the trench. When 100 cm afterslip is applied, an uplift of 40 cm after 6 years is accumulated. This number is considerably reduced when only 20 cm maximum afterslip is used; without any afterslip it changes to subsidence. These results are in agreement with Wang and Fialko (2014, 2018), who found afterslip at the downdip limit produces uplift at that region, while subsidence is controlled by viscoelastic relaxation. Beyond distances of 400 km, the impact of different afterslip magnitudes is negligible.

The overall pattern of the horizontal cGPS signal is better explained by models with small afterslip at the down-dip limit of the seismogenic zone than when 100 cm of afterslip is considered, in particular in the area of largest deformation between 200–400 km from the trench. An increase in maximum afterslip results in an increase in surface deformation that leads to an overestimation of the horizontal component in the near field.

The observed patterns in the vertical signal are also in better agreement with models when a smaller afterslip is applied. Adding afterslip shifts the higher uplift signal toward the trench, in a different pattern as observed by the cGPS observations. All models are in a good agreement with the cGPS observations in the far-field (> 500 km from the trench). However, none of the models can explain the wavelength of the declining uplift signal observed between 300–500 km from the trench (Fig. 3.3b). In general, the geomechanical-numerical model with power-law rheology results qualitatively in a good fit to the overall surface deformation pattern observed at the cGPS sites.

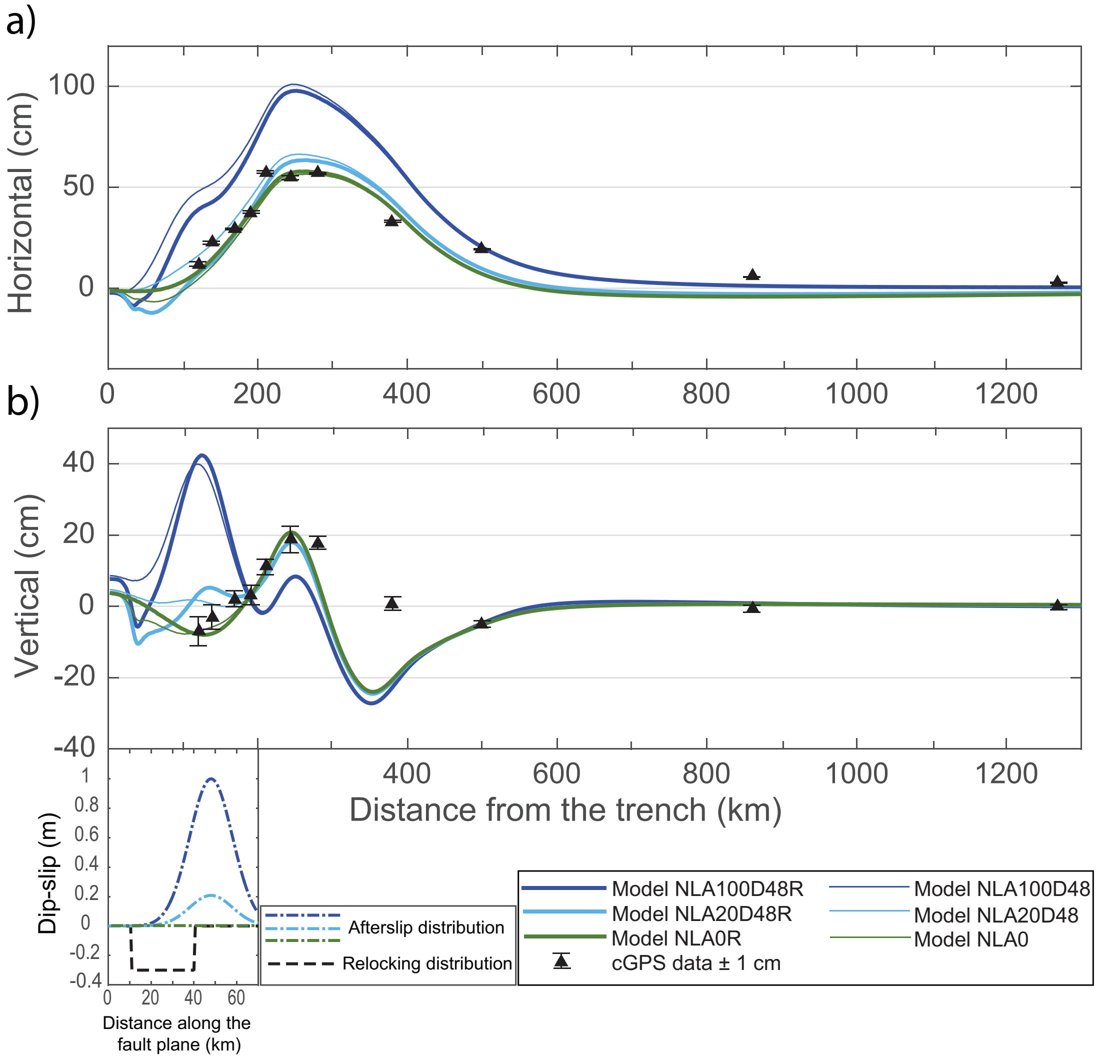

Fig. 3.3 Relative impact of afterslip and relocking for the cumulative surface displacement six years after the Maule event in comparison with cGPS observations. Afterslip and relocking distributions for the six models are shown below the figures at the location relative to the trench. a) Horizontal displacement: Positive values represent trench-ward motion and negative land-ward motion. cGPS displacements are projected onto the model cross section. b) Vertical displacement.

3.3.2 Impact of Afterslip Maximum in Models with Linear Maxwell and Power-Law Rheology

In the second model group, we model the cumulative surface deformation six years after the 2010 Maule event using models with linear Maxwell or power-law rheology and different afterslip magnitudes of 100, 20 and 0 cm that are located at the down-dip limit of the seismogenic zone (Fig. 3.4). We use the same three models with power-law rheology (as in Fig. 3.3), where the afterslip maximum is at 48 km depth and compare these with models that have the same setup, but considering linear Maxwell rheology. Furthermore, despite of the results presented in Fig. 3.3 that show a minor contribution from relocking on the cumulative surface deformation, in Fig. 3.4 we consider all models with relocking after 2 years.

Similar to the results presented in section 3.1, the maximum of afterslip has also an impact on the horizontal and vertical deformation signal for the models with linear Maxwell rheology, but it is smaller than the magnitude inferred using the models with power-law rheology, in particular for the vertical component (Fig. 3.4b). The horizontal component shows the largest differences between models with linear Maxwell and power-law rheology in amplitude and patterns in the near-field among the models, but the difference in the overall pattern is small (). In the far-field all models with linear Maxwell rheology overestimate the horizontal displacement in comparison to the ones with power-law rheology. Significant differences between the models with linear and non-linear rheology are found in particular in the near-field for the vertical component and to lesser extend in the middle and far-field (Fig. 3.4). While models with power-law rheology show uplift at about 200–300 km and subsidence at about 300–700 km from the trench, models with linear rheology show the opposite surface displacement pattern.

In comparison with the horizontal cGPS signal, the overall pattern from the models with linear Maxwell and power-law rheology agrees with the observations equally well in the area of key postseismic deformation, in the Andean region (Fig. 3.4a). However, for the vertical cGPS signal the models with linear Maxwell rheology reveal larger differences with the observed patterns than models with power-law rheology. This holds especially for the area 150–300 km from the trench.

3.3.3 Impact of Afterslip Location on Models with Linear Maxwell and Power-Law Rheology

In the third model group we shift the location of the maximum afterslip of 100 cm from 48 to 35 km and 20 km depth to investigate the impact on the surface deformation in models with linear Maxwell and power-law rheology. The choice of the maximum afterslip location has important effects on the surface deformation. In particular, for the horizontal component, models with linear Maxwell or power-law rheology and shallow afterslip result in a larger surface deformation than those using moderate deep afterslip for distances closer to 100 km from the trench (Fig. 3.5a). Beyond distances of 200 km from the trench, the surface deformation is smaller as shallow afterslip takes place, and it is also in the same fashion as the results from models without afterslip. These differences also apply to the vertical component, mainly in models with power-law rheology (Fig. 3.5b). For models with power-law rheology, the impact is much larger for distances closer to 200 km from the trench than the effect observed in the horizontal component. There, the differences are both in magnitude and patterns. This effect is less pronounced in models with linear Maxwell rheology. These models show a similar pattern of deformation, where the maximum uplift and subsidence are shifted around 40 km toward the trench as afterslip moves to closer distances from the trench on the fault plane.

The different patterns of deformation shown by these models can be compared with the cGPS signal to evaluate the relative impact of afterslip on the surface deformation signal. From models with power-law rheology, our results indicate that they can better explain the overall pattern

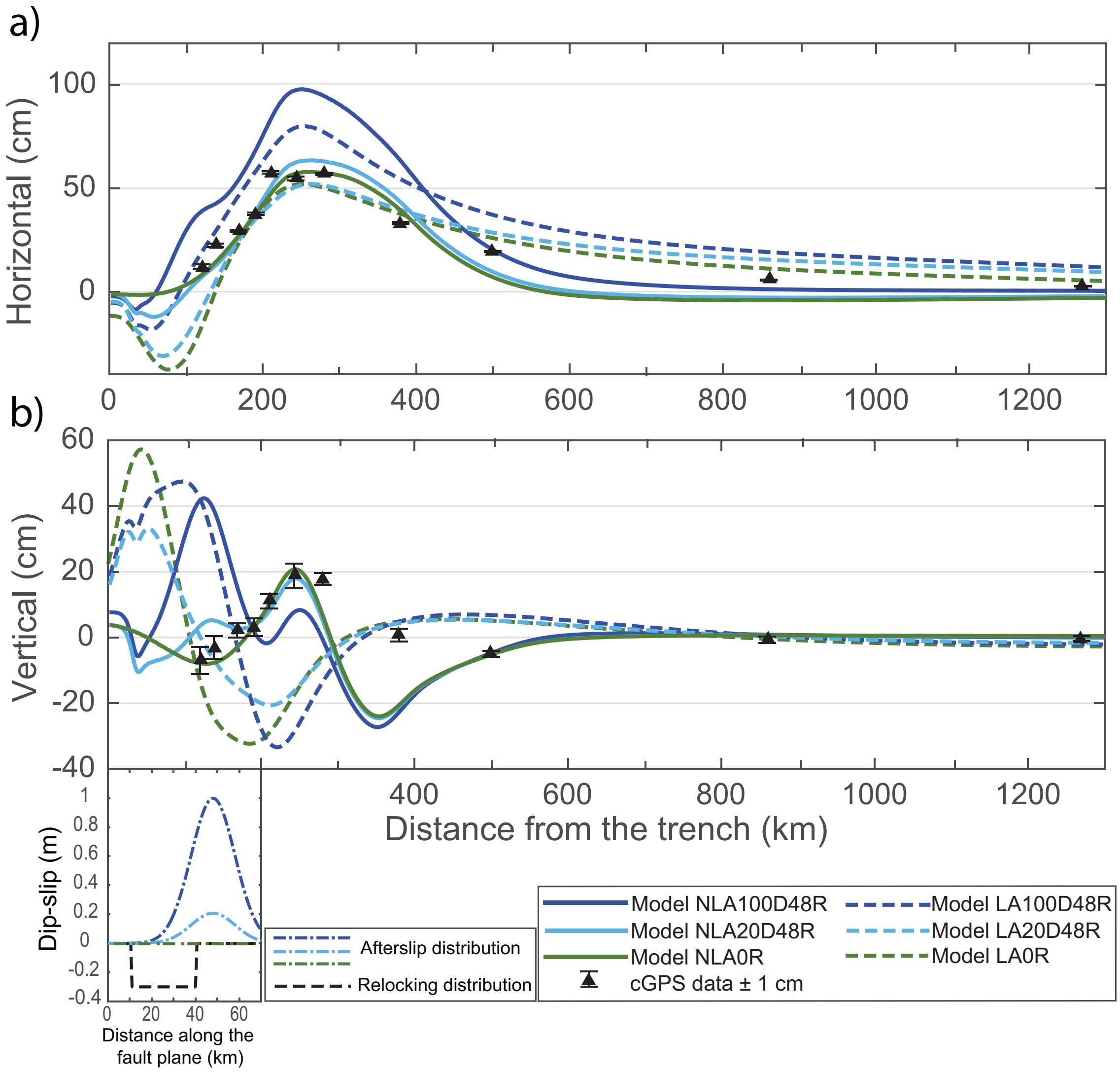

Fig. 3.4 Impact of rheology and afterslip maximum on the cumulative surface displacement six years after the Maule earthquake in comparison with cGPS observations. Afterslip and relocking distributions for the six models are shown below the figures at the location relative to the trench. a) Horizontal displacement. GPS velocities are projected onto the model cross section. b) Vertical displacement.

observed by cGPS where shallow afterslip is considered. In particular, the vertical component gives clear insight to evaluate the relative impact of afterslip location for surface regions closer to 300 km from the trench. Here, the remarkable uplift at about 250 km and small subsidence at about 140 km from the trench can be just explained by the power-law rheology model with maximum afterslip at either 35 km or 20 km depth. None of these models result in very small uplift as shown by one cGPS site about 400 km from the trench. However, beyond these distances, power-law rheology models explain the cGPS displacement pattern.

In summary, the key findings from previous sections are: (1) relocking is not contributing significantly to the cumulative postseismic deformation signal along the chosen model profile; (2) models with linear Maxwell rheology without adaptation of the viscosity structure at depth fail to reproduce the pattern of the observed cumulative vertical postseismic deformation signal regardless of where the maximum afterslip is located and the amplitude of the afterslip; finally,

(c) the general patterns of the cGPS observations are better explained by models with power-law rheology when small values of afterslip at the down-dip limit are considered and/or when afterslip is occurring at shallower regions

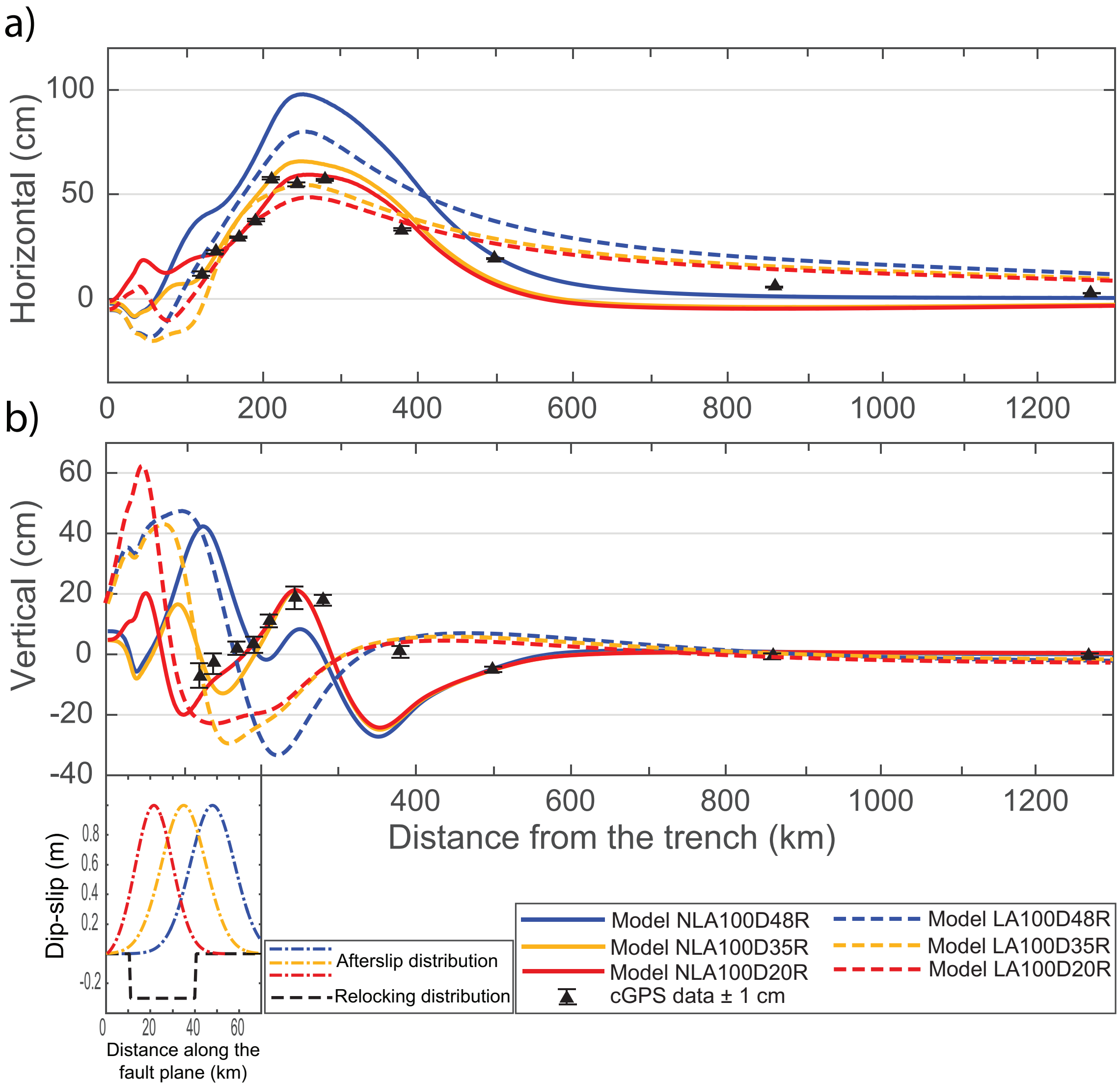

Fig. 3.5 Impact of rheology and location of the afterslip maximum on the cumulative surface displacement six years after the Maule earthquake in comparison with cGPS observations. Afterslip and relocking distributions for the six models are shown below the figures at the location relative to the trench. a) Horizontal displacement. GPS velocities are projected onto the model cross section. b) Vertical displacement.

3.3.4 Model Results Versus Time Series of the cGPS Stations

In this section we analyze the time series for 6 years after the Maule earthquake from four cGPS stations at different distances from the trench and compare these with the models with linear Maxwell and power-law rheology (Fig. 3.6). For this comparison we choose the models with 100 cm maximum afterslip at a depth of 20 km and 0 cm afterslip (Fig. 3.6). We selected the cGPS time series of the stations PELL, QLAP, MAUL and CRRL for comparison, which are located in the near, middle and far field (yellow triangles in Fig. 3.1) at about 130 km, 190 km, 270 km and 500 km distance from the trench, respectively.

The largest differences from models with and without afterslip are found in the near field (cGPS site PELL). As expected, models with afterslip (NLA100D20R and LA100D20R for the power-law and linear Maxwell case, respectively) result in larger deformation than when afterslip is assumed to be zero in particular in the near field. It is also observed that for the two cGPS sites at larger distance from the trench (MAUL and CRRL), the power-law rheology models with afterslip have very close deformation patterns and magnitudes but linear Maxwell rheology models keep small differences after 6 years. For sites at 190 km and 270 km from the trench, models with linear Maxwell and power-law rheology show very similar surface cumulative deformation for the horizontal component; however, there are large differences in the early part of the postseismic phase. In this period, the transient deformation of models with power-law rheology is much faster than linear Maxwell model scenarios, especially at 270 km from the trench where the cGPS MAUL site is located.

By comparing with the cGPS PELL site in the near field, it can be shown that the effect of afterslip is larger than that of viscous relaxation, in agreement with previous studies (Bedford et al., 2013; Hsu et al., 2006). A combination of afterslip and viscous relaxation can resemble the deformation patterns, in particular in the first 2 years. However, after the 2$^{\text{nd}}$ year, the model with power-law rheology can better explain the observed horizontal and vertical postseismic deformation pattern than models with linear Maxwell rheology. Compared with cGPS sites further from the trench, our results indicate that the preferred model also is a combination of power-law rheology and afterslip for both the horizontal and vertical component. Even though the models with Maxwell rheology and afterslip can produce good agreement with the cumulative surface deformation signal, they cannot produce the transient deformation in the early postseismic phase, as observations show. In the far field, at the cGPS CRRL site, no model is in agreement with the early postseismic deformation during the first years for the horizontal component. The vertical component is in very good agreement with models considering power-law rheology. In general, compared with the selected cGPS sites, models with power-law rheology show a better agreement with the overall deformation pattern signal than models with linear Maxwell rheology.

3.4 Discussion

3.4.1 Location of the Viscous Relaxation Process

The largest deformation for models with power-law rheology is produced in a region about 280 km landward from the trench (Fig. 3.7a). Interestingly, most of the viscoelastic relaxation occurs in the lower continental crust. This is in contrast to previous studies in the Chilean subduction zone, since these assumed that the whole crust is an elastic medium above a viscoelastic mantle (Hu et al., 2004; Klein et al., 2016; Li et al., 2018, 2017), resulting in relaxation mainly occurring

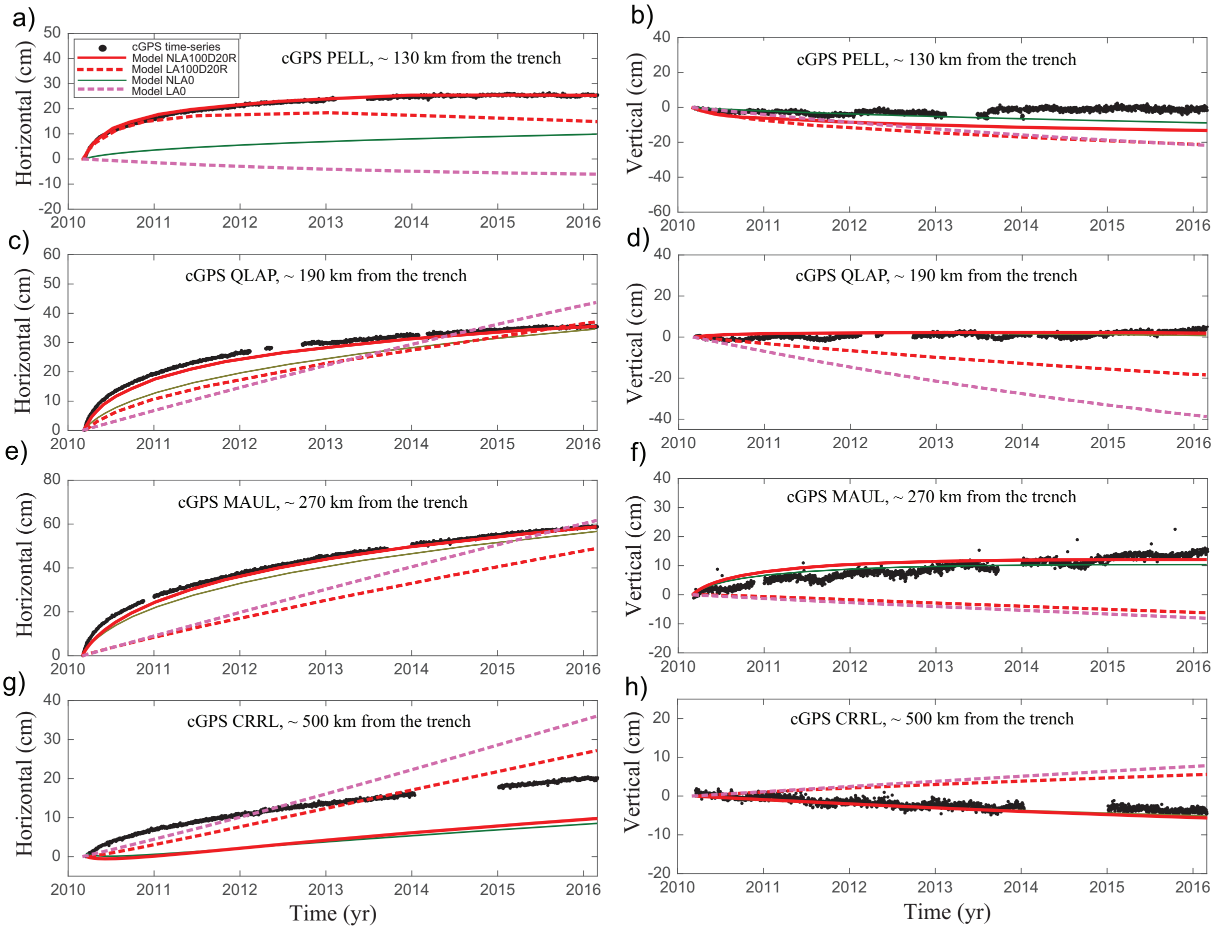

Fig. 3.6 Time series of four cGPS stations versus model results from four models with linear Maxwell and power-law rheology for six years after the Maule event. Black dots are daily solutions of the cGPS observations; distance from the trench is given in km next to the station names. Left row (Figures a, c, e, and g) shows the horizontal displacement. GPS velocities are projected onto the model cross section. Right row (Figures b, d, f, and h) shows the vertical displacement.

in the mantle wedge, in agreement with our model results with linear Maxwell rheology (Fig. 3.7b).

Below the cGPS station MAUL, at 36 km depth, we infer a creep strain after 6 years of 7.9×10^{-5} and an effective viscosity of 1.1×10^{18} Pa s from the power-law model with 1 m of afterslip at 20 km depth. The creep strain and effective viscosity values are very similar for all models with power-law rheology. For the same region but at a shallower depth of only 10 km in the continental crust, we infer after 6 years a creep strain and effective viscosity on the order of 1×10^{-10} and 1×10^{22} Pa s, respectively. The model results using power-law rheology are in good agreement with a brittle upper crust and a ductile lower crust shown by laboratory extrapolation of the rock strength with depth (Brace and Kohlstedt, 1980; Ranalli, 1997). The high creep strain rate in the lower crust predicted by our model may be a result of the vertical geothermal gradient and rock composition at the boundary between the continental lower crust and the upper mantle. These results support the conclusion from Griggs and Blacic (1965) who raised the possibility of great stress relaxation in the deeper crust and uppermost mantle at temperatures far below the melting point. The latter is in agreement with other studies of postseismic relaxation that also consider rock viscosity below the solidus (Barbot, 2018a; Klein et al., 2016; Wang et al., 2012). Hence, this rheologic boundary likely affects geodetic observations of the postseismic deformation at the earth's surface.

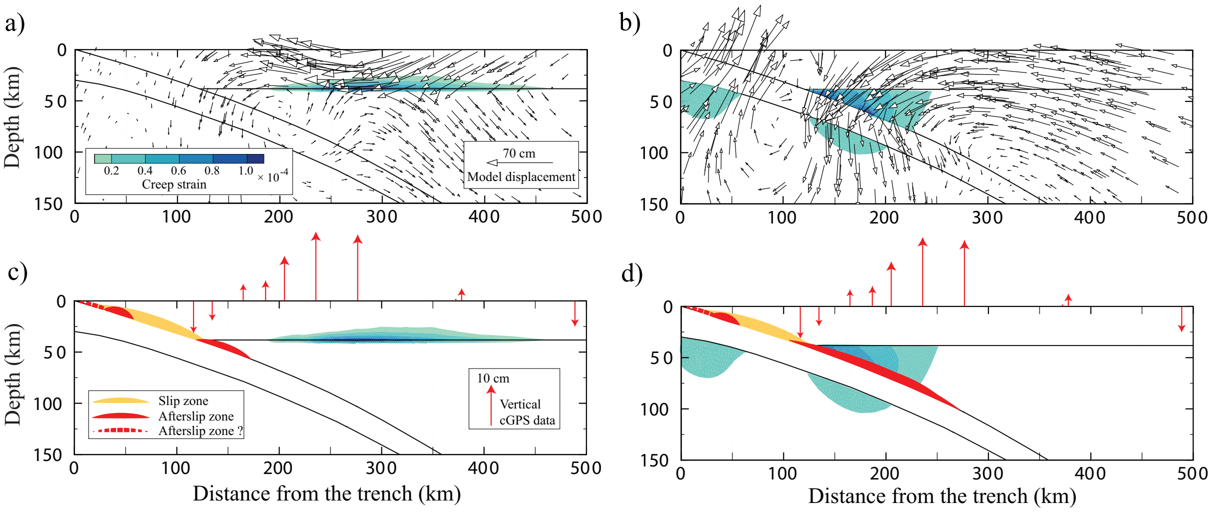

Fig. 3.7 Modeled accumulated displacement field and creep strain 6 years after the Maule earthquake compared with the accumulated observed vertical displacement from nine cGPS stations along the model profile as shown in Fig. 3.1. a Modeled cumulative creep strain (second invariant of the creep strain tensor) and displacement vectors from model NLA0 (power-law rheology, no afterslip and no relocking). b Same as a but with linear model rheology (model LA0). c Schematic representation of where the afterslip occurs in case of the model shown in a. d Same as c using the linear Maxwell model rheology

3.4.2 Implication of Linear Maxwell and Power-Law Model Rheology on Afterslip Location

Uplift deformation observed by cGPS sites at distances between 200 and 300 km from the trench is also found for the postseismic deformation after the great 1960 Valdivia, Chile; 2011 Tohoku-Oki, Japan; great 2004 Sumatra-Andaman, Indonesia and 2015 Gorkha, Nepal, earthquakes (Hu et al., 2004; Muto et al., 2016; Qiu et al., 2018; Wang and Fialko, 2018; Zhao et al., 2017), suggesting that postseismic surface deformation is driven by common relaxation processes. To explain this deformation pattern, our preferred model scenarios are those with power-law rheology and afterslip at the upper part of the fault plane (< 30 km depth) or at the down-dip limit less than 20 cm. Our model results suggest that such a remarkable uplift is mainly the result of stress relaxation in the lower crust due to dislocation creep (Fig. 3.7a), showing that afterslip in a deeper region of the megathrust fault plays a secondary role to explain the uplift pattern at those distances (Fig. 3.7c). The dislocation creep process occurs at distances relatively close to the surface; thus, the deformation produced by this process does not need to be high to explain this pattern. Previous studies showed that this pattern can be explained by using linear viscoelastic rheology in the uppermost mantle in combination with afterslip, especially at the down-dip limit at about 55 km depth or deeper regions (Govers et al., 2018; Klein et al., 2016; Noda et al., 2018; Yamagiwa et al., 2015). In the same fashion, our model results from linear Maxwell model rheology suggest that deeper afterslip is required to explain this pattern (Fig. 3.7d). However, evidence from interseismic locking obtained from GPS velocities (Moreno et al., 2010) or friction laws (Scholz, 1998) along megathrust faults suggests that below approximately 55 km depth the megathrust is probably fully unlocked and no strain is built up to be released as frictional slip after the earthquake. Such a deep aseismic slip may not be only due to frictional processes, but may also occur as strain localization within ductile shear zones. Montési and Hirth (2003) proposed a theoretical model to investigate the impact of dislocation and diffusion creep processes on the transient behavior of ductile shear zones considering grain size evolution. They found that a ductile shear zone resembles frictional afterslip on a deep extension of the fault. This result is also supported by Takeuchi and Fialko (2013). Nevertheless, they found that thermally activated shear zones have little effect of postseismic relaxation. Diffusion creep processes depend strongly on grain size evolution. Here, we have considered the dominance of dislocation creep over diffusion creep processes; therefore, we have not considered grain size evolution. However, further experiments are required to investigate its impact on postseismic deformation, in particular on ductile shear zones along the megathrust fault.

In the very near field (< 50 km from the trench), our results show important differences in the cumulative surface displacement between models with linear Maxwell and power-law rheology, providing a key discriminant between the predominant rheology (linear or non-linear) and the magnitude and location of afterslip. Observations from the postseismic phase of the 2011 Tohoku-Oki earthquake indicated that the impact of afterslip is much smaller than was previously assumed when near-trench time series of GPS stations are used (Sun et al., 2014). Such stations observe a landward motion, which is not in agreement with substantial afterslip at the up-dip limit, which results in a seaward motion. Recently, Barbot (2018a) used a power-law rheology in a 2D model to show that landward motion above the rupture area of the main shock can be produced by transient deformation in the oceanic asthenosphere. Our model with power-law rheology (Model LNA20D48R), in fact, results in a landward motion of $\sim$ 10 cm at 50 km distance from the trench, but since near-trench observations are missing in Chile, it remains a speculation whether landward motion would be observed or not.

3.4.3 Uncertainties of the Temperature Field

The largest uncertainty of the models with power-law rheology originates from the incorporated temperature model since this, besides the stress exponent, is the key control of the effective viscosity and thus the stress relaxation process induced by the coseismic slip and afterslip. Unfortunately, no temperature model exists for the entire cross section of the model, and we thus adopt the model from Springer (1999) that is located in the central Andes at 21°S. There, the age of the oceanic crust is older ($\sim$ 50 Ma) in contrast to the younger plate at 36°S ($\sim$ 35 Ma). Other temperature models closer to the Maule area (Oleskevich et al., 1999; Völker et al., 2011) only provide a temperature field 300 km landward from the trench not covering our model area. In contrast, the Springer model is covering the entire E–W extent of the modeled plate boundary system. Furthermore, Oleskevich et al. (1999) showed that in the fore arc and arc regions at 21°S and 34°S the temperature contours have a very similar pattern, but absolute values can vary by 100 °C and more (Lamontagne and Ranalli, 1996).

To show the model sensitivity due to the initial temperature field T, we increased (Model NLA0T + 100) and decreased (Model NLA0T - 100) the temperatures by 100 °C, respectively (Fig. 3.8). Since we would like to investigate only the impact of viscoelastic relaxation due to temperature changes on the deformation, we considered the model with power-law rheology and without afterslip. The results display a strong impact of the temperature field on the surface deformation, undergoing a maximum surface displacement change by a factor of about two, in the region of largest deformation at the Andean region (Fig. 3.8c, d). Thus, the mismatch of patterns of the slight uplift at about 350 km from the trench and the trench-ward motion in the far field (> 570 km) shown by cGPS observations and our model results, but also obtaining the afterslip, might be due to the temperature uncertainties.

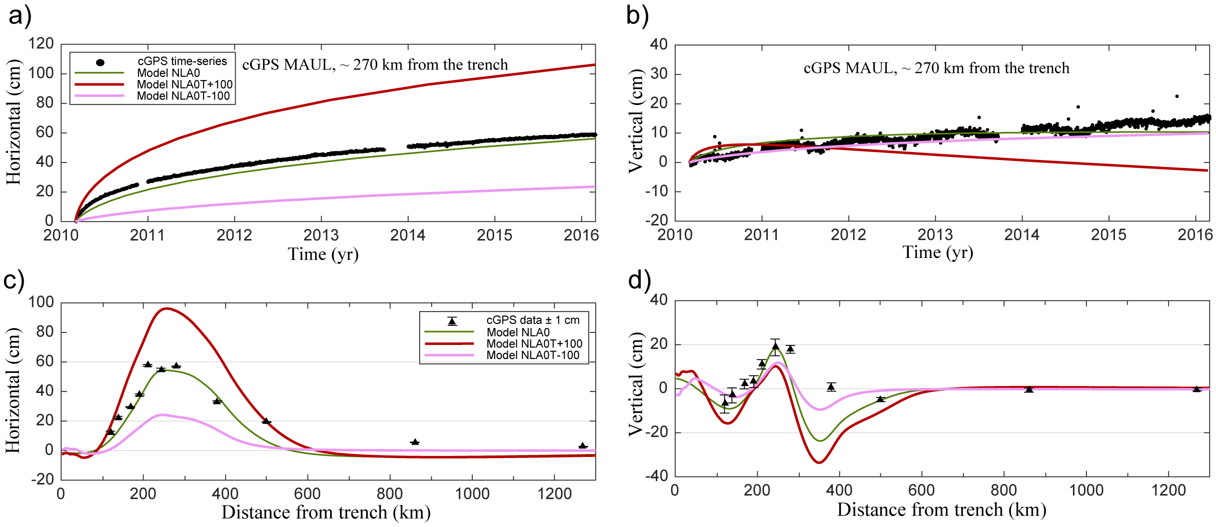

Fig. 3.8 Results of the temperature sensitivity test for the model with power-law rheology. a Time series of the horizontal displacement of the cGPS station MAUL projected onto the model profile compared with model results for the temperature test. b Same as a for the vertical displacement. c Cumulative horizontal displacement of the cGPS stations indicated in Fig. 3.1 after 6 years compared with model results for the temperature test. d Same as c for the cumulative vertical displacement.

3.5 Conclusion

We used a 2D geomechanical-numerical model to study the relative impact of afterslip, relocking and viscoelastic relaxation on the observed postseismic deformation 6 years after the 2010 Maule earthquake. In particular, we tested the general difference of using linear Maxwell or power-law rheology. The overall impact of relocking is only visible at distances < 200 km from the trench, but small compared with afterslip and viscoelastic relaxation. For the cumulative horizontal displacement the overall pattern from models with linear Maxwell and power-law rheology is similar. However, for the cumulative vertical displacement this is different. Here the used afterslip magnitudes as well as its depth location have a different expression in the modeled cumulative vertical displacement. To reproduce the pattern of the cGPS observations, the model with power-law rheology requires afterslip in shallower regions at 20—30 km depth rather than afterslip at depth > 50 km as suggested by models with linear rheology (Bedford et al., 2016; Klein et al., 2016). It also seems that less afterslip is needed at shallow depths. This difference is due to the different processes that are induced. In the models with power-law rheology the coseismically induced differential stresses in the lower crust and upper mantle are relaxed in shallower regions, i.e., the lower crust, whereas the models with linear Maxwell rheology assume that the crust is elastic. To produce the same vertical postseismic displacement these models require a relatively high afterslip at greater depth. To discriminate which model assumption is ultimately controlling the postseismic relaxation processes, cGPS stations near the trench are needed, and these turning points between subsidence and uplift as well as the change in direction of the horizontal displacement toward or away from the trench could be used as a proxy for the location and amount of afterslip as well as for the depth where differential stresses are relaxed by linear or non-linear viscoelastic processes.

Chapter 4

Impact of Power-Law Rheology on Afterslip Distribution and Viscoelastic Pattern Following the Postseismic Deformation Associated to the 2010 Maule Earthquake

Abstract

After large earthquakes at subduction zones, the plate interface continues moving due to mostly frictional afterslip or simply afterslip processes. Below depths of 60 km, little afterslip is to be expected on plate interface due to low shear strength, lack of apparent geodetic interseismic locking, and low seismic moment release from aftershocks. However, inversion models that employ linear viscoelastic mantle rheology and an elastic crust result in a significant portion of afterslip at depths > 60 km. In this paper, we present a combination of a 3D forward geomechanical-numerical model with power-law rheology that simulates postseismic relaxation with dislocation creep processes in the crust and upper mantle and an afterslip inversion. We estimate the cumulative viscoelastic relaxation and the afterslip distribution for the first six years following the 2010 M_w 8.8 Maule earthquake in Chile. The cumulative afterslip distribution is obtained from the inversion of the residual surface displacements between the observed displacements from the continuous GPS (cGPS) and the ones from the forward modelling. We investigate five simulations, four with different dislocation creep parameters for the crust, slab, and upper mantle and one with elastic properties for the crust and slab, and a linear viscoelastic upper mantle for comparison. Our preferred simulation considers a weak crust since it shows the best fit to the cumulative cGPS postseismic displacements, a good fit to the time-series, and, in particular, a good spatial correlation between afterslip and aftershock activity. In this simulation, most of the viscoelastic relaxation occurs in the continental lower crust beneath the volcanic arc due to dislocation creep processes. The resulting afterslip pattern from the inversion is reduced at depths > 60 km, which correlates to the low cumulative seismic moment that is released from aftershocks at these depths. Furthermore, the cumulative afterslip moment release from this simulation corresponds to 10% of the main shock in six years, which is approximately half of the moment release that results from models with an elastic crust and linear viscosity in the upper mantle. We conclude that an integrated analysis by considering power-rheology with dislocation creep processes in the continental crust and upper mantle along with aftershock activity may be used to constrain location and magnitude postseismic relaxation processes better.

Highlights

- Six years of postseismic displacements after the 2010 Maule earthquake from GPS data.
- Combination of 3D forward modelling with power-law rheology and afterslip inversion.
- Inverted deep afterslip patterns strongly depend on the choice of rheology model.
- Continental lower crustal viscoelastic relaxation reduces need for deep afterslip.
- Use of aftershock activity to discriminate simulations.

4.1 Introduction

In the years following large magnitude earthquakes, the surface deformation is transient and occurs at high and variable rates, generally decaying with time. This postseismic deformation is a superposition of afterslip at the plate interface which seems to surround the plate interface regions that had the largest coseismic slip (Bedford et al., 2013; Hsu et al., 2006; Perfettini and Avouac, 2007; Perfettini et al., 2010), poroelastic rebound in the oceanic and continental crust (Hu et al., 2014; Masterlark, 2003) and viscoelastic relaxation of co-seismically induced differential stresses in the continental crust and upper mantle (Freed and Bürgmann, 2004; Freed et al., 2017; Hergert and Heidbach, 2006; Peña et al., 2019; Qiu et al., 2018; Sun et al., 2014; Wang et al., 2012). The contribution of poroelastic rebound is small compared to afterslip and viscoelastic relaxation processes, but the relative contribution of the latter two processes is not clear and strongly depends on the incorporated model rheology.

Afterslip distribution following earthquakes has been usually investigated using linear inversion and, to a lesser extent, self-consistent stress-driven approaches that model the observed postseismic cGPS surface displacements. The existing models are quite different and consider fully elastic rheology (Aguirre et al., 2019; Bedford et al., 2013; Perfettini et al., 2010), use the residual between the surface postseismic displacements and the results from a forward model of the postseismic relaxation with linear viscoelastic rheology (Bedford et al., 2016; Freed et al., 2017) or consider the afterslip-viscoelastic coupling with linear and non-linear viscoelastic relaxation processes (Agata et al., 2019; Barbot, 2018a; Lambert and Barbot, 2016; Masuti et al., 2016b; Muto et al., 2019; Rollins et al., 2015; Rousset et al., 2012a; Shi et al., 2020a; Tsang et al., 2016; Yamagiwa et al., 2015). At subduction zones, these models showed that generally afterslip dominates near field and viscoelastic processes far field, but the use of close-to-trench GPS observations after the 2011 Tohoku-oki earthquake, Japan, revealed that viscoelastic relaxation in the oceanic mantle may also contribute considerably to the near field signal (Agata et al., 2019; Freed et al., 2017; Sun et al., 2014). Yet, the contribution of afterslip and viscoelastic relaxation processes to the surface deformation field cannot easily be distinguished based on near-field and far-field cGPS observations (Weiss et al., 2019). The incorporation of viscoelastic relaxation processes in the mantle reduces the deep afterslip and increases the shallow afterslip compared to a model with fully elastic properties (Qiu et al., 2018; Sun et al., 2014; Tsang et al., 2016). Nevertheless, even with the inclusion of viscoelastic relaxation in the upper mantle, these model settings generally result in considerable afterslip at depths > 60km from the inversion. For instance, the afterslip model of Yamagiwa et al. (2015) results in afterslip of ∼2m at 80 km depth after 2.5 years of the 2011 Tohoku-oki earthquake in Japan. Similar results were found in the Sumatra-Andaman region with afterslip values of ∼1.5-3 m at the same depth by Tsang et al. (2016) and Qiu et al. (2018).

However, large afterslip at depths > 60 km is apparently not in agreement with frictional properties and shear strength of the megathrust inferred from seismic wave radiation (Lay et al., 2012), friction laws (Agata et al., 2019; Avouac, 2015) and the low aftershock activity (Agurto-

Detzel et al., 2019; Lange et al., 2014, 2012; Lay et al., 2012). Recently, Agata et al. (2019) combined a model with stress-driven afterslip considering laboratory-derived friction laws and non-linear rheology for the upper mantle. Their results indicate that afterslip mainly occurs at depth < 60 km after 2.8 years of the 2011 Tohoku-oki earthquake in Japan. This depth is in the temperature range of 300–450 °C for the Tohoku-oki region, Japan (Wada et al., 2015), which represents the onset of brittle-ductile transition (Scholz, 1988), i.e., the down-dip limit of the seismogenic zone. Nevertheless, this transition varies among subduction zones (Oleskevich et al., 1999; Shi et al., 2020b), mainly because of age and velocity of the incoming plate (Oleskevich et al., 1999; Völker et al., 2011). On the other hand, geodetic interseismic locking (Avouac, 2015; Li et al., 2018; Loveless and Meade, 2010; Moreno et al., 2010; Métois et al., 2012) indicates that the down-dip limit of the seismogenic zone is approximately 50 km at most subduction zones.

The distribution of afterslip following the 2010 M_w 8.8 Maule earthquake in Chile has been investigated in a number of studies, each using different elastic and viscoelastic model configurations (Aguirre et al., 2019; Bedford et al., 2013, 2016; Klein et al., 2016; Lin et al., 2013; Peña et al., 2019; Weiss et al., 2019). Results from each study differ significantly indicating that the incorporated model rheology for the upper mantle and continental crust has a major impact on the afterslip distribution at the plate interface. For example, models that use an elastic rheology for the crust and mantle result in afterslip with a maximum of up to 2 m mainly between 25–50 km depth, but also significant afterslip at depths > 60 km (Bedford et al., 2013; Lin et al., 2013). The study of Klein et al. (2016) uses a model with Burgers rheology with a linear viscosity of 4.75×10^{18} Pa s for the upper mantle below an elastic crust. They also include a deep subduction channel with viscosities close to 10^{17} Pa s at depths between 55–135 km, limiting the afterslip distribution to a shallower region (< 55 km depth) with a maximum of $\sim$9 m over the first year. Weiss et al. (2019) used a model that jointly inverts for viscous strain in the continental lower crust and upper mantle and afterslip at the plate interface. Their maximum afterslip is up to 8 m and mostly concentrated in the vicinity of the trench at > 20 km depth, while viscoelastic relaxation in the lower crust has little impact of the postseismic signal at the surface. In contrast, Peña et al. (2019) showed that stress relaxation in the continental lower crust due to non-linear dislocation creep processes reduces the maximum afterslip to $\sim$1 m and shift it to deeper regions between 20–35 km depths. However, their work is a semi-generic study using a 2D geomechanical forward model in which the afterslip distribution is pre-defined as a boundary condition rather than an inversion to explain residual GPS postseismic surface displacements. A 3D model for the Maule postseismic deformation that accounts for dislocation creep processes in a forward sense and then obtains the afterslip distribution on the plate interface from the residual displacements between the observed and the viscoelastic forward simulation is still missing. The postseismic deformation associated to the Maule event has important deformation features along-strike (Bedford et al., 2013; Klein et al., 2016; Li et al., 2017); therefore, a 3D model may give a more integrated understanding of the driven processes rather than a 2D approach that assumes plain strain in the along-strike direction.

Thus, in this study we extend the 2D model of Peña et al. (2019) into a 3D model using a power-law rheology with dislocation creep for the crust and upper mantle. Furthermore, we now combine the postseismic forward modelling of viscoelastic relaxation with a standard linear inversion to estimate the cumulative afterslip distribution on the plate interface six years after the main shock. We use the observed surface displacements from 55 cGPS stations as shown in Fig. 4.1. Our primary goal is to investigate the impact of rheology (linear and power-law) on the inverted afterslip distribution using a range of plausible dislocation creep parameters for the continental crust and the upper mantle, as well as the linear rheology case (elastic crust and linear viscoelastic mantle). Our results show that the moment release by afterslip is 10-14% of the main shock. Furthermore, we find that simulations that result in viscous deformation in the continental lower crust concentrate the afterslip to depths < 60 km. The afterslip distribution from our preferred simulation is chosen from its lowest residual between the observed and simulated surface displacements as well as its good correlation with the accumulated moment release from the aftershocks at the plate interface.

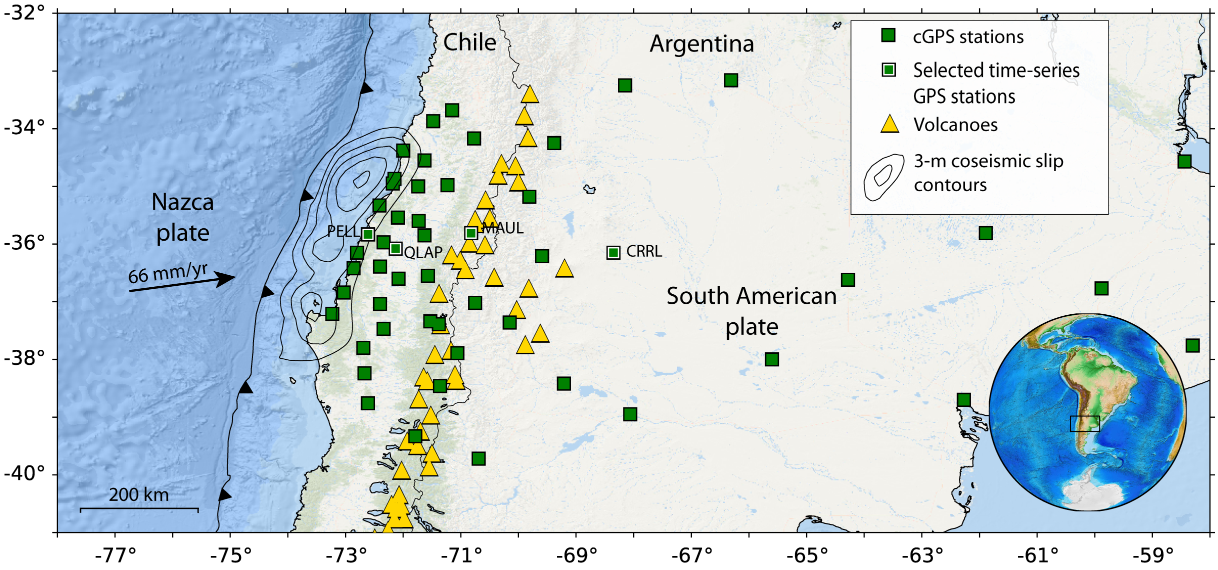

Fig. 4.1 Study area with location of cGPS stations used in this study. Grey contour lines depict the area of coseismic slip of the 2010 Maule earthquake taken from Moreno et al. (2012). Stations shown by a white border and their station names are the ones to be compared with displacement time series from the model results (see A.5).

4.2 Model set up and cGPS data

We estimate the afterslip distribution on the plate interface with a combination of a 3D geomechanical forward model and an inversion approach (Fig. 4.2). The 3D viscoelastic forward model describes the postseismic relaxation for the first six years after the 2010 Maule $\mathrm{M_w}$ 8.8 earthquake using linear and power-law rheology. The resulting cumulative predicted surface displacements are subtracted from the observed displacements at the cGPS stations in the model area. After that, the cumulative residual displacements are used in a linear inversion to finally estimate the afterslip at the plate interface. More details on the two models and the cGPS data are presented in the two following subsections.

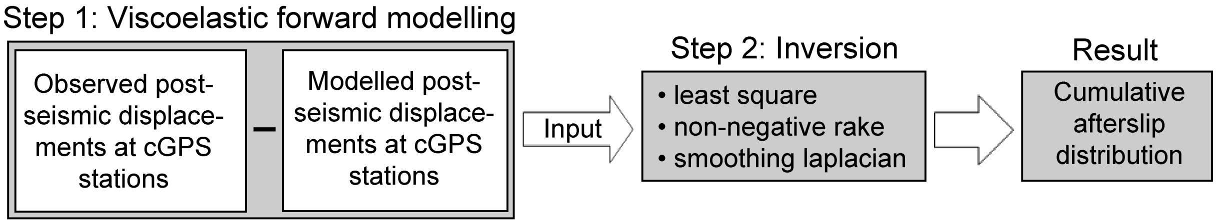

Fig. 4.2 Sketch of the model workflow that combines a forward model of the postseismic viscoelastic relaxation with an inversion for the cumulative afterslip distribution at the plate interface six years after the main shock. The input of the inversion model is the residual between the cumulative postseismic displacements at the cGPS stations and the results of the forward simulation at the cGPS stations after six years.

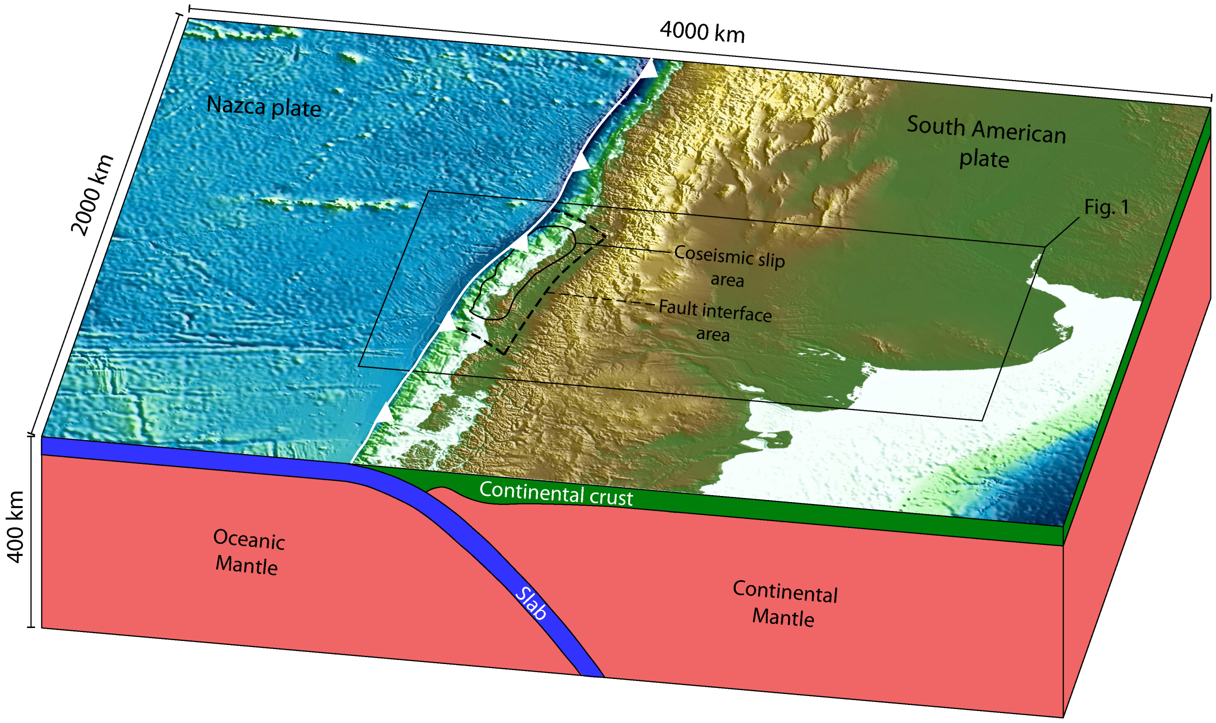

Fig. 4.3 Model geometry and study area with twofold exaggeration in vertical direction. At the lateral and lower model boundary normal displacements are not allowed while the surface is free of constraints. Assigned coseismic slip greater than 3m is shown by black solid contour lines; dashed rectangular box indicates the domain of the afterslip inversion on the fault interface. Rectangular box shows the location of the study area presented in Fig. 4.1

4.2.1 Set up of the forward model

The model geometry of the forward model to describe the viscoelastic relaxation includes the slab from Hayes et al. (2012) and the Moho from Tassara et al. (2006). It extends 4000 km in

West-East direction, 2000 km in North-South and 400 km in the vertical direction (Fig. 4.3). This size is large enough to avoid artefacts that result from the model boundary conditions.

At steady state, and under high-temperature and high-pressure conditions, rocks deform predominantly due to dislocation creep processes described by equation:

$$\dot{\varepsilon} = A\sigma^n e^{\frac{-Q}{RT}} \tag{4.1}$$

While a linear viscoelastic material with effective viscosity (η) deforms as:

$$\dot{\varepsilon} = \frac{\sigma}{2\eta} \tag{4.2}$$

where $\dot{\varepsilon}$ is the strain rate, A is a pre-exponent parameter, σ the differential stress, n the stress exponent, Q the activation enthalpy for creep, R the gas constant and T the absolute temperature (Freed and Bürgmann, 2004; Hirth and Kohlstedt, 2003; Masuti et al., 2016b; Wang et al., 2012). Studies from laboratory experiments in lithospheric rocks (Carter and Kirby, 1978; Chopra, 1997) and postseismic deformation following large-magnitude earthquakes (Agata et al., 2019; Freed et al., 2012; Masuti et al., 2016b) suggest a more rapid initial transient deformation than the one from the power-law formulation in equation 4.1. Here, we neglect this rapid initial transient response since its impact is small in comparison to the large uncertainty that result from the temperature models (Ranalli, 1997; Völker et al., 2011) and creep parameters (Hirth and Kohlstedt, 2003, 1996; Ranalli, 1995). We thus model the viscoelastic relaxation with power-law and linear rheology using equations 4.1 and 4.2, respectively. Details on the rock properties are presented in section 4.2.4. The temperature field for our model is adopted from Völker et al. (2011). Since the domain of this temperature model is 2D only and laterally smaller than ours, we first take the isotherms at the borders of the temperature model and extend them to our model's boundaries. This assumption is justified as there are no relevant changes in the slab geometry and age in the key postseismic deformation area, which are controlling factors in the thermal structure (e.g, Völker et al., 2011). Finally, we interpolate the temperature field and assign the corresponding temperature to each node in the 3D model domain (Fig. A.1). We assume that the implemented temperature field is time-independent because no significant changes are expected during our model time of six years.

At the lateral and bottom model boundaries displacement is only allowed in a boundary-parallel direction; the model surface is free of constraints. To initiate the postseismic deformation we simulate the coseismic rupture of the Maule M_w 8.8 earthquake on a fault that is ~700 km long in strike direction and ~90 km deep. The relative displacement of the hanging and foot walls is governed by linear constraint equations that satisfy the specified slip at each node-pair (Freed et al., 2017; Masterlark, 2003). Here, we apply the coseismic slip of Moreno et al. (2012) as displacement boundary conditions. We employ this slip model because we use the same elastic material properties and model geometry as implemented in the model of Moreno et al. (2012). The resulting coseismic deformation is consistent with the observed coseismic deformation at the GPS stations (Fig. A.2).

Since power-law rheology is stress dependent, we evaluate the effects of background stresses with the 2D model of Peña et al. (2019). We find no substantial differences in the cumulative six-years postseismic displacements (Fig. A.3 and A.4); therefore we assume in the following that background stresses can be disregarded. Thus, the differential stress changes imposed by the coseismic slip cause the onset of the dislocation creep processes with rates depending on the dislocation creep parameters. The model volume is discretized into 2,350,000 finite elements with high resolution close to the area of key postseismic deformation ($\sim$5 km) and significant coarser resolution (*sim*50 km) at the model boundaries where no deformation is expected. The resulting numerical problem is solved with the commercial finite element software ABAQUS^{TM}, version 6.11.

Table 4.1 Elastic properties and creep parameters

Rock type[b]	Young's module E (GPa)[a]	Poisson's ratio[b]	Pre-exponent A (MPa^{-n} s^{-1})[b]	Stress exponent n[b]	Activation energy Q (kJ mol^{-1})[b]
Wet quartzite	100	0.265	3.2×10^{-4}	2.3	154
Wet olivine 1*	160	0.25	5.6×10^{6}	3.5	480
Wet olivine 2*	160	0.25	1.6×10^{5}	3.5	480
Diabase	160	0.3	2.0×10^{-4}	3.4	260

[a] Reference source from Christensen (1996) and Moreno et al. (2012)
[b] Reference source from Hirth and Kohlstedt (2003) and Ranalli (1997))
* Wet olivine 1 and 2 contain 0.1 and 0.005% of water, respectively

4.2.2 Continuous GPS observations

The postseismic deformation associated with the 2010 M_w 8.8 Maule earthquake in Chile was well recorded by a rapid international collaborative effort under which 67 cGPS stations were installed (e.g., Vigny et al., 2011). We use the first six-years of the postseismic surface displacements observed by cGPS as reported by Li et al. (2017). In this data set, the cumulative surface displacements at cGPS stations are obtained from daily solutions processed at Nevada Geodetic Laboratory (University of Nevada, U.S., Blewitt, 2018), where the cGPS time series are processed in the IGS08 reference frame (Rebischung et al., 2012). Li et al. (2017) considered only stations with more than 4 years of temporal coverage, obtaining a total of 55 cGPS stations that fulfill this criterion. Furthermore, they applied the trajectory model of Bevis and Brown (2014) and removed the effect of seasonal variations, aftershock and/or jump signals. We also removed the secular component by identifying the interseismic displacements at each postseismic GPS stations from previous studies (Moreno et al., 2010; Métois et al., 2012).

4.2.3 Afterslip inversion

The input for the inversion model of the afterslip is the residual between the results of the forward model of the cumulative postseismic relaxation after six years and the cGPS data as described in Fig. 4.2. We use this residual signal to invert for the afterslip distribution by calculating the Green's functions at each node-pair using linear equations that satisfy the static dislocation of node-pairs by imposing kinematic constraints as described by Masterlark (2003). Following the approach from previous studies considering forward simulation for the viscoelastic response and an inversion for the afterslip (Bedford et al., 2013; Freed et al., 2017), the Green's functions for the afterslip inversion are calculated from the 3D model by considering only the elastic material properties stated in Table 4.1. The inverse problem is solved with a least squares method, a non-negative rake varying from 0 to 180° (i.e., afterslip in down-dip direction is not allowed), and Laplacian smoothing constraints that minimize the differences among neighboring node-pair dislocations (Bedford et al., 2016; Freed et al., 2017). Here, the smoothing constants are chosen from the trade-off curve between the residual norm and the solution length (Bedford et al., 2016; Masterlark, 2003; Moreno et al., 2012) (more information in Fig. A.8).

Our approach implies that afterslip and viscous relaxation are assumed to act independently from each other. However, the rate and magnitude of afterslip will indeed change the stress state, potentially affecting the viscous response. To investigate this, we combined afterslip and power-law rheology and compare the results to assess to what extent these processes are coupled. In the first case, we use the 3D model to jointly simulate six-year postseismic deformation with the afterslip and rheology from our preferred simulation. In the second case, acting independently, the surface postseismic displacements over six years are the sum of afterslip and viscoelastic processes simulated separately using the 3D model. The afterslip distribution on each node adopts a decay law as shown by aftershock seismicity in both cases (Agurto-Detzel et al., 2019; Bedford et al., 2016; Lange et al., 2014; Perfettini and Avouac, 2007). We find that the coupling with afterslip increases the total surface displacement by less than 6% (Fig. A.5). Similar findings are presented by Freed et al. (2017) who investigated the postseismic deformation after the M_w 9.0 2010 Tohoku earthquake in Japan. Therefore, we concluded that it is a reasonable approach to separately investigate the viscoelastic relaxation and afterslip contributions to the postseismic deformation.

4.2.4 Rheological parameters of the five simulations of the forward model

For the four simulations PL1-PL4 with dislocation creep we assume that the rheology of the slab is controlled by diabase rock and the one of the oceanic upper mantle by the mineral olivine with 0.005 wt.% of water content because of their well-known rock composition and water content from a mid-ocean ridge basalt (MORB) source (Hirth and Kohlstedt, 1996). In simulation PL1 and PL2 we combine a wet quartzite for the continental crust with the two dislocation creep parameters for the continental mantle, that is wet olivine with 0.005 wt.% and 0.1 wt.% of water, respectively. In contrast, simulation PL3 and PL4 instead use a diabase for the continental crust

Table 4.2 Configuration of simulations

Simulation	Rheology	Continental crust	Continental mantle	Slab	Oceanic mantle
PL1	Power-law	Wet quartzite	Wet Olivine 1	Diabase	Wet olivine 2
PL2	Power-law	Wet quartzite	Wet Olivine 2	Diabase	Wet olivine 2
PL3	Power-law	Diabase	Wet Olivine 1	Diabase	Wet olivine 2
PL4	Power-law	Diabase	Wet Olivine 2	Diabase	Wet olivine 2
LI5	Linear Maxwell	Elastic*	1.3×10^{19} Pa s	Elastic*	1.3×10^{19} Pa s

* Elastic properties (Young's modulus and Poisson's ratio) for the continental crust and slab as described in Table 4.1 for wet quartzite and diabase, respectively.

and the same dislocation creep parameters for the continental mantle as simulations PL1 and PL2. Finally, in simulation LI5 we assume that the crust is linear elastic and that the postseismic relaxation in the upper mantle is controlled by linear viscoelasticity with a viscosity of 1.3×10^{19} Pa s in agreement to previous studies for the Chilean subduction zone (e.g., Bedford et al., 2016; Peña et al., 2019). The elastic and dislocation creep parameters of simulations and configuration of each simulation are presented in Table 4.1 and Table 4.2, respectively.

4.3 Results

In the following we present the results of five parameter sets of the forward model. Four of these use power-law rheology with dislocation creep (simulations PL1-PL4) and one uses a linear viscoelastic rheology (simulation LI5) as listed in Table 1.2. The inversion parameters used to produce all five afterslip distributions are identical.

4.3.1 Horizontal and vertical surface displacements

Fig. 4.4 shows for all five simulations the modelled displacement (the sum of the cumulative postseismic relaxation after six years and the inverted afterslip) and the observed displacement at the cGPS stations. The overall displacement patterns of the horizontal component are well captured by all simulations but larger discrepancies are found in the vertical component in the volcanic arc and back arc areas. Simulations PL1-PL4 using power-law rheology can better explain the fast uplift in the volcanic arc and subsidence in the back arc than the linear rheology simulation LI5, which results in opposite patterns to the observed uplift at station MAUL in the middle and subsidence at station CRRL in the far fields. The change from the observed uplift to subsidence in the back arc is slightly better explained by simulation PL4, but the amplitude of the horizontal displacement is not well captured. Furthermore, the observed cumulative displacements on the coast line are well fit-ted by all simulations, suggesting that near-field observations are mainly dominated by afterslip processes as already pointed out by previous studies (e.g., Bedford et al., 2013; Qiu et al., 2018).

To quantify the deviations between model results and cGPS data, we calculate the Mean Absolute Error (MAE) for each simulation separately for the cumulative total, horizontal and vertical displacements after six years. The smallest MAE is achieved by simulation PL1 with 4.0 cm (Fig. 4.4a). Compared to simulation PL1 there is an increase of the total MAE of 20%, 15%, 48% and 23% for simulations PL2, PL3, PL4, and LI5, respectively. Interestingly there is a trade-off between the quality of the fit of the horizontal and the vertical cumulative displacements. For example, simulation PL4 (Fig. 4.4d) has the largest MAE with 5.9 cm, but the smallest error in the vertical (MAE=3.4 cm) and the largest error for the horizontal displacement (MAE=7.2 cm) while simulation LI5 can explain the horizontal displacement best (MAE=3.8 cm), but the vertical displacement has the worst fit (MAE=6.7 cm). The latter originates mainly from a poor fit to observed displacements at the cGPS stations located in the volcanic and back arcs (Fig. 4.4e).

We also investigate the main features in the surface displacement patterns over time by comparing simulation PL1, which has the lowest MAE with 4.0 cm in comparison to simulation LI5. To account for the temporal decay of afterslip, we applied a decay law for the afterslip with the shape of the aftershock seismicity decay. This is support by previous studies which found a good correlation between the temporal evolution of the afterslip and aftershock seismicity (Aguirre et al., 2019; Lange et al., 2014; Perfettini and Avouac, 2007). To gain insight into the main surface deformation differences between models with linear and non-linear rheology, in Fig. 4.5 we show and compare the time-series of four cGPS stations located in the near field (PELL), middle field (MAUL and QLAP) and far field (CRRL) with the combined results of the forward and inversion model. Additional time-series comparison is found in Fig. A.6. We find that the largest differences are shown in the displacement rates. Even though the simulation with linear rheology can best explain the cumulative horizontal displacement (smallest MAE in the horizontal component), it does not reproduce convincingly the time-series of the postseismic displacements in the first years compared to simulation PL1 (Fig. 4.5b-c and Fig. A.6f-i). This has also been shown by Freed and Bürgmann (2004) for the postseismic deformation associated to the 1992 Landers and 1999 Hector Mine earthquakes and Peña et al. (2019) for the Maule case. This is shown at cGPS stations QLAP and MAUL, where simulation LI5 underestimates the observed fast surface displacements, especially in the first two years.

4.3.2 Afterslip inversions

Fig. 4.6 shows the resulting afterslip distributions on the plate interface from the inversions of all five simulations. For power-law simulations PL1–PL4 the afterslip pattern is similar between 20–60 km depths except for changes in the amplitude. Simulation LI5 with linear rheology, however, shows a different pattern at these depths as we will present in this section. All simulations show afterslip maximums surrounding the maximum coseismic slip, which are regions of moderate coseismic slip. The maximum afterslip is located north of the maximum

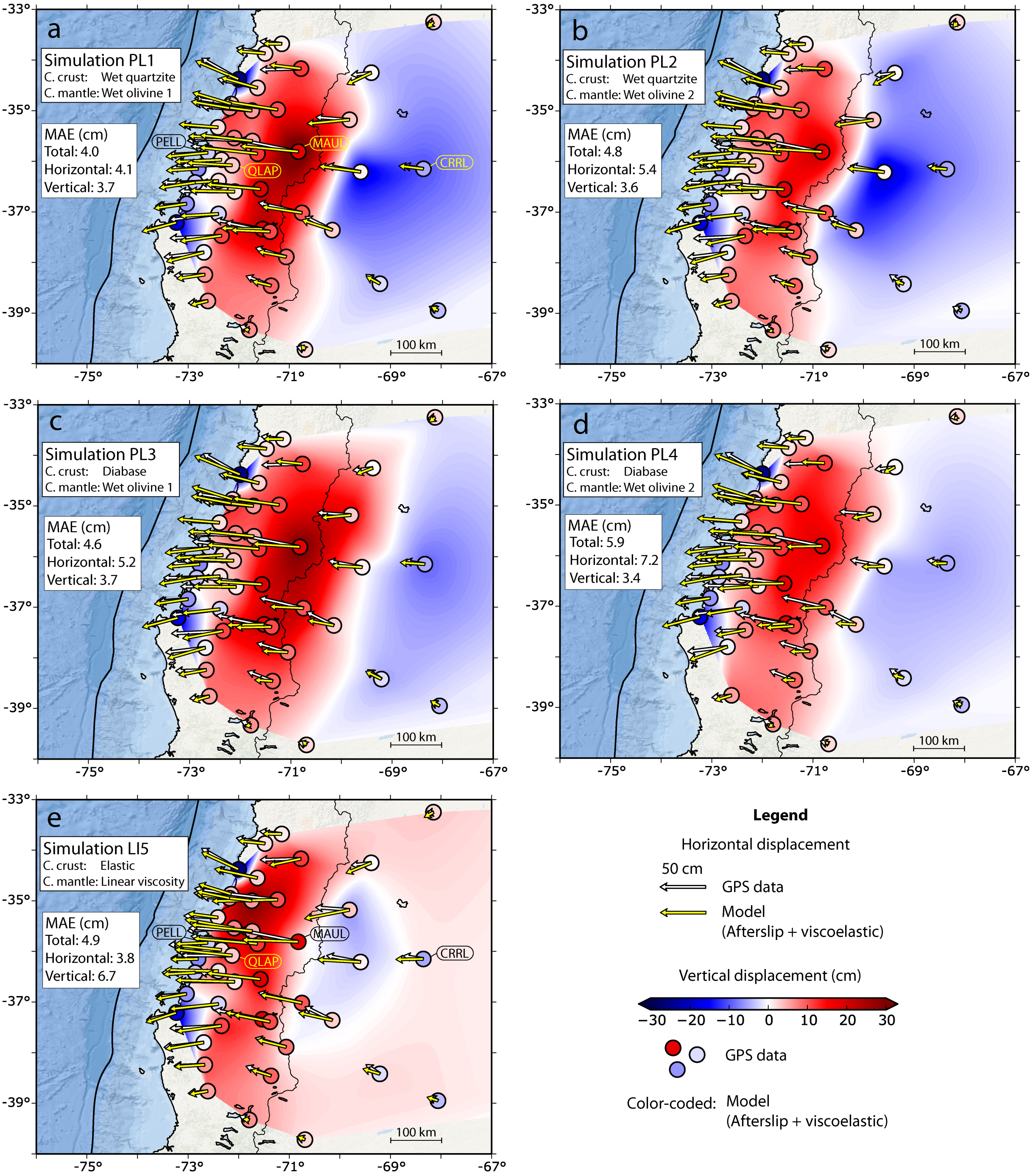

Fig. 4.4 Observed versus modelled cumulative surface displacements after six years from the cGPS stations shown in Fig. 4.1. Only inland surface displacements are shown. MAE represents the Mean Absolute Error. The modelled surface displacement is the sum of the viscoelastic relaxation from the forward model and the resulting afterslip from the inversion.

coseismic slip at 20km depth in all simulations and reaches a maximum of ∼3m for power-law rheology simulations and 3.7 m for the simulation with linear rheology. The afterslip in the vicinity of the up-dip region of the megathrust fault is relatively small in all simulations; in zones of poor resolution (Figs.S7 and S8), no afterslip is resolved at < 15 km depth in simulation PL1 and small afterslip (< 0.4 m) at this region is apparent for the other simulations. Interestingly, all simulations show that the afterslip pattern is concentrated in two bands between 34.5–37.5°S

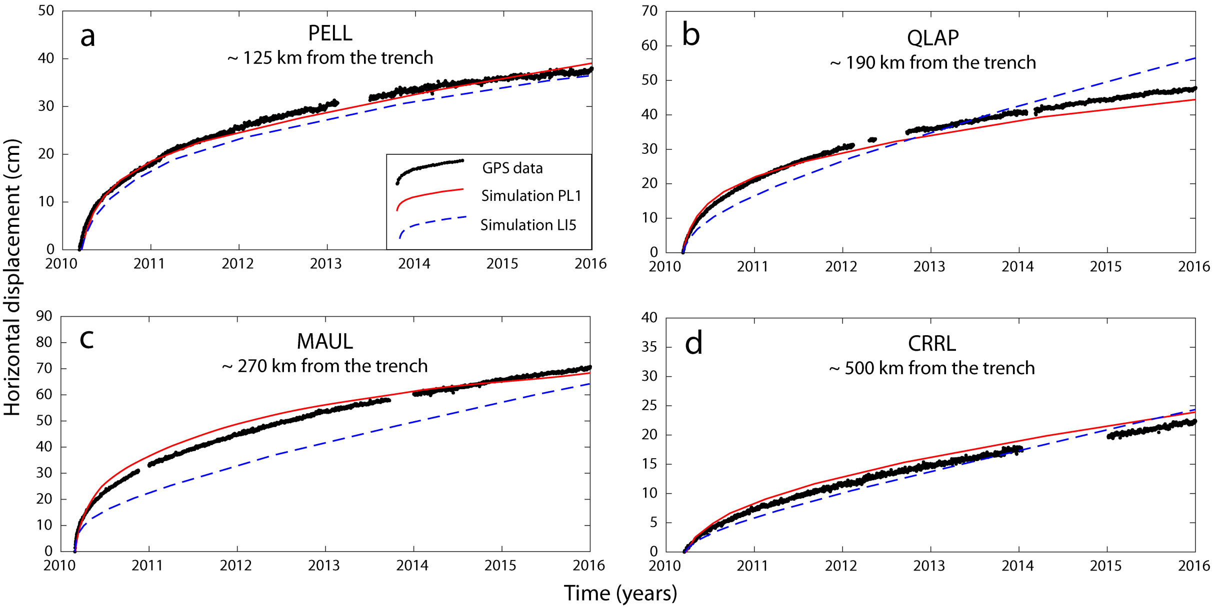

Fig. 4.5 Observed versus modelled time-series (daily solutions) of the horizontal surface displacements over six years after the main shock for cGPS stations PELL, QLAP, MAUL and CRRL. The effect of aftershocks, seasonal and interseismic loading (secular) are removed from the cGPS time-series observations. To account for the temporal decay of the modelled afterslip, we applied a decay law for the afterslip with the shape of the aftershock seismicity decay.

located at ∼ 15–30 km and ∼ 45–60 km depth. Nevertheless, the upper band from simulation LI5 is shallower (∼20 km depth) and contains less afterslip compared to the same band from power-law rheology simulations (∼30 km depth). These bands lie in zones of good resolution (Fig. A.7), and can also be recovered from synthetic checkerboard tests (Fig. A.8), further suggesting their plausibility. Furthermore, our tests show that the main pattern from these bands is apparent between a range of smoothing constants (Fig. A.9). A deeper band at ∼75–90 km depth is also exhibited more clearly in simulations PL3, PL4 and LI5. Despite these zones being at a lower resolution compared to the upper ones, they can still be well recovered as shown by our checkerboard test (Fig. A.8a, b).

The main differences in afterslip distributions are found at greater depths between 60–90 km with two afterslip regions landward of the area of maximum coseismic slip at 34.5–36°S and 37–38°S (Figs. 4.6 and 4.7). In the north region, simulation LI5 shows the largest afterslip distribution which is localized in a region with up to 2.8m between 70–90 km depths (Fig. 4.6e). For the same region, simulations PL3 and PL4 show afterslip up to 0.6 m and 0.8 m of magnitude (Fig. 4.6c, d) at ∼80 km depth, respectively. Simulation PL4 concentrates the highest afterslip of the power-law simulations at this depth (Fig. 4.6d). For the south region, the same simulations PL3 and PL4 show up to 0.9 m and 1.2 m at ∼80 km depth, respectively, and even deeper afterslip is shown from simulation LI5 which reaches up to 1.4 m at approximately 90km depth (Fig. 4.6e).

In contrast, by analyzing the result at the same depths, the afterslip distributions from simulations PL1 and PL2 are reduced in magnitude (Fig. 4.6a, b). There is no deep afterslip for simulation PL1 in the north region (Fig. 4.6a), while simulation PL2 indicates up to 0.4 m (Fig. 4.6b). In the south region, the afterslip is reduced up to 0.5m and 0.8m for simulations PL1 and PL2, respectively.

To better visualize the differences of the afterslip inversion results, we show the differences relative to simulation PL1 as it achieves the smallest MAE (Fig. 4.7). The difference is increasing from power-law rheology simulations PL2–PL4 (Fig. 4.7a, c) reaching up to approximately 0.5 m and 1 m of afterslip in two bands along strike between 20–40 km and 60–90 km depth, respectively; the afterslip distribution difference between PL1 and LI5 is even larger showing differences not only in magnitude, but location as well. In particular, Fig. 4.7d shows that the shallower band of simulation LI5 decreases by approximately 1.5 m and increases in the vicinity of the trench by approximately 0.3 m between 10–20 km depth while in the deeper band, the afterslip distribution has a more pronounce amplitude that exceeds 2 m at 80 km depth.

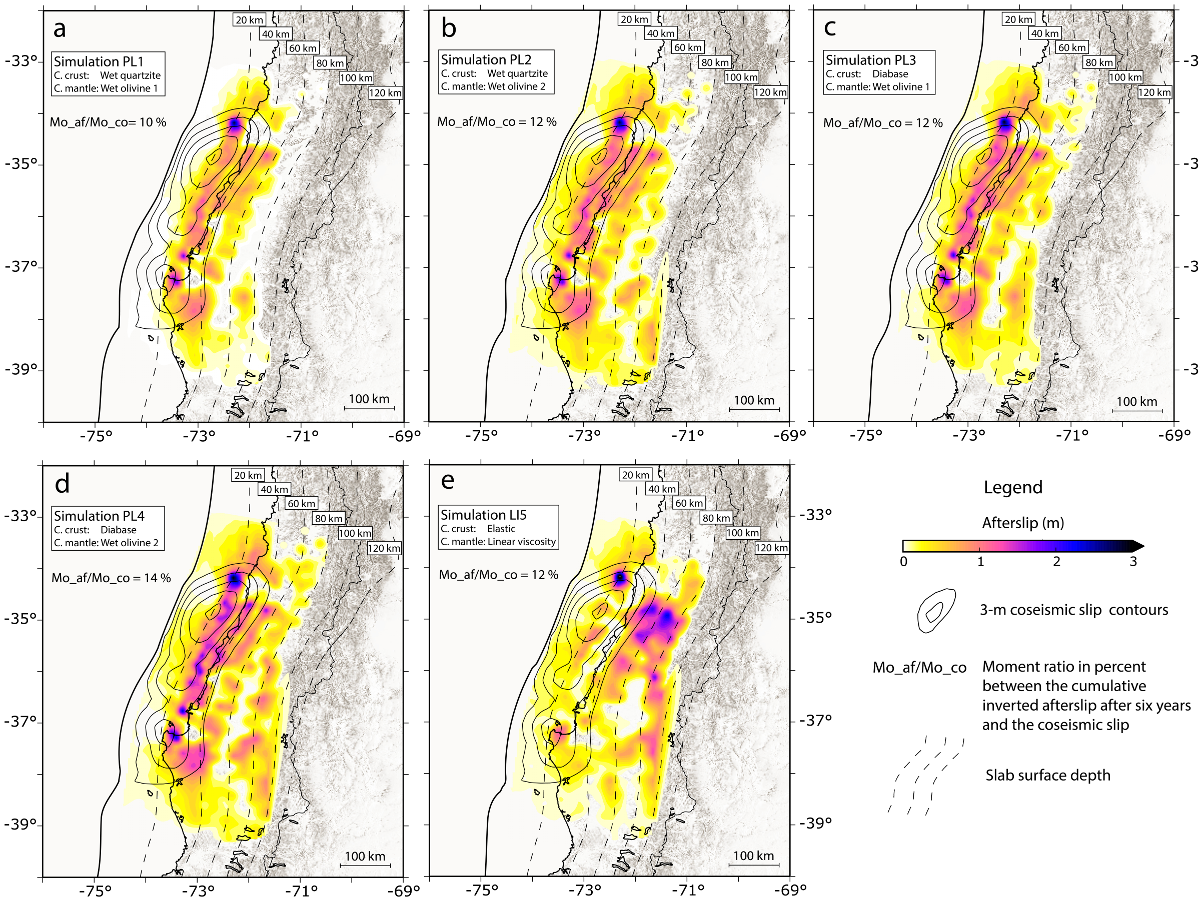

Fig. 4.6 Modelled cumulative afterslip distribution and residual displacement after six years. Ratio of afterslip moment release to coseismic moment release in percent (Mo_af / Mo_co) associated to each simulation are also shown.

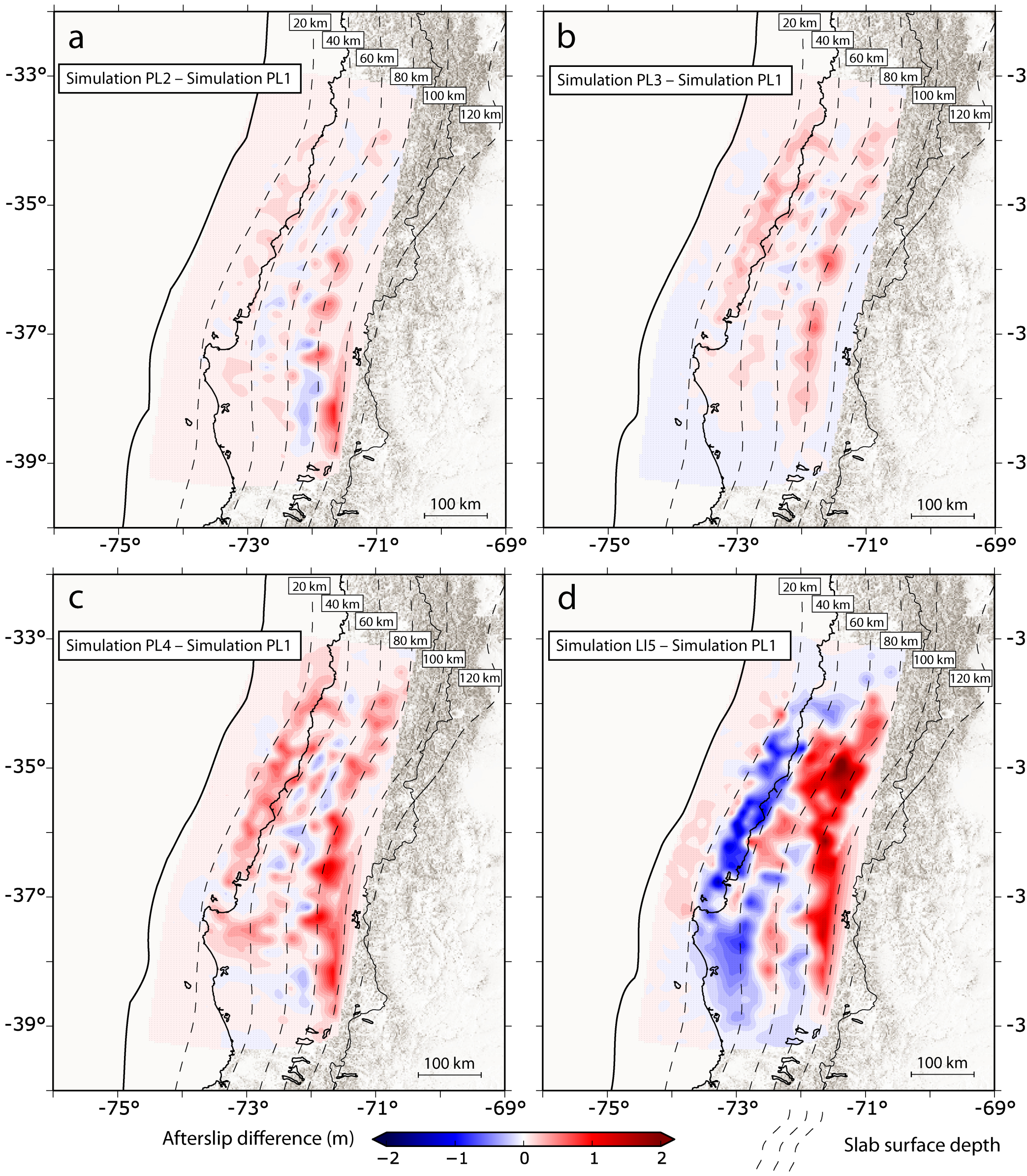

Fig. 4.7 Difference of afterslip distribution with respect to the results of the preferred simulation PL1. Note that the largest differences are found in the linear rheology simulation LI5.

4.4 Discussion

4.4.1 Discriminating afterslip distributions

Our best-fit result with the lowest MAE is simulation PL1 (Fig. 4.4a). However, the MAE of PL3 and LI5 is only 0.6 cm and 0.9 cm, respectively, larger; which is within the uncertainty of the data (7.5 cm). Therefore, we also use the spatial distribution and cumulative moment release from the aftershocks to test if one of these simulations fit better. According to Avouac (2015) and Perfettini and Avouac (2007), afterslip and aftershocks should spatially and temporally correlate. This has been shown by the good correlation between aftershock seismicity and afterslip in studies of Agurto-Detzel et al. (2019), Lange et al. (2014), Perfettini and Avouac (2007) and

Tassara et al. (2016) as well as by a study of Kato (2007) who shows that the aftershock triggering can be explained by afterslip. In addition, a mechanical afterslip-aftershock coupling may be also inferred from their temporal evolutions as both relaxation processes show almost the same decay law over time (Agurto-Detzel et al., 2019; Bedford et al., 2016; Hsu et al., 2006; Lange et al., 2014; Perfettini and Avouac, 2007).

In Fig. 4.8 we compare the resulting afterslip from models PL1, PL3 and LI5 with the location and accumulated moment release of the aftershocks. For the Maule case, most of the aftershock activity occurs in two belts: 1) abroad band equivalent to the megathrust failure during the Maule event, with most of aftershock activity outside of the maximum coseismic slip regions, but in regions of moderate coseismic slip (Agurto et al., 2012; Lange et al., 2012; Rietbrock et al., 2012), and 2) aslightly deeper one at approximately 50 km depth separated by a gap from the coseismic rupture domain. Strikingly, our afterslip inversions from power-law rheology simulations show a good spatial correlation with these aftershock belts, but less so in the linear rheology case (Fig. 4.8). These patterns are also reproduced to some extent by previous models. For example, the afterslip model of Lin et al. (2013) is sandwiched in between the upper and deeper aftershock belts. On the other hand, the afterslip model of Bedford et al. (2013) showed a better correlation with these aftershock belts, but not for the deeper segment (> 60 km). Similarly to a fully elastic crust, simulation PL3 that considers a strong material in the continental crust as diabase and simulation LI5 that considers a fully elastic continental crust result in deep afterslip, in contrast to the location of aftershock activity and its cumulative moment release (Fig. 4.8b, c). Conversely, simulation PL1 shows viscous deformation in the continental crust. It mostly occurs in its lower part at 25–45 km depth and beneath the volcanic arc at 220–450 km from the trench due to the implementation of weaker rock material (wet quartzite), which in turn compensates the deep afterslip (Fig. 4.8a). It is noteworthy to point out that location of viscous deformation, apart from depending on dislocation creep parameters, strongly depends on rheology choice. The linear rheology simulation LI5 mostly concentrates the viscous deformation in the fore-arc continental mantle, while in the power-law rheology simulation PL3 it mostly occurs in the continental mantle beneath the volcanic arc. This difference may explain the larger afterslip at still 80–90 km depth from simulation LI5 as it tries to compensate the lack of deformation beneath the volcanic arc to explain the observed uplift.

Simulation PL1 has a better correlation with moment release from aftershock seismicity. It also results in a better agreement with frictional properties on the fault interface for the area associated to the postseismic deformation of the 2010 Maule event obtained from apparent locking degree from interseismic GPS velocities (Moreno et al., 2010), which is close to zero at > 60 km depth, and with the depth-varying fault segmentation study from seismic wave radiation and seismicity of Lay et al. (2012). Therefore, we consider simulation PL1 as our preferred solution.

The assumption of a relatively weak lower crust is also supported by Farías et al. (2010) who suggested a low-viscosity ductile rather than a strong continental lower crust beneath the volcanic arc at 33.65°S based on seismicity and surface geology, in agreement to the location of the crustal weakening found in this study. This low-viscosity region may be controlled by partial melting as it has been shown from laboratory experiments that crustal rock strength could dramatically drop under melting conditions (Rosenberg and Handy, 2005). Rosenberg and Handy (2005) showed that a plausible melting of 12% for continental crustal rocks could drastically reduce the strength in amphibolite samples from $\sim$1000 MPa to $\sim$300 MPa (see Fig. 2 in Rosenberg and Handy, 2005). For the area associated to the postseismic deformation of the 2010 Maule event, previous studies from tomography images (González-Vidal et al., 2018) and magnetotelluric observations (Cordell et al., 2019) have illuminated potential melting regions, which are in good agreement with the location of the resulting viscous deformation in the continental lower crust.

Using similar data, but a different approach by also inverting for volumes of viscous strain in the continental lower crust and upper mantle, Weiss et al. (2019) found viscous deformation directly beneath the volcanic arc in the continental lower crust and mantle as well. However, our resulting cumulative maximum creep strain in six years in the continental lower crust is broader and it reaches a maximum of $\sim 4 \times 10^{-5}$, which is approximately four times larger than the one from them. Furthermore, they also find a region with a creep strain of $\sim 8 \times 10^{-6}$ in the lithospheric mantle just beneath the Moho discontinuity between $\sim$45–60 km depth, where we find smaller creep strain ($< 2 \times 10^{-6}$). Nevertheless, at deeper regions in the upper mantle, our results agree better. Their creep strain region at 45–60 km depth compensates their smaller and more localized deformation in the continental lower crust compared to our findings, as well as it contributes significantly to the horizontal surface displacement field. These differences may potentially be because of weakening in this region of the upper mantle (45–60 km depth) due to secondary effects such as temperature anomalies or rock material differentiation, which are not included in the forward modelling. Weiss et al. (2019) showed that the ability to infer viscous strain in the continental lower crust and upper mantle is lower because of the decrease of cGPS stations in the volcanic and back arc. Therefore, a denser cGPS network in these regions may be used to assess better the relative contribution of relaxation processes occurring in the continental lower crust and upper mantle to the postseismic deformation field.

Comparing these findings to studies triggered by the postseismic deformation associated to the 2011 Tohoku-oki earthquake, a weak continental lower crust beneath the volcanic arc is also required to explain the postseismic cGPS observations (Hu et al., 2014; Muto et al., 2016). Similarly, the joint inversion of afterslip and lower-crustal viscous strain from space geodetic observations have imaged low transient viscosities in the lower crust beneath the orogenic belt from GPS observations for the 1999 Chi-Chi earthquake (Tang et al., 2019) and the 2016 Kumamoto earthquake beneath active volcanoes from GPS and InSAR observations (Moore et al., 2017), suggesting that transient stress relaxation in the lower crust may be a common and key process following large earthquakes in actively orogenic or volcanic regions.

Our results also show that viscous deformation, due to dislocation creep processes, in the continental upper mantle is a key process during postseismic deformation, supporting previous studies such as Agata et al. (2019), Freed and Bürgmann (2004), and Qiu et al. (2018). Although the mantle rock composition is well known (Hirth and Kohlstedt, 2003), its water content may vary. These variations could be responsible for the small deep afterslip in the south region shown by simulation PL1, as higher water content would produce less deep afterslip, as shown by simulations PL1 and PL3 (0.1 wt.%) compared to simulations PL2 and PL4 (0.005 wt.%), respectively. In this context, this afterslip pattern might compensate the lack of higher water content. The southern region coincides with the Mocha Fracture Zone (MFZ) at the subducting oceanic crust (Contreras-Reyes et al., 2008, and light blue line in Fig. 4.8), suggesting a higher water content in the mantle wedge due to dehydration metamorphic reactions.

The assumption of homogeneous rock properties in the continental crust and upper mantle could also explain the residual displacements as well as secondary features in temperature anomalies in the volcanic and back arcs as pointed out by Peña et al. (2019) for the Maule case. Furthermore, although our test suggests that afterslip and viscoelastic processes can be modelled independently, there may be localized effects. Agata et al. (2019) have recently showed that afterslip-viscoelastic relaxation coupling could locally increase at some inland cGPS stations the surface displacements in $\sim$10% in the horizontal component and $\sim$30% in the vertical using a stress-driven afterslip model, but the total surface displacement field does not substantially change (see Fig. 8 in Agata et al., 2019). On the other hand, the effect of the coupling on afterslip is most important at > 60 km depth (almost zero at < 60 km depth, see Muto et al., 2019), which will not considerably affect our results since most of the afterslip occurs at < 60 km depth in our preferred simulation. However, a future joint non-linear inversion or an afterslip driven model could elucidate secondary features such as temperature anomalies, rock material heterogeneities and afterslip-viscoelastic interaction for the Maule case.

4.4.2 Afterslip models and moment release

As shown in the previous section, the choice of the rheology (linear or power-law) has a strong impact on the afterslip magnitude and pattern, in particular at greater depths (Figs. 4.6 and 4.7). It also has an impact on the location and magnitude of the postseismic viscoelastic relaxation (Fig. 4.8). This deep afterslip pattern for the Maule case was first investigated by Klein et al. (2016) through a deep and weak subduction channel. However, in contrast to their findings, we propose that non-linear viscoelastic relaxation processes in the continental lower crust may result in a surface deformation pattern similar to that expected from a deep subduction channel. Nevertheless, we do not neglect that both processes may operate together as they cannot be separated unambiguously from the observed postseismic surface displacements.

In the shallower segment at < 30 km depth, the afterslip model of Klein et al. (2016) reaches up to $\sim$ 9 m during the first year of postseismic deformation. Similar patterns have recently been shown by Weiss et al. (2019) who found up to 8 m of afterslip at $\sim$10 km depth over the first six years. In contrast, our results suggest that afterslip mostly occurs at 20–60 km depths. These differences might be because Weiss et al. (2019) constrain afterslip to preferentially occur in the regions surrounding the coseismic slip patches. Here, Weiss et al. (2019) considered the slip model of Lin et al. (2013), which results in small slip at < 10 km depth. In contrast, other slip models as the one used in this study Moreno et al. (2012) and Yue et al. (2014) show more slip at

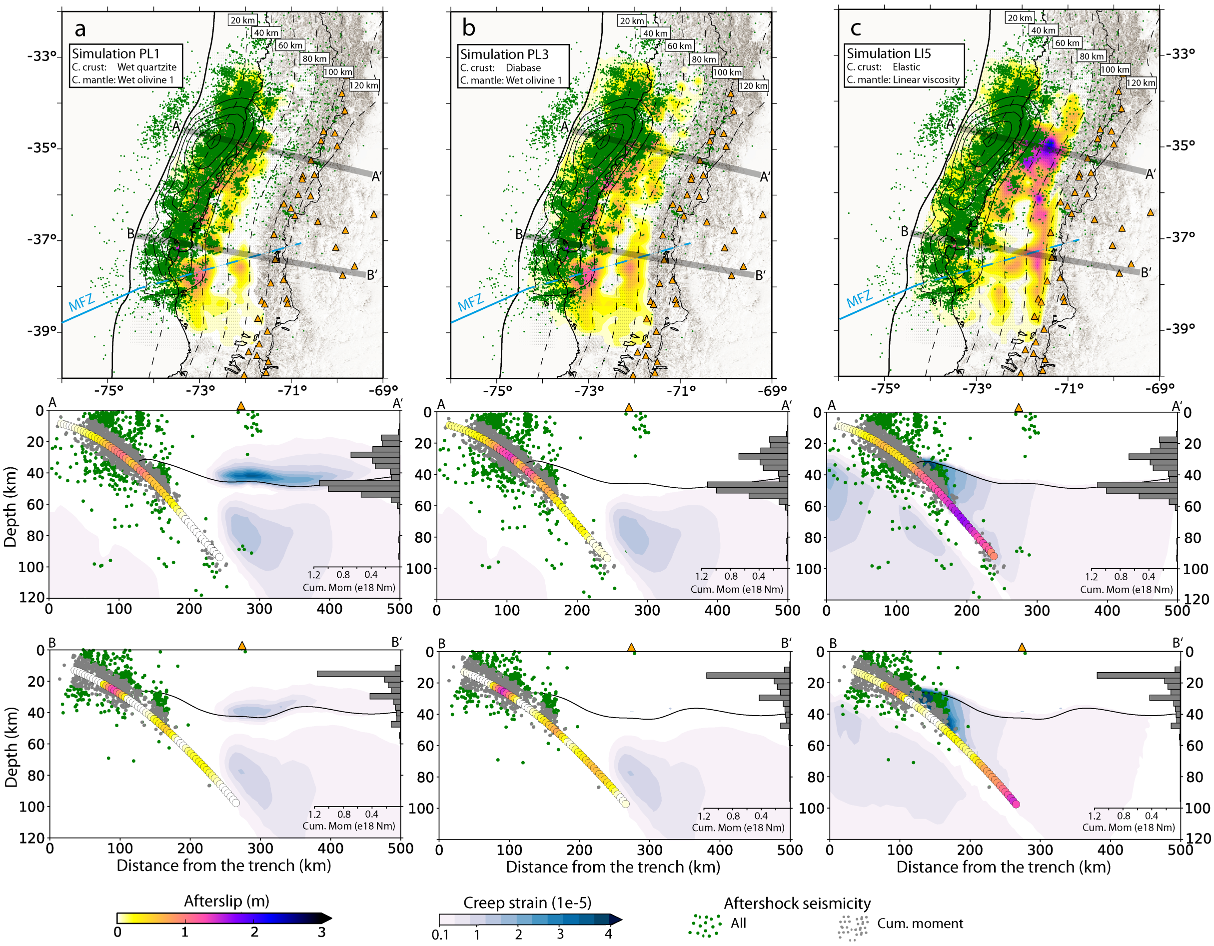

Fig. 4.8 Cumulative afterslip and aftershock seismicity after six years of the Maule event. a), b) and c) on top show the results of the afterslip inversion from simulations PL1, PL3 and LI5, respectively. Middle and lower panels show the cross-sections A–A' and B–B' with 25 km width associated to a), b) and c) with aftershock seismicity, afterslip, second invariant of the creep strain tensor and cumulative moment release of the aftershocks in the grey histograms. Aftershock seismicity is compiled from Lange et al. (2012), Rietbrock et al. (2012) and National Earthquake Information Center (NEIC-USGS). Lange et al. (2012) and Rietbrock et al. (2012) aftershock catalogues cover approximately from March to September in 2010. The periods (first days after the main shock and last 5 years) which are not covered for these catalogues are covered by NEIC. We exclude redundant events from the three catalogues. Histograms are calculated from the grey dots (aftershocks). To account for the uncertainties of the aftershock location, we calculate the cumulative moment release of the aftershocks as proposed by Rietbrock et al. (2012). We first select only aftershocks at ±10 km distance from the interface geometry of the slab, and then we project the selected aftershocks on surface and calculate the cumulative moment release in windows of 10 km width. MFZ corresponds to the Mocha Fault Zone. Coseismic slip in black contours as shown in Fig. 4.6. Solid black line within figures depicts the Moho discontinuity.

shallower regions, but all differ to some extent. These differences are mainly produced because of the fault geometry and data considered during the inversion approach. We have evaluated the impact of slip on our results (Fig. A.10). They show that the location and magnitude of the main afterslip patterns remain almost the same between 20–60 km depth, with small variations at shallower and greater depths. In particular, we cannot precisely assess these differences at shallower regions as they are poorly constrained due to the lack of offshore observations.

Hence, offshore cGPS stations may be used in future as a proxy to better constrain the relative contribution of postseismic relaxation processes to the surface observations and the competing models, since our preferred afterslip model differs mostly from the one of Klein et al. (2016) and Weiss et al. (2019) in the shallower region (< 20 km depth).

At other subduction zones, afterslip inversions show similar deep pattern from models considering only viscoelasticity for upper mantle (Qiu et al., 2018; Tsang et al., 2016; Yamagiwa et al., 2015). This assumption results in an increase of afterslip in the up-dip and reduction in the deeper segments (Qiu et al., 2018; Sun et al., 2014; Tsang et al., 2016). However, these models generally still result in moderate deep afterslip distribution at 80 km depth as the models of Qiu et al. (2018) and Tsang et al. (2016) for the Sumatra-Andaman region by considering a jointly inversion for afterslip and viscoelastic heterogeneities in the asthenosphere above an elastic 100-km-thick lithosphere. The viscoelastic relaxation from these setups occurs in the mantle wedge at 100 km depth and at 250–400 km from the trench. In our preferred simulation most of the viscoelastic relaxation also occurs at such distances from the trench, but conversely, it occurs in a much shallower region, i.e., in the lower crust at approximately 45 km depth (Fig. 4.8a). Since the fact of differences in data source and cover-age, jointly inversion and slab geometry and age, we speculate that such a still deep afterslip may be due to the lack of shallower viscoelastic relaxation.

The moment released by the cumulative afterslip after six years is in our simulations considerably smaller in comparison to fully elastic models. Lin et al. (2013) estimated a moment of 3.6–5.1 $\times$ 10^{21} Nm in 1.3 years following the 2010 Maule earthquake, which is 20-30% of the seismic moment from the main shock. Similar results were reported in other subduction zones after megathrust earthquakes using fully elastic models (e.g., Hsu et al., 2006; Perfettini et al., 2010) and from models that assume a linear viscoelastic mantle rheology as the one from Yamagiwa et al. (2015) who found $\sim$21% of the ratio of afterslip to the coseismic moment release after 2.5 years of postseismic deformation associated to the Tohoku-oki earthquake. In contrast, we estimate a moment release of 1.8 $\times$ 10^{21} Nm in six years from our preferred afterslip distribution which is equivalent to 10% of the coseismic moment (Fig. 4.6a). Thus, in comparison to a power-law rheology simulation that allows viscoelastic relaxation in the continental lower crust, afterslip distribution on the plate interface is larger by a factor of approximately two from models that assume an elastic crust above a mantle with linear viscoelastic rheology. This is mainly explained by the location of the viscoelastic relaxation as a model that allows non-linear viscoelastic relaxation in a shallower region as the continental lower crust reduces the afterslip, in particular and considerably at greater depths.

4.5 Conclusions

We use a 3D forward model with power-law rheology with dislocation creep in the crust and upper mantle and linear viscoelastic rheology to investigate the first six years of postseismic relaxation after the 2010 Maule earthquake. From the residual displacements, we derive afterslip distributions through a standard inversion scheme. Our results show that the largest differences of afterslip distributions are located in the deeper segment of the fault interface at depths > 60 km.

Given that the Mean Absolute Error (MAE) between the cumulative observed and modelled displacements of PL1, PL3 and LI5 is close to each other, we use the assumed correlation between afterslip and moment release from aftershock seismicity to further assess the model results. We find that our preferred simulation PL1 with the lowest MAE also correlates better to the accumulated aftershock moment release.

In comparison to the model with linear rheology, simulation PL1 shows especially in the first years of postseismic deformation a significantly better fit of the observed transient relaxation signal at the cGPS stations. The viscoelastic relaxation from our preferred simulation PL1 mainly occurs in the continental lower crust and to lesser extent in the upper mantle, both beneath the volcanic arc due to dislocation creep processes. In contrast, in the simulation with linear rheology, relaxation mainly occurs in the continental upper mantle beneath the fore arc. In particular, the non-linear viscoelastic relaxation in the continental lower crust trades off the deep afterslip and may be associated with partial melting. Therefore, our results suggest that the continental lower crust is weak rather than strong. We conclude that non-linear viscoelastic relaxation processes in the continental lower crust along with cumulative moment release by aftershocks might potentially better constrain afterslip inversions following megathrust earthquakes, particularly its maximum depth.

Chapter 5

Transient deformation and stress patterns induced by the 2010 Maule earthquake in the Illapel segment

Abstract

Evaluating the transfer of stresses from megathrust earthquakes to adjacent segments is fundamental to assess seismic hazard. In this study, we use a 3D geomechanical-numerical model and GPS observations to investigate the transient deformation and stresses induced by the 2010 M_w 8.8 Maule earthquake in its northern segment, where the M_w 8.3 Illapel earthquake occurred in 2015. The 3D model considers the elastic (instantaneous) response due to the coseismic deformation, and time-dependent afterslip and viscoelastic relaxation processes over the postseismic period. The impact of linear and power-law rheology on the resulting deformation and stresses is also investigated. Furthermore, we evaluate the transfer of stresses under the Coulomb Failure Stress (CFS) theory. Our results reveal that CFS changes prevail during the coseismic period. At the Illapel hypocenter, CFS increased by $\sim$0.05 bar due to the coseismic deformation, while divergent values are obtained in the postseismic period from the choice of rheology. The power-law rheology case produces positive CFS changes in the order of 0.007 bar, and the one with linear rheology -0.004 bar. This deviation is produced because of the resulting postseismic displacements between the choice of rheology model. Here, the surface landward patterns simulated by the power-law rheology case agree better with the GPS data, while opposite patterns are found from the linear case. Additionally, we show that seismicity M_w $\geq$ 5 in the southern region occur in regions of CFS changes $\geq$ 0.2 bar.

5.1 Introduction

Megathrust earthquakes induced local and continental scale deformation (e.g., Hu et al., 2004; Moreno et al., 2012; Vigny et al., 2011), which may last several decades (e.g., Klotz et al., 2006; Wang et al., 2012). In the following years, the crust continues moving over years exhibiting different patterns as observed by GPS measurements (Klein et al., 2016; Loveless and Meade, 2016; Tomita et al., 2015). Inland GPS observations show that in front of the rupture area the crust moves in the sense of the main shock, which in most subduction zones represents trenchward movement. At neighboring segments of the rupture area, however, the GPS horizontal displacements exhibit landward motion (Heki and Mitsui, 2013; Klein et al., 2016; Loveless and Meade, 2016; Melnick et al., 2017; Tomita et al., 2015), as envisioned Anderson in 1975 (Anderson, 1975). While the trenchward motion patterns are mostly attributed to afterslip on the fault interface and viscous relaxation in the lower crust and upper mantle (Hergert and Heidbach, 2006; Hu et al., 2004; Peña et al., 2019, 2020; Wang et al., 2012), the driving mechanisms that control landward patterns following megathrust earthquakes are debatable. For instance, Hu et al. (2016) and Tomita et al. (2015) showed that landward acceleration of the oceanic plate following the 2011 M_w 9.0 Tohoku-oki earthquake in Japan may be attributed to upper mantle viscoelastic relaxation. Alternatively, it has been proposed that the slab pull balance of forces after large earthquakes is the driving mechanism (Heki and Mitsui, 2013; Yuzariyadi and Heki, 2020).

The deformation produced by such patterns will also modify the state of stress at adjacent segments, which may be critically stressed. These segments are key target to be investigated as the stresses transferred by the coseismic and postseismic deformation to mature segments may trigger megathrust earthquakes as witnessed in the Sumatran-Andaman region, Indonesia (Hughes et al., 2010; McCloskey et al., 2005; Pollitz et al., 2006a; Qiu and Chan, 2019), as well as large-magnitude earthquakes in strike-slip settings such as the 1999 Hector Mine earthquake in Southern California, USA, (Freed and Lin, 2001) and the 2016 Visso earthquake in Italy (Tung and Masterlark, 2018).

On the 27th of February 2010, the Maule earthquake occurred in the Central Chile with magnitude $\mathrm{M_w}$ of 8.8, breaking about 500 km length along strike (Fig. 5.1) (e.g., Moreno et al., 2012; Vigny et al., 2011). In its northern segment, ca. 200 km the Maule rupture area, the $\mathrm{M_w}$ 8.3 Illapel earthquake struck on the 16th of September 2015 (Fig. 5.1). The Illapel segment (enclosed area in Fig. 5.2) is a prominent case of study since landward velocity enhancement is observed following the 2010 Maule event (Klein et al., 2016; Melnick et al., 2017; Ruiz et al., 2016), as well as it was a mature segment with the last large-earthquake in 1943 with magnitude of 7.9 (Ruiz and Madariaga, 2018, and references therein). There, GPS data revealed a rise up to 15% in the annual GPS interseismic velocity between the 2010 event and the end of 2014 (Ruiz et al., 2016), but they did not directly measure the locking degree nor stress changes due to this augmentation. On the other hand, Melnick et al. (2017) found an increase of 20% in the apparent locking degree by using GPS observations in the period within 2010 Maule and the 2015 Illapel events. In their study, however, the effect of exponential transient components, e.g., viscous relaxation, were not included as they only considered the change in the linear trend component of the observations between the 2010 and 2015 events to calculate the locking changes. Furthermore, Melnick et al. (2017) did not attempt to explain the observed landward displacement patterns. By contrast, Klein et al. (2016) showed that a possible mechanism to explain such a pattern may be viscoelastic relaxation in the asthenosphere, as well as in a deep, low-viscosity channel along the fault interface. Despite these advances in understanding the kinematics of these patterns, it remains unclear, in particular, how much stress was built-up on the fault interface in the Illapel segment due to the coseismic and postseismic deformation associated to the 2010 Maule event.

Here, we use the 3D geomechanical-numerical model of Peña et al. (2020) and cumulative GPS observations between the 2010 Maule and 2015 Illapel earthquakes to study the induced transient deformation and stress changes in the Illapel segment due to the 2010 Maule earthquake. Our main goal is to quantity the stresses transferred under the Coulomb Failure Stress (CFS) theory due to the coseismic and postseismic deformation in northern segment of the Maule rupture zone. Additionally, our results reveal that landward motion following the 2010 Maule event is very sensitive to the choice of rheology (linear or power-law) incorporated in the 3D model. Our results show that most of the CFS changes are produced by the coseismic deformation and opposite values are produced from the choice of rheology during the postseismic deformation. Additionally, we find an increase in the CFS changes in the order of 1 bar to 0.001 bar from the closest region to the 2010 Maule rupture area to its northernmost region, respectively. These values are discussed in the context of the seismicity between the 2010 and 2015 events.

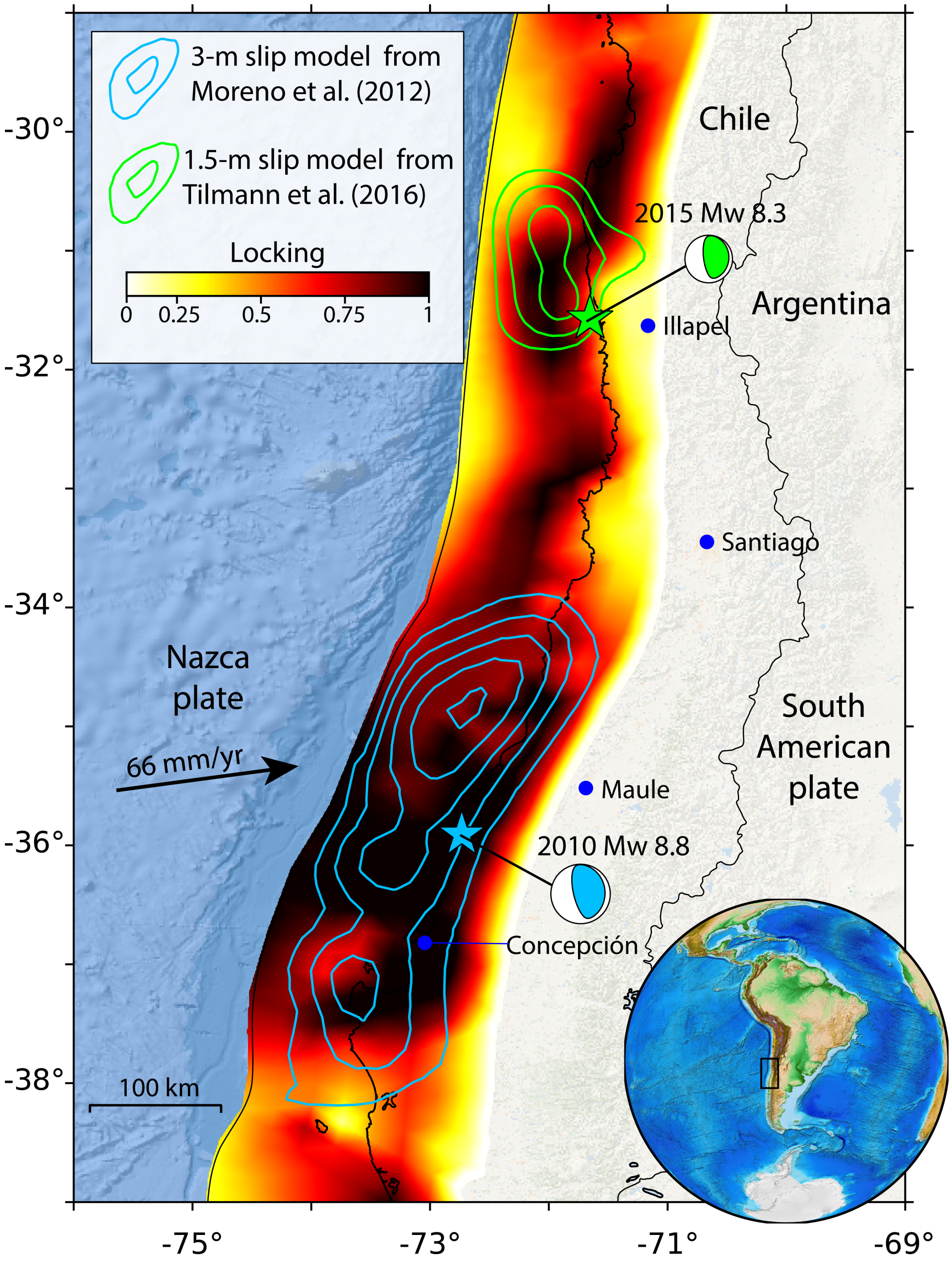

Fig. 5.1 Study area with slip models for the Maule (Moreno et al., 2012) and Illapel (Tilmann et al., 2016) earthquakes, interseismic locking prior to the 2010 Maule events from (Tilmann et al., 2016) and main cities.

5.2 Model setup and GPS observations

We use the 3D geomechanical-numerical model of Peña et al. (2020) to investigate both the deformation and stresses transient patterns induced in the Illapel segment due to the 2010 Maule event. The model described in Peña et al. (2020) considers the slab and Moho geometries obtained from Hayes et al. (2012) and Tassara et al. (2006), respectively. The model extends 4000 km in WE direction, 2000 km in NS direction and 400 km in the vertical (Fig. A.1). The postseismic deformation following the 2010 Maule event is simulated by combining afterslip and viscous relaxation jointly through a forward approach. To do so, we employ the best-fit simulation of Peña et al. (2020) which considers afterslip on the fault interface and power-law rheology with dislocation creep processes in the crust and upper mantle (see parameters in Table 4.2). In this simulation, most of the afterslip occurs at depths < 60 km and viscous relaxation in the continental lower crust and upper mantle beneath the volcanic arc. As discussed by Peña et al. (2020), this configuration matches best the cumulative GPS observations, GPS time-series, as well as afterslip-aftershocks correlation found by previous studies (e.g., Lange et al., 2014; Perfettini et al., 2018). For comparison, we also consider a simulation with linear elastic properties in the crust and linear viscosity in the upper mantle along with its resulting afterslip to evaluate primary difference in the surface displacement field between them. The resulting afterslip from both simulations are shown in Fig. 5.2.

We further compute the Coulomb Failure Stress (CFS) changes on the fault interface in the Illapel segment from the coseismic and postseismic deformation simulations due to the 2010 main shock. We calculate the CFS changes from the relationship between shear and normal stresses given by:

$$\Delta CFS = \Delta\tau - \mu'\Delta\sigma \tag{5.1}$$

where ΔCFS is the CFS change, $\Delta\tau$ is the change in shear stresses, μ' the effective coefficient of friction and $\Delta\sigma$ the change in normal stresses (King et al., 1994; Stein, 1999). Following the approach of Moreno et al. (2018), in this work we consider a heterogeneous effective coefficient of friction on the fault interface. They showed that a higher friction coefficient in regions of locking ≥ 0.8 than its surroundings explained the occurrence of moderate-size earthquakes in southern Chile better. For comparison, we also consider the case of higher friction in regions of locking ≥ 0.5 and 0.2. Moreno et al. (2018) found an optimal value of 0.3 between the ration of the smaller to the higher friction coefficients with values of approximately 0.04 and 0.01, thus we use the same values. These small values are also supported by a recent study investigating Mountain building worldwide (Dielforder et al., 2020) and by stress orientations inversion of moment tensors subduction earthquakes since they suggest frictional zonation with higher apparent friction coefficient in highly locked than creeping regions (Hardebeck and Loveless, 2018)). We tested higher values as well, although they do not play a major role in our results, which agrees to Pollitz et al. (2006a) who found similar stress changes by considering a range of friction coefficients between 0 and 0.8 to investigate the stress changes in the Sumatra-Andaman region. The resulting numerical problem is resolved with the AbaqusTM software, version 6.14, and CFS changes are computed using GeoStress Add-on (Stromeyer et al., 2020) for Tecplot 360 EX, version 2019 R1.

To investigate general differences between the results deformation in the Illapel segment between the choice of rheology, we also consider the cumulative GPS observations from Melnick et al. (2017) between the 2010 Maule and 2015 Illapel earthquakes. In this data set, the effect of aftershocks and seasonal components are removed (further information can be found in supporting information in Melnick et al., 2017). Following the approach of Melnick et al. (2017) and Klein et al. (2016), we have also removed the interseismic component measured prior the 2010 Maule earthquake to account only for the postseismic effects following the 2010 Maule event. Notice that the resulting cumulative GPS displacements slightly differs from Melnick et al. (2017) as they only used the linear component of the GPS displacements in the same period, but our results agree better with Klein et al. (2016) as we use the same approach. The resulting cumulative GPS displacements are displayed in Fig. 5.2.

5.3 Results

In this section, we present the results by using the previously described 3D forward model considering jointly viscoelastic-afterslip processes (Fig. 5.2). We also calculate the cumulative CFS changes and compare it with the seismicity between the 2010 Maule and 2015 Illapel earthquakes in Fig. 5.3 and Fig. 5.4, respectively.

5.3.1 Surface displacement patterns

Fig. 5.2 shows the cumulative GPS displacements between the 2010 Maule and 2015 Illapel earthquakes versus the modelled ones. In the Maule rupture zone, the resulting deformation by combining afterslip and viscoelastic relaxation does not exhibit large differences in the horizontal patterns between a simulation with linear and power-law rheology as both show similar pattern and magnitude (Peña et al., 2020). However, this is not the case for the patterns in the Illapel segment. There, the observations display landward displacements with a strong north component and a maximum cumulative displacement of 3.9 cm. By comparing the GPS observations with our results, the simulation that account for power-law rheology can better explain the observed postseismic patterns than the linear rheology case. The power-law rheology simulation results in landward motion mostly with a strong east component and a similar vector magnitude compared to the observations (Fig. 5.2a). This simulation also shows a maximum displacement at approximately at latitude -30.5°, decreasing to north and south from this latitude, in agreement to the observations. Conversely, the linear rheology case shows trenchward motion with northwest direction and slightly larger magnitude than the observations (Fig. 5.2b). Considering that these GPS observations in the Illapel segment were not included in the postseismic deformation analysis of Peña et al. (2020), our forward model provides a good first-order explanation to the general observed landward patterns and magnitude. Therefore, these results can calculate the stresses transferred to the Illapel segment to assess earthquake triggering as we will present in Fig. 5.3.

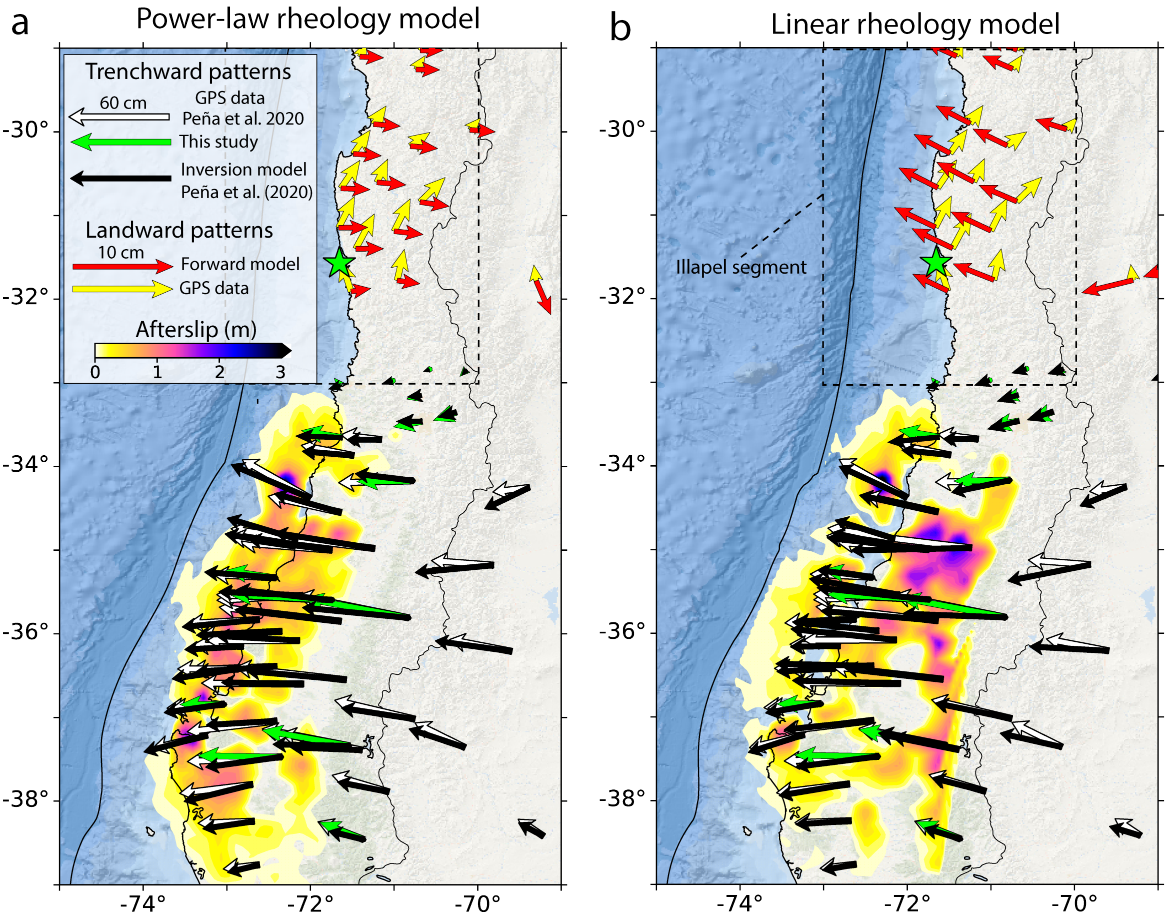

Fig. 5.2 Observations versus modelled displacements and afterslip inversion on the fault interface (projected on surface) from the simulation considering power-law (a) and linear (b) rheology. The Illapel segment is enclosed by the black-dashed rectangle. The GPS observations used in the study of Peña et al. (2020) cover 6 years from the 27 February 2010 (white arrows). In this study, we investigate the period between the 2010 Maule (27 February 2010) and the 2015 Illapel (16 September 2015), which represents 5.5 years. Therefore, the resulting modelled surface displacements displayed in the Illapel segments account for this period, but the differences considering six years are negligible. Thus, green (trenchward) and yellow arrows (landward) represent the cumulative 5.5-years surface displacements from the GPS data, while the red arrows from the model in the same period.

5.3.2 CFS changes

In Fig. 5.3 we present the resulting CFS changes for the coseismic and postseismic periods by considering friction zonation in regions of locking ≥ 0.8, 0.5 and 0.2, which we hereafter will name scenario A, B and C. Although the choice of the friction zonation has an impact in the resulting CFS changes (Fig. 5.3), they have negligible effect on the resulting displacement patterns. We find that the coseismic deformation mostly contributes to the CFS changes transferred to the Illapel segment between the 2010 and 2015 events in all friction zonation scenarios, which accounts approximately 70% of the total shear stresses transferred. Here, the choice of other coseismic slip models does not greatly affect the CFS changes since small deviations are found in the resulting afterslip and viscous relaxation distributions (Fig. A.10 in Chapter 4). We find that the largest CFS changes occur in regions closest to the 2010 Maule rupture region with maximum magnitude close to 0.8 bar, which decreases northwards to values smaller than 0.001 bar. In the Illapel hypocenter, the calculated coseismic CFS changes from the power-law rheology case are 0.05 bar, while in the postseismic period are 0.008 bar for friction zonation in scenario A (higher friction in locking regions ≥ 0.8) as shown in Fig. 5.3a, b. For scenario B, the coseismic and postseismic CFS changes are reduced to 0.05 bar and 0.008 bar, respectively (Fig. 5.3d, e), while the coseismic and postseismic CFS changes are smaller than 0.005 bar for the scenario C (Fig. 5.3g, h). On the contrary, negative CFS changes are found by comparing the postseismic scenarios against the linear rheology case. We find that CFS changes of -0.004, -0.01, and -0.003 bar for scenarios A, B, and C, respectively. Since CFS changes are dependent on the rake vector, i.e., negative in the direction of the fault failure, these negative values are mainly produced because the trenchward displacement patterns from the linear rheology case (Fig. 5.3b).

5.4 Discussion

Landward deformation patterns following megathrust earthquakes have been recently observed by modern GPS data (e.g., Heki and Mitsui, 2013; Melnick et al., 2017), but their mechanism is not fully understood. Our results reveal that to achieve this pattern, the choice of rheology is critical. Here, an upper mantle with homogenous and linear viscoelastic material properties cannot achieve such a pattern. In contrast, second-order rheologies for the crust and upper mantle may better explain this pattern as shown by Klein et al. (2016) by considering a layered upper Earth with Burgers rheology or temperature-dependent power-law rheology with dislocation creep processes as shown in this study. On the other hand, Heki and Mitsui (2013) hypothesized that deep slab acceleration may also play a key role. This may produce broad deformation patterns challenging to distinguish from the current GPS observations, we cannot thus rule out its contribution in landward deformation enhancement, as well as the interplay between these processes. However, our study emphasizes the use of power-law rheology to investigate such a pattern as well.

Although our forward simulation cannot perfectly explain the north component, the magnitude of cumulative landward displacement pattern is well achieved by our power-law rheology simulation and we can thus infer first-order stresses induced in the Illapel segment. Furthermore, we compare the total CFS changes against seismicity Mw ≥ 5 in the Illapel segment to explore the earthquake triggering due the coseismic and postseismic deformation (Fig. 5.4). Interestingly, the seismicity is mostly located in the surroundings of highly locked regions as shown in Fig. 5.4a between the 2010 and 2015 events, which agrees better with the magnitude of CFS changes calculated at each hypocenter in scenario A, i.e., higher friction in regions of locking ≥ 0.8 (Fig.

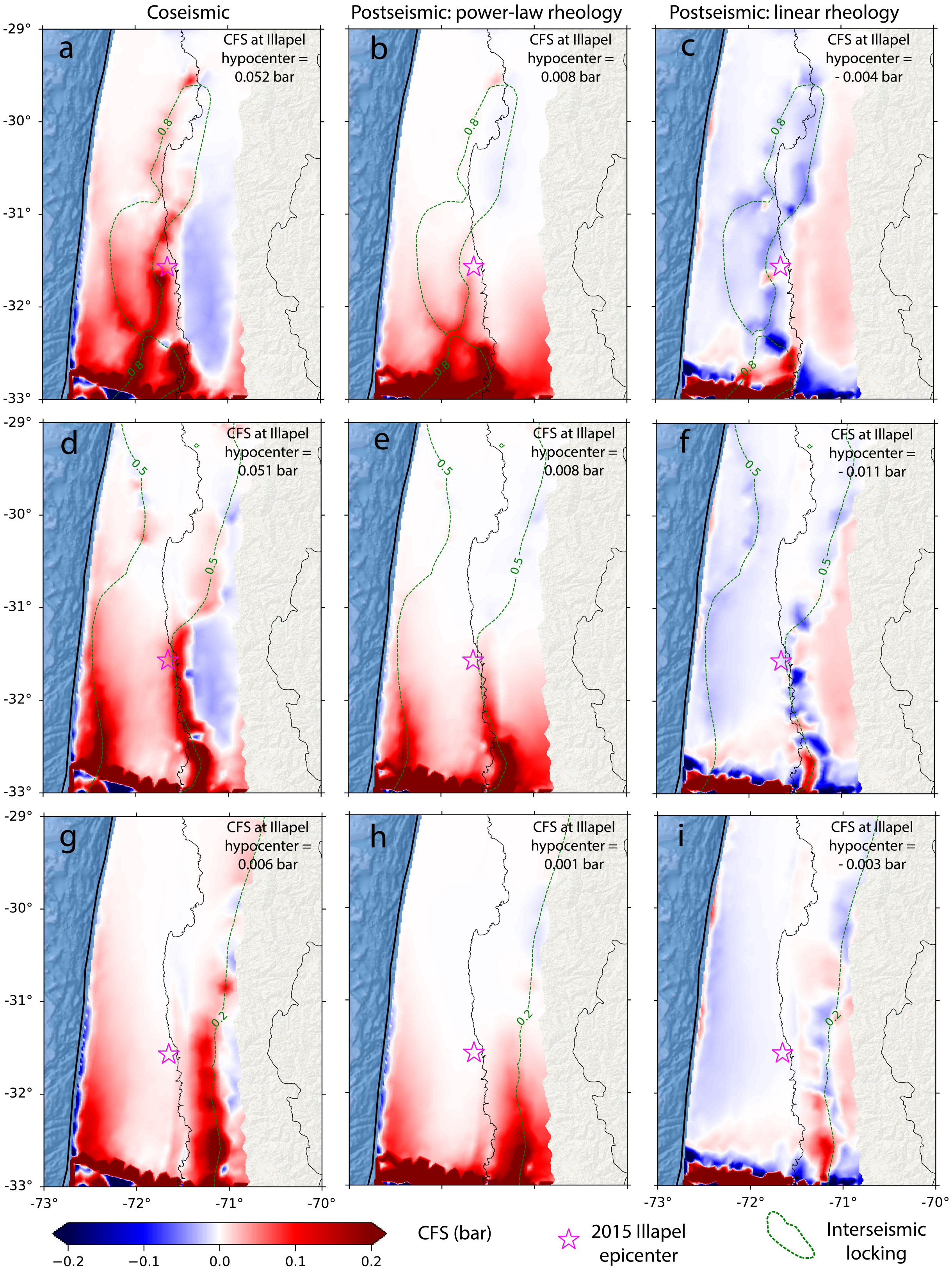

Fig. 5.3 Coulomb Failure Stress (CFS) changes from the simulated coseismic (left panel) and postseismic deformation with power-law (middle) and linear rheology (right) in the Illapel segment (black-dashed rectangle Fig. 5.2). Panels on the left, middle and right consider higher friction in locking regions ≥ 0.8 (a, b, and c), ≥ 0.5 (d, e, and e), and ≥ 0.2 (g, h, and i) than its surroundings, respectively.

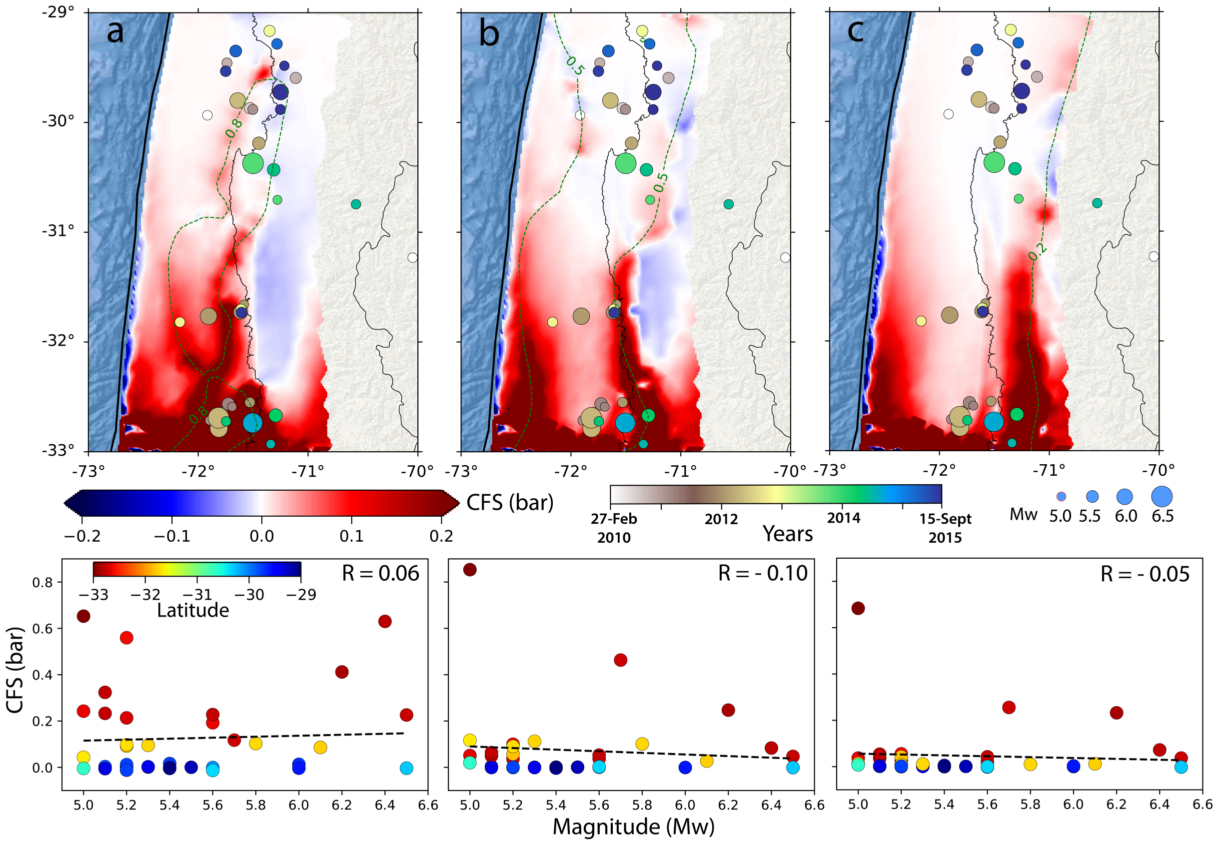

Fig. 5.4 Total CFS (coseismic plus postseismic) changes extracted from the power-law rheology simulation and seismicity Mw ≥ 5.0 in the Illapel segment between the 2010 and 2015 events associated for scenarios A (a), B (b), and C (c). Upper panel exhibit the sum of the CFS as shown in Fig. 3 a-b, d-e, and g-h. Lower panel exhibits the total CFS calculated at each seismicity hypocenter versus seismicity magnitude, while R corresponds to the Pearson correlation coefficient.

5.4a). In particular, all seismicity (twelve events) in latitudes between 32°S and 33°S matches CFS changes ≥ 0.2 bar, while three events in scenarios B and C. Additionally, the calculated CFS changes at Mw ≥ 6.0 hypocenter are on average ca. 0.1 bar higher in scenario A than in B and C, which changes the Pearson correlation coefficient to positive compared to the same scenarios (Fig. 5.4a). Similarly, larger CFS changes in scenario A compared to B and C are also found at other latitudes (lower panel in Fig. 5.4). These small values are sufficient to trigger seismicity as statically proven in many subduction and strike-system settings (King et al., 1994; Ziv and Rubin, 2000), as well as shown by rate-and-state friction laws (Lowry, 2006; Stein, 1999). Yet, no strong increase in seismicity have been reported from the current catalogues after the 2010 event in Illapel segment (Ruiz et al., 2016) for seismicity M_W 4.5, remaining intriguingly changes in lower seismicity, which may provide key information to evaluate seismicity triggering better (Toda et al., 2011a,b). However, a tendency in the augmentation of seismicity at latitudes close to 32.7°S after the 2010 Maule event compared to its previous year is shown from Heidarzadeh et al. (2016) by using the USGS–NEIC catalogue. Furthermore, an offshore M_W 5.2 offshore Coquimbo (latitude ca. 31.7°S) occurred only 30 minutes after the 2010 main shock, where the CFS changes at the hypocenter increased by 0.07 bar. Hence, we suggest that seismicity in the southern region of the Illapel segment was mostly triggered by the coseismic deformation of the Maule event.

Furthermore, four Mw ≥ 6 also occurred in the southern region of the Illapel segment. Two of them occurred in the beginning of 2012, by the time afterslip and viscous relaxation mostly takes place (Peña et al., 2020; Weiss et al., 2019) and CFS increase by 0.08 bar due to the co- and postseismic deformation, and thus likely triggering these events. However, in this segment and also further north, including the Illapel main shock hypocenter, the remaining events occurred from the end of 2013 (Fig. 5.4). Therefore, what controls their occurrence remains poorly understood. Additional and more efficient transfer of stresses mechanism may be related to dynamic triggering and specially pore-fluid processes. The first one may change the state of the stresses of the medium due to the passage of the seismic waves both at near and remote distances, but is a very short-term mechanism (Freed, 2005; Van Der Elst and Brodsky, 2010). On the other hand, pore-fluid processes may last longer, where their resulting surface deformation is confined close to the rupture zone rather than further distances (Hu et al., 2014; Hughes et al., 2010; Masterlark, 2003). Moreover, it is generally smaller than that from viscous relaxation, although the resulting stresses changes are comparatively larger than those from viscous relaxation (Hughes et al., 2010; Masterlark et al., 2001). Hence, the transfer of stresses during the postseismic deformation to the Illapel segment may be underestimated by not considering pore-pressure processes.

5.5 Conclusion

We investigate the deformation and stress patterns induced in the Illapel segment by the 2010 Maule earthquake. By doing so, use a 3D model that accounts for coseismic and postseismic of the Maule event, as well as cumulative GPS observations between the 2010 Maule and 2015 Illapel events. Our results show that the achievement of observed surface landward patterns following the 2010 main in the Illapel segment is sensitive to rheology model during the postseismic deformation. Here, power-law rheology can explain both pattern and magnitude of the cumulative displacement vector observed by GPS data, but fails in the north component. On the other hand, a simulation that considers linear viscosity in the upper mantle and an elastic crust exhibits trenchward motion. These patterns have also a great impact in the resulting CFS changes during the postseismic period, however, our results reveal that most of the CFS are produced due to the coseismic deformation. Since the power-law rheology simulations achieves a better fit to the GPS data, we compare the CFS changes from the coseismic and postseismic deformation against the seismicity activity between the Maule and Illapel events. We find that small values (< 0.06 bar) are transferred to the Illapel hypocenter. However, in the southern region of the Illapel segment, the seismicity activity correlates well with CFS changes higher than 0.2 bar, which are sufficient to trigger seismicity as shown by previous studies (King et al., 1994; Stein, 1999). Therefore, our results suggest that they were mechanically triggered by the coseismic and postseismic deformation induced by the Maule event. Our study emphasizes the importance of using power-law rheology models to investigate transient deformation patterns as well as stress changes induced by megathrust earthquakes. In particular, future research should be focused on the transfer of stresses from the 2015 Illapel earthquake to the Atacama segment (north to Illapel), which has not experienced seismic events with $M > 7.5$ since the 1922 M_w 8.5 Atacama earthquake and may be close to failure.

Chapter 6

Summary and discussion

In this dissertation, I present the first comprehensive analysis of the postseismic deformation following the 2010 Maule earthquake in Chile by combining cutting edge geomechanical-numerical models, Global Positioning System (GPS) observations, and aftershock seismicity. Through the three main studies in Chapter 3, 4 and 5, the following is considered in the 2D and 3D models: spontaneous (coseismic) and time-dependent (postseismic) deformation with linear (Maxwell) and temperature-dependent power-law rheologies; and a plausible range of rheological (elastic and creep) parameters. The viscosity in the model with power-law rheology is fully controlled by the dislocation creep parameters and temperature field in the crust and upper mantle. In contrast, the linear rheology case considers a fully elastic crust and an upper mantle with homogeneous, linear viscosity.

I particularly examine, for the first time, the hypothesis that the GPS displacements following the 2010 Maule earthquake can be predicted by geomechanical-numerical models incorporating power-law rheology with dislocation creep processes. Furthermore, I propose a novel approach to constraint postseismic deformation processes.

In this chapter, I summarise the main findings from the core work presented in Chapters 3, 4, and 5, which are in relation to the research questions formulated in Chapter 1. Additionally, I also discuss the implication of my findings in the current state of our thinking on postseismic processes and potential issues that could be tackled with geomechanical-numerical models considering power-law rheology.

6.1 Recap of scientific research questions

Can power-law rheology be used to investigate the postseismic deformation associated to the 2010 Maule event, and what are the principal differences in the resulting postseismic displacements from models considering linear or power-law rheologies?

This question is mainly addressed in Chapters 3 and 4. The study in Chapter 3 is the first study to demonstrate that a 2D model with power-law rheology in the crust and upper mantle can be used to examine the postseismic deformation associated to the 2010 Maule event.

My results showed that the choice of a model with linear or power-law rheology does not show large variations in the cumulative surface displacement in the horizontal component (see Figs. 3.4, 3.5, and 4.4). The deviations between rheologies are in the GPS uncertainty range, and their displacement patterns are similar. The maximum amplitude of the surface horizontal displacements is found in the volcanic arc, at approximately 250 km from the trench, while in the vicinity of the trench, the modelled results show landward motion (Fig. 3.4a). Although opposite horizontal displacement patterns are exhibited in the northern segment of the Maule rupture, these are small compared to the overall surface displacement field. I will further discuss this in the last question.

Quite to the contrary, in the vertical component, the cumulative postseismic displacements reveal fundamental differences from the choice of rheology model. I find opposite patterns from distances from the trench (Fig. 3.4). My findings reveal that the vertical patterns, especially the uplift in the volcanic arc, are clearly better explained by a model with power-law rheology in the crust and upper mantle (Figs. 3.4b and 4.4).

Although the cumulative surface displacements in the horizontal, resulting from linear or power-law rheology models, are similar, when examining the displacements over time, my results exhibit fundamental deviations (Figs. 3.6 and 4.5). My findings show that the high-rate GPS transient displacements are remarkably in better agreement with the modelled time series from the power-law case (Figs. 3.6, 4.5, and A.6). Furthermore, in Chapter 3, my results indicated that temperature variations, close to the temperature uncertainties, can considerably amplify the modelled cumulative amplitude and the displacement rate over time (Fig. 3.8). Therefore, temperature variations may control the mismatch between the resulting surface displacements from the power-law rheology model and the GPS data (Figs. 3.6 and 4.5).

What is the rheology model's role in location, magnitude, and patterns of afterslip and viscous relaxation following megathrust earthquakes, especially when a continental crust with power-law rheology is also considered?

In Chapters 3 and 4, I also present the impact of rheology on afterslip and viscous distributions. In Chapter 3, my results reveal that location, magnitude, and patterns of viscous relaxation strongly depend on rheology choice. The linear rheology case results in viscous relaxation mostly occurring in the mantle wedge, beneath the forearc (Fig. 3.7b). Conversely, the one from power-law rheology, primarily occurs in the continental lower crust, beneath the volcanic arc, in a region extending about 200 km (Fig. 3.7a). These variations are the principal reason for the different patterns in the resulting vertical surface displacement.

In Chapter 4, I extent the 2D model approach into a 3D model approach, and the afterslip distribution is obtained from an inversion of the GPS observations. My results exhibit that afterslip inversions are significantly affected by the choice of rheology model (Fig. 4.6 and 4.7). The election of creep parameters in the continental crust and upper mantle also has a role in the afterslip distribution, but mostly in the amplitude. In contrast, the rheology choice largely affects both the magnitude and location of afterslip, particularly at depths > 60 km. The model with linear (viscosity) rheology shows large afterslip (approximately 2.5 m) at 80 km depths. Conversely, my results reveal that a power-rheology model that results in non-linear viscous relaxation in the continental lower crust, considerably reduces the deep afterslip patterns. This region of viscous relaxation is similar to the one presented in Chapter 3, i.e., beneath the volcanic arc in an area extending from approximately 250 to 450 km from the trench.

Furthermore, my results indicate that the non-linear viscous relaxation primarily occurs in the continental lower crust, with a maximum creep strain of 4×10^{-5} and an effective viscosity close 5×10^{18} Pas after six years. This is in contrast to previous studies for the Maule case and at other subduction zones, as these studies mostly considered a whole elastic crust (e.g., Agata et al., 2019; Qiu et al., 2018; Shi et al., 2020a; Sun and Wang, 2015; Wang et al., 2012). Although the study of Weiss et al. (2019), for the Maule case, also results in non-linear, lower-crustal viscous relaxation, it contributes slightly to the GPS observations. I attribute these variations to differences between their inversion constraints approach and model geometry and my postseismic model approach. Despite these deviations, and more importantly, both postseismic models agree that the continental lower crust acts as a non-linear viscous material, rather than a fully elastic material as commonly considered.

How can additional information from independent observations such as aftershock activity be integrated to assess postseismic models better?

Postseismic models are not unique, and they could eventually explain the displacement field recorded by GPS observations equally well or in the order of the data uncertainty. Therefore, additional information should be incorporated to rule out competing postseismic models.

As presented in Chapter 4, the Mean Absolute Error (MAE) between the surface displacements observed versus the modelled ones is in the order of the data's uncertainty, when considering a model with linear or power-law rheology. However, I find large variations in the resulting afterslip distributions, especially at greater depths (Fig. 4.6). In this dissertation, I use an innovative approach to discriminate postseismic simulations. This approaches combines power-law rheology modelling, GPS data, and the premise that afterslip processes primarily drive aftershocks. In particular, the latter is fundamental to rule out competing postseismic simulations. I calculate the cumulative moment released from the aftershocks closest to the slab interface, and evaluate this against the inverted afterslip distributions (see caption in Fig. 4.8 for further details). In agreement to previous seismological studies (e.g., Lange et al., 2012; Rietbrock et al., 2012), most of the aftershock moment release occurs at depths < 60 km depths, indicating that below these depths, stable sliding and/or plastic processes are dominant.

My results clearly show that the model, whose resulting afterslip distribution achieves best this criterion, is the one that also results in non-linear viscous relaxation in the continental lower crust and, to a lesser extent, in the continental upper mantle (Fig. 4.8a). Quite to the contrary, at greater depths, where the aftershock moment release is relatively small, I find substantial afterslip from the linear rheology case (Fig. 4.8c).

These outcomes also agree with the frictional properties on the fault interface from additional constraints, such as the apparent interseismic locking degree (e.g., Loveless et al., 2009; Moreno et al., 2010) and the depth-segmentation seismological study of Lay et al. (2012). Furthermore, a continental crust that exhibits non-linear viscous relaxation is also in better agreement with the crustal-rock strength under high temperature and stress conditions (e.g., Kirby and Kronenberg, 1987; Rybacki and Dresen, 2000). Consequently, in this dissertation, I propose this novel approach to infer location, magnitude, and patterns of postseismic processes better.

How much stresses are transferred to neighbouring segments due to afterslip and viscous relaxation, and to what extent are they related to postseismic seismicity and ultimately to megathrust earthquakes?

This question is addressed in Chapter 5. This is the first work to examine the transfer of stresses induced by the coseismic and postseismic deformation of to the Maule event, considering a model with afterslip and power-law rheology, in the Illapel segment; where the M_w Illapel earthquake occurred in 2015.

I calculate the stress changes under the Coulomb Failure Stress (CFS) theory by using the preferred simulation, obtained from the cumulative work carried out in Chapters 3 and 4. For comparison, I also calculate the CFS changes from the linear rheology case.

My results reveal that the coseismic deformation produces most of the CFS changes. At the Illapel hypocenter, I find that the CFS increased by $\sim$0.05 bar (0.005 MPa) due to the coseismic deformation, while 0.008 bar and -0.004 bar for the model with power-law and linear rheology, respectively. These differences in the postseismic period are due to the modelled displacement from the rheology choice. In the context of the Chilean subduction zone and the CFS theory, landward displacement patterns will produce positive CFS values, which means that the segment is brought closer to failure (King et al., 1994). The opposite is expected from trenchward displacement patterns, i.e., negative CFS values. The landward patterns recorded by GPS are clearly better explained by the power-law rheology model (Fig. 5.2). Therefore, a postseismic power-law rheology model can also better estimate the CFS changes at neighbouring segments.

Yet, the small CFS values calculated at the Illapel hypocenter suggest that the Illapel earthquake was unlikely triggered directly by the Maule event and its subsequent postseismic deformation. In contrast, I find that in the southern part of the Illapel segment, the CFS augmented by 0.8 bar from the co- and postseismic deformation, which falls within the CFS threshold ($\sim$0.1 bar) to trigger seismicity, as reported by previous studies (e.g., King et al., 1994; Stein, 1999). Since the postseismic deformation prevails in the first two years, as shown in my results in Chapter 4, I conclude that the Maule earthquake triggered the seismicity in the southern region of the segment during this period.

In the same southern region, however, two $M_w \geq 6$ occurred from 2013 and before the Illapel mainshock, but the CFS changes are very small. Additional mechanisms controlling these events may be related to fluid-pressure and/or dynamic wave processes. However, it is challenging to evaluate this hypothesis due to the lack of key seismic and geodetic observations.

6.2 Discussion

6.2.1 Additional constraints on postseismic models

As shown and discussed in this dissertation, the implementation of temperature-dependent power-law rheology at subduction zones, as well as its distinction from linear rheology, has been possible due to the tremendous increase of geophysical observations triggered by the 2010 Maule and 2011 Tohoku-Oki earthquakes. In particular, the GPS time series and the vertical component provide insightful constraints. Although I have not included Burgers rheology in the main Chapters, its implementation in the upper mantle will only improve the fit to the transient GPS signal in the horizontal component, as I demonstrate in Fig. 6.1a, c. Furthermore, Fig. 6.1c exhibits that the predicted surface displacements over six years are challenging to distinguish from Burgers and and power-law rheology models. These findings also agree with Takeuchi and Fialko (2013), who investigated postseismic processes in the Mojave desert, Eastern California. Takeuchi and Fialko (2013) showed that the postseismic surface displacements from a 3D model with Burgers and power-law rheologies might be difficult to distinguish in short-term intervals (< 5 yrs). On the other hand, I show that the resulting surface vertical patterns from Burgers rheology are very similar to the one from the linear rheology case, and cannot thus explain the observed vertical patterns, particularly the fast uplift in the volcanic arc (Fig. 6.1b, d). Consequently, the afterslip distribution from a model with Burgers rheology in the upper mantle will also result in remarkable afterslip at greater depths. An alternative approach to explain this uplift pattern, is through the inclusion of a deep, low-viscosity subduction channel, as proposed by Klein et al. (2016) for the postseismic deformation associated to the Maule event. Given that this approach also can explain the postseismic displacements, it is challenging to discriminate the approach of (Klein et al., 2016) and mine from the current GPS observations.

However, my results reveal fundamental differences after one decade (2020) of the mainshock between the choice of a model with Burgers and power-law rheology (Fig. 6.1e, f). After one

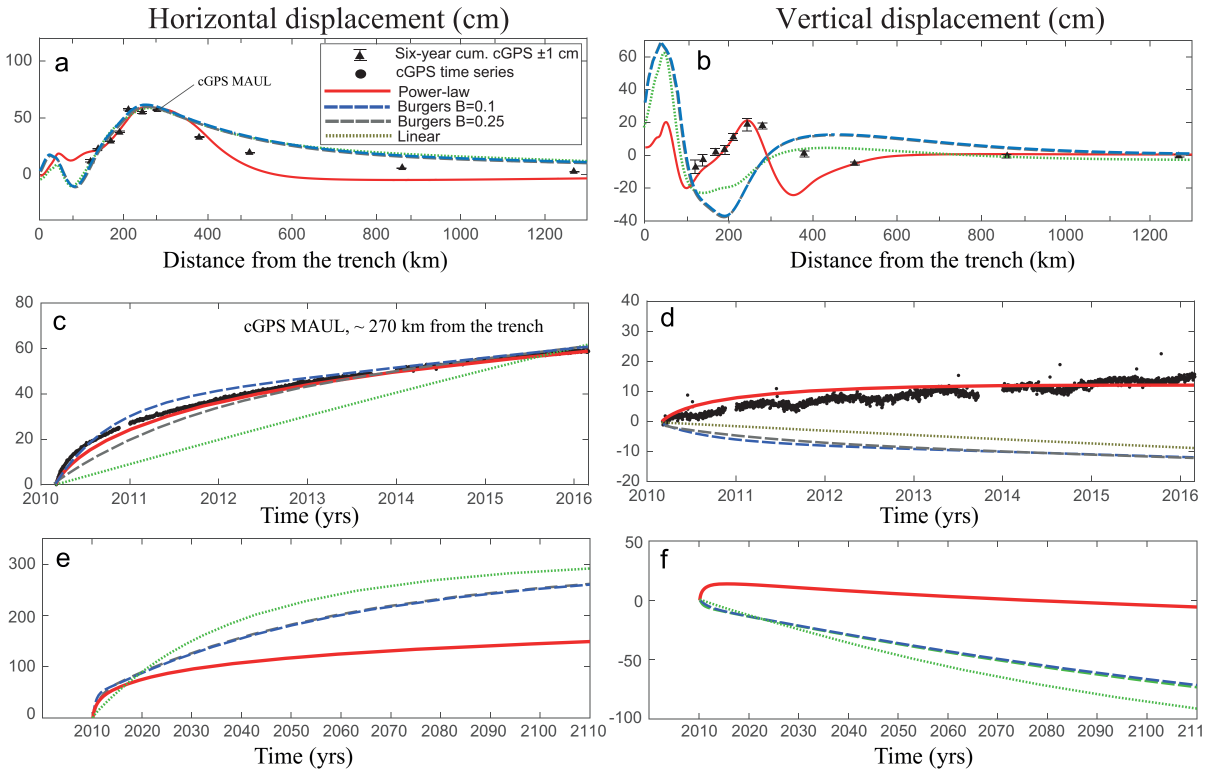

Fig. 6.1 Surface displacements comparison among power-law, linear, and Burgers rheologies using the preferred postseismic simulation (NLA100D20R) from Chapter 3. Left and right panels illustrate the horizontal and vertical components, respectively. a and b represent the cumulative surface displacements from the 2D model. c and d depict the time series over six years at station MAUL. e and f represent the displacement predictions over 100 yrs at station MAUL following the mainshock. Burgers rheology in the upper mantle is implemented through the shear relaxation modulus representation by Prony series expansion, as described in Takeuchi and Fialko (2013). This model with Burgers rheology considers the crust fully elastic. In agreement to previous studies (e.g., Hu et al., 2016; Takeuchi and Fialko, 2012), I used the same shear modulus for the steady-state and transient viscosities. B in a) is the ratio of the transient to the steady-state viscosity with the same linear steady-state viscosity as used in this dissertation. The fault and boundary conditions are identical in all simulations. Further details can be found in Table 3.2 in Chapter 3.

decade of postseismic deformation, the displacements over time from the Burgers rheology model are visibly larger than the ones from power-law rheology. For instance, at station MAUL, the predicted displacements from the Burgers rheology model, compared to the ones from the power-law rheology model, increases in approximately 35% and 50% after 50 and 100 years, respectively. At the moment, and given that ca. one decade has passed since the 2010 Maule and 2011 Tohoku-Oki earthquakes, small differences can be found by using these one-decade GPS observations. Nevertheless, more extended GPS time series in the future will provide further constraints to prove these rheologies.

Additional constraints to discriminate postseismic models can also be found from offshore geodetic data, since the afterslip distribution from my preferred simulation (PL1 in Chapter 4), compared to the ones of Klein et al. (2016) and Weiss et al. (2019), exhibits significant deviations at depths < 25 km. The new methodology proposed in Chapter 4 to discriminate competing postseismic models could also be employed to evaluate these models. Here, I consider visual correlation between afterslip and aftershock moment release, given that the afterslip deviations at greater depths are evident. However, to assess my results against the ones from Klein et al. (2016) and Weiss et al. (2019) better, one should use a more sophisticated afterslip-aftershock correlation approach, such as the Pearson correlation. Hence, offshore and longer geodetic time series and a more afterslip-aftershock correlation approach could provide additional constraints to discriminate postseismic models.

6.2.2 Implications in current knowledge

In this dissertation, I showed the main differences between using linear and power-law rheology models. In particular, power-law rheology models produce postseismic deformation patterns (afterslip and viscous relaxation) that are notably more consistent with the fault interface constraints from seismic and geodetic observations. Additionally, they agree better with the concepts of lithosphere-asthenosphere system strength at subduction zones from laboratory experiments (Bürgmann and Dresen, 2008; Karato, 2010; Rybacki and Dresen, 2000). Therefore, these (power-law) models provide a better estimation of the slip budgets and transfer of stresses during the postseismic period, which is critical to assess the the potential of earthquakes better. Furthermore, and given that afterslip distributions are used as a proxy to evaluate the frictional behaviour of the fault (Avouac, 2015, and references therein), our knowledge of afterslip-based fault frictional behaviour needs revisions at subduction zones.

The extrapolation of laboratory-derived power-law rheology to investigate postseismic processes at lithospheric scales might be questionable since the typical laboratory strain rates (10^{-6}–10^{-4}) are approximately nine orders of magnitude higher than those in nature (10^{-12}–10^{-16}, see Fig. 6.2). Yet, my results provide strong evidence that models considering laboratory-derived power-law rheology enable us to make first-order predictions about how the lithosphere-asthenosphere system responds in the aftermath of the 2010 Maule earthquake. This is also support by recent studies investigating the postseismic deformation associated to earthquakes in Japan (Agata et al., 2019; Barbot, 2020; Muto et al., 2019; Shi et al., 2020b), in the Sumatra-Andaman region in Indonesia (Qiu et al., 2018), as well as previous studies in strike-system fault such as in California in USA (e.g., Freed and Bürgmann, 2004; Freed et al., 2012; Takeuchi and Fialko, 2013). On the other hand, and in contrast to models considering fully elastic or Burgers rheology, model considering power-law rheology with creep processes could also facilitate the investigation in the plastic deformation. Laboratory experiments, using lower-crustal rocks at high temperatures conditions, showed that the dominant deformation mechanisms are dislocation creep processes (e.g., Carter and Kirby, 1978; Kirby and Kronenberg, 1987; Rybacki and Dresen, 2000), which is, in principle, in contrast with postseismic models neglecting viscous deformation in the whole crust. Additionally, the simplest version of the Burgers rheology might not be appropriate to explain seismic wave attenuation (Karato, 2010), but the dislocation motion of minerals provides a better explanation (Karato, 1998).

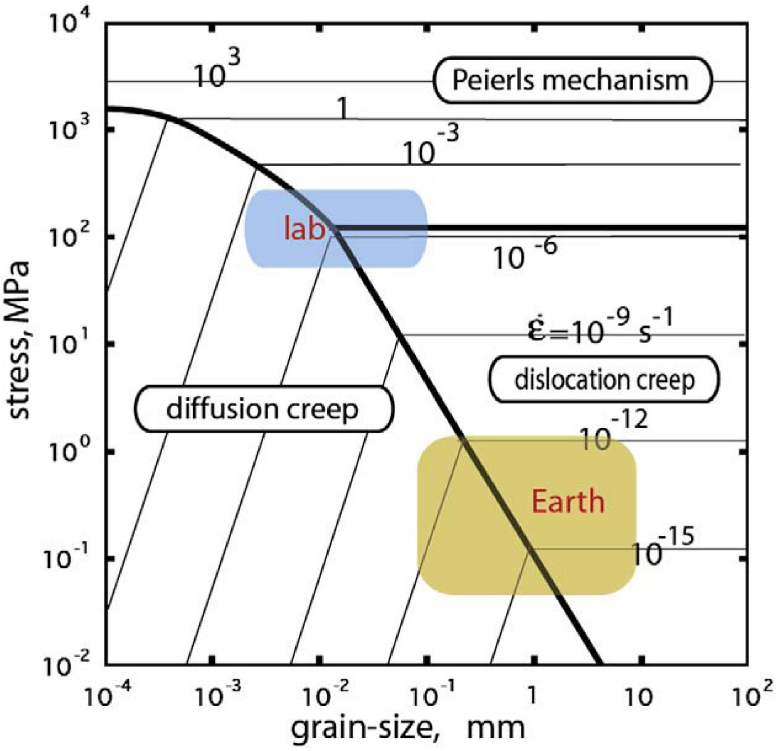

Fig. 6.2 Chart of the deformation mechanisms in olivine at temperature = 1700 K and pressure = 7 GPa. Figure modified from Karato (2010).

The assumption that the whole crust accommodates the deformation only elastically is also in contrast to permanent forearc vertical deformation, as revealed by geomorphic and geologic records in central and northern Chile (Bookhagen et al., 2006; Melnick, 2016). These studies suggest that this permanent deformation accumulates with a rate of $\sim$ 0.01 cm/yr, which represents $\sim$10% of the geodetic vertical annual displacement (Melnick, 2016; Wesson et al., 2015). Nevertheless, existing studies have only employed fully elastic models to hypothesize the possible mechanisms controlling such permanent deformation patterns (Jolivet et al., 2020; Melnick, 2016). Therefore, the potential role of a model considering power-law rheology with plastic creep remains enigmatic.

The use of power-law rheology in postseismic studies could also facilitate the investigation of additional rock parameters, such as water content and melting, which are poorly understood in the lithosphere-asthenosphere system. These parameters are implicit in the pre-factor A in Equation 4.1 and can be written as:

$$A = A'(C_{OH})^r e^{\alpha\phi} \tag{6.1}$$

where A' is a creep material constant, C_{OH} the water content and r its exponent, and α and ϕ are the melt fraction and a constant, respectively (e.g., Hirth and Kohlstedt, 2003; Masuti et al., 2016a). A limitation to overcome, however, is the high uncertainty of these parameters (and the temperature field), which makes an inversion challenging due to the current geodetic postseismic data and the inversion approach employed in this dissertation. In particular, more geodetic data in the volcanic and backarc regions, as the viscous relaxation is dominant there, alongside a more sophisticated inversion approach, such as a Bayesian one, could allow a better exploration and minimization of these uncertainties. In addition, valuable constraints could also be provided by integrating magnetotelluric and seismic (e.g., V_p/V_s ratio) measurements, as they are sensitive to water and/or melting variations (e.g., Brasse and Soyer, 2001; Cordell et al., 2019; Nakajima et al., 2001).

Chapter 7

Conclusions and outlook

7.1 Conclusions

The analysis and results of this dissertation lead to the following conclusions:

- For the first time, I show that models considering afterslip on the fault interface and power-law rheology in the whole crust and upper mantle, can be used to investigate the postseismic deformation following the 2010 Maule earthquake. In particular, my results reveal that these models can explain notably better the cumulative GPS vertical displacements and the GPS time series, in comparison to those that consider linear rheology in the upper mantle and a whole elastic crust.

- I develop a novel approach to investigate postseismic deformation processes, which combines power-law rheology modelling, GPS data, and aftershock activity. If compared to traditional approaches, the postseismic deformation patterns from this innovative approach are in a considerably closer concordance with the frictional properties, along the fault interface and concepts of lithosphere-asthenosphere system strength. It enables, consequently, a better understanding of faulting mechanics properties and quantification of slip budgets.

- The postseismic deformation patterns obtained from this new approach, results in afterslip primarily at depths < 60 km, while non-linear viscous relaxation mostly occurs in the continental lower crust beneath the volcanic arc, due to dislocation creep processes. The continental lower crust acts therefore, as a non-linear viscous medium after megathrust earthquakes and not as a fully elastic one, as commonly believed.

- This novel methodology also facilitates a more accurate assessment of megathrust earthquake triggering under the Coulomb Failure Stresses (CFS) criteria. The Illapel earthquake was not likely triggered directly by the Maule event due to the small, albeit positive CFS values transferred from the Maule one to the Illapel hypocenter. However, additional constraints from seismic and geodetic data are required to examine thoroughly their mechanical connection.

7.2 Outlook

The investigation carried out in the present dissertation has focused on the particular case of the 2010 Maule earthquake and its subsequent postseismic deformation. However, the role of power-law rheology, specially implemented in the continental crust, on postseismic deformation remains poorly understood worldwide. The outstanding postseismic data from the 2014 Iquique earthquake will provide a future key target to investigate postseismic processes. This will also allow to compare and contrast postseismic processes against the case of the 2010 Maule. To examine the controlling postseismic processes and their interplay better, an essential challenge is to minimize the model uncertainty, which are primary produced by the temperature field uncertainties. To do so, the integration of further observations from geodesy (e.g., InSAR), seismology (e.g., seismic tomography), geophysics (e.g., magnetotellurics), and geology will supply additional and insightful constraints. Future research should also be focused on examining the contribution of power-law rheology to processes across the seismic cycle, as interseismic locking and the accumulation of vertical permanent deformation. Particularly, urgent inspection of interseismic locking degrees maps, considering second-order power-law rheology models, is required since locking maps are used as a proxy to forecast location and magnitude of megathrust earthquakes.

Appendix A

Supporting information for Chapter 4

A.1 Content of this file

- Text A1
- Figures S1 to S10

A.2 Background stresses

We consider the 2D model of Peña et al. (2019) to investigate the sensitivity to background stresses. We do so by applying a far-field velocity for several of hundreds of years until the creep strain rates become steady state. Figure S4 shows that the differences by considering a model with and without background stresses are negligible. Our results show that the resulting steady-state viscosity (Figure S5) is comparable to results of Sobolev and Muldashev (2017). They found a steady-state viscosity of $\sim 10^{19}$ Pa s for the upper mantle; however our steady-state viscosity in the lower crust is lower since the differences in rock material assumption for the lower crust.

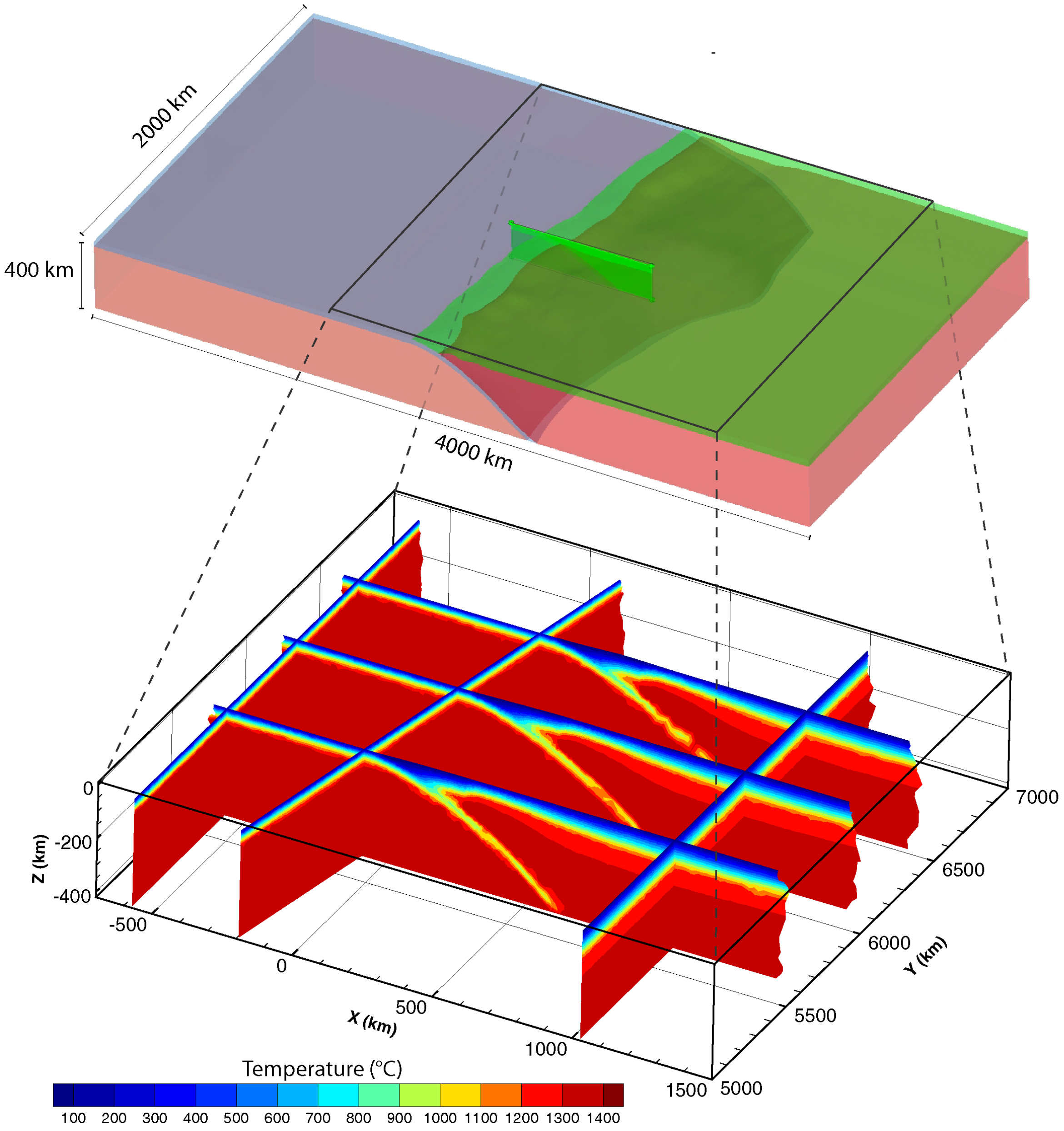

Fig. A.1 Temperature field.

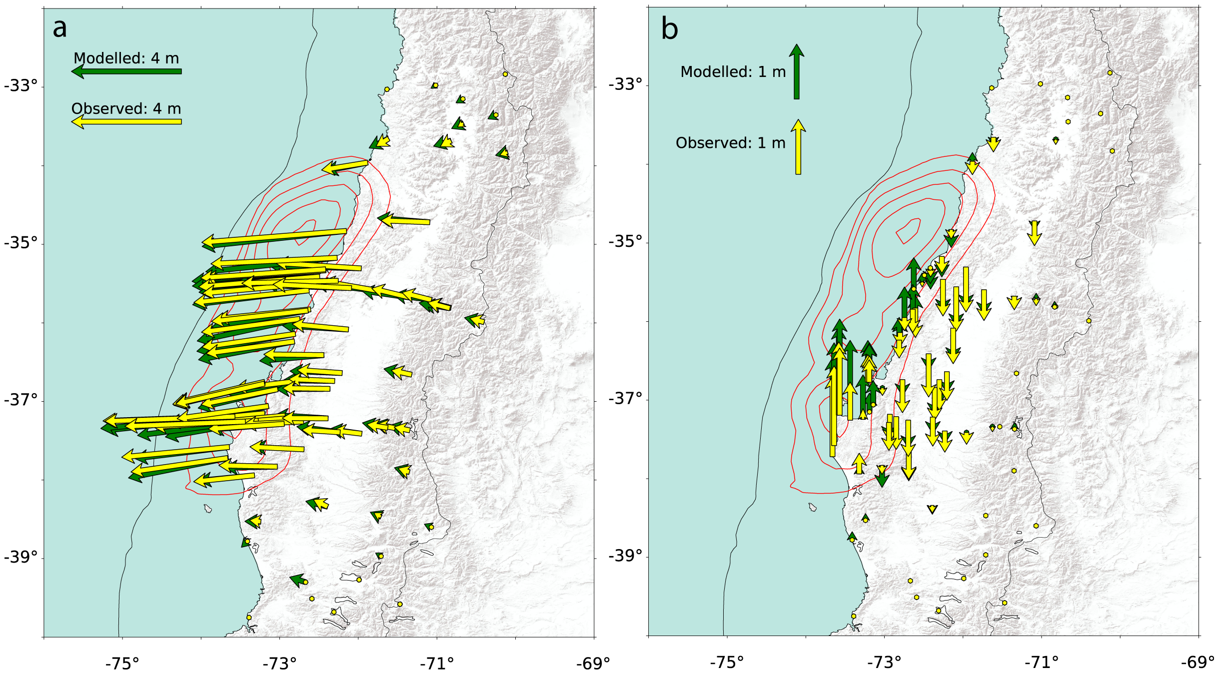

Fig. A.2 Observed versus simulated coseismic displacements. The 3-m coseismic slip contour lines are shown in black. The Mean Absolute Error (MAE) is 0.13 m, while the Root Mean Squared Error (RMSE) is 0.2 m which is in good agreement with the calculated by Moreno et al. (2012) (0.15 m and 0.1m for the horizontal and vertical GPS data, respectively).

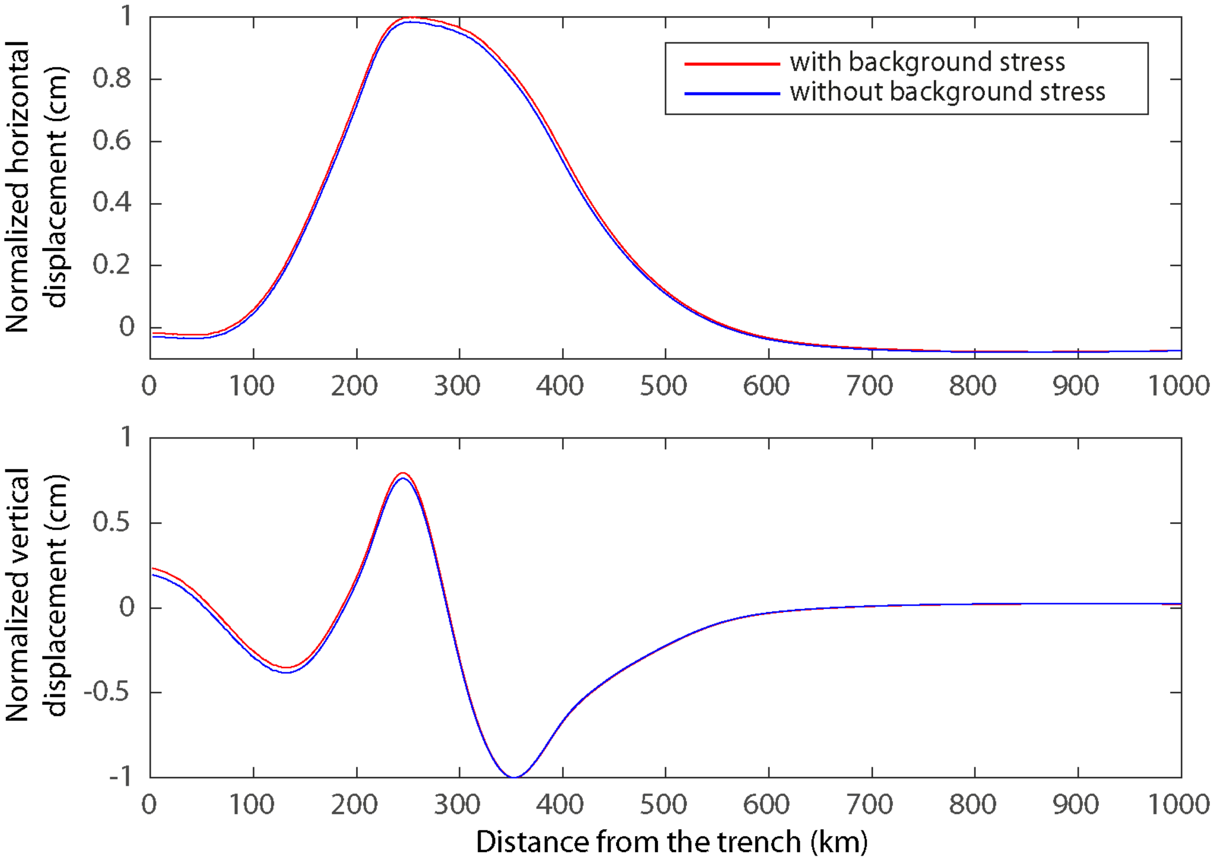

Fig. A.3 Background stresses test. Normalized horizontal and vertical displacements correspond to the cumulative surface displacement after six years of the earthquake simulation.

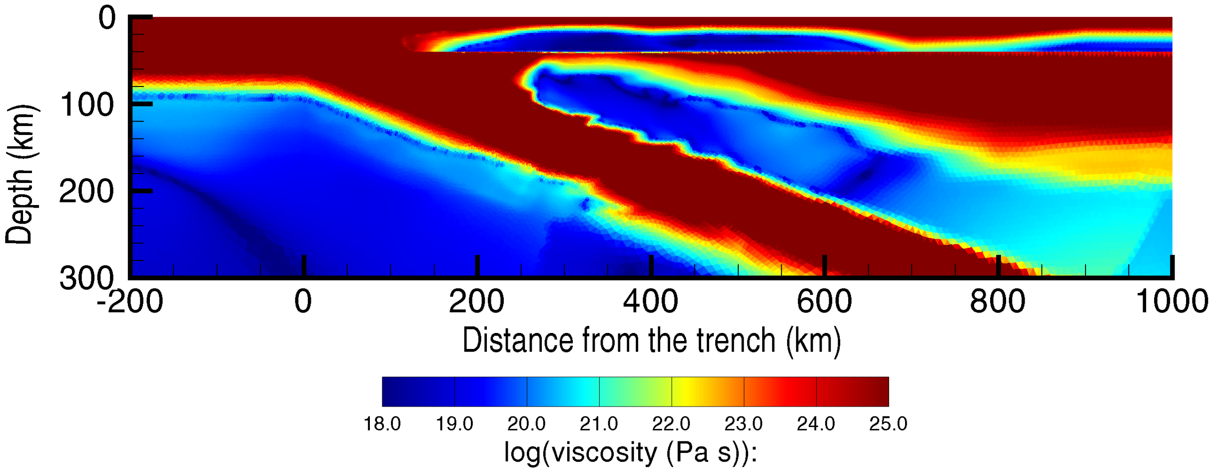

Fig. A.4 Steady-state viscosity.

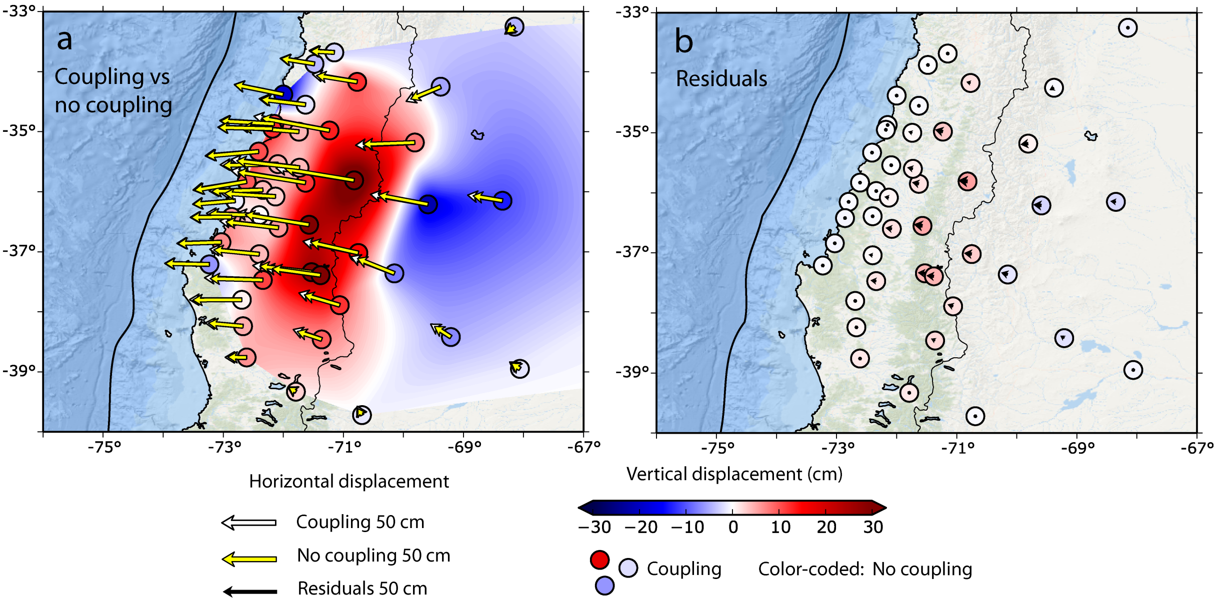

Fig. A.5 Impact of afterslip on the creep strain. We use simulation 1 as it is our preferred simulation (smallest MAE and best correlation with aftershock seismicity). The coupled afterslip-viscoelastic simulation results in an increment of the total surface displacements at cGPS stations of ∼6% compared the simulation considering afterslip and viscoelastic processes acting independently. The MAE is 1.5 cm between these two simulations.

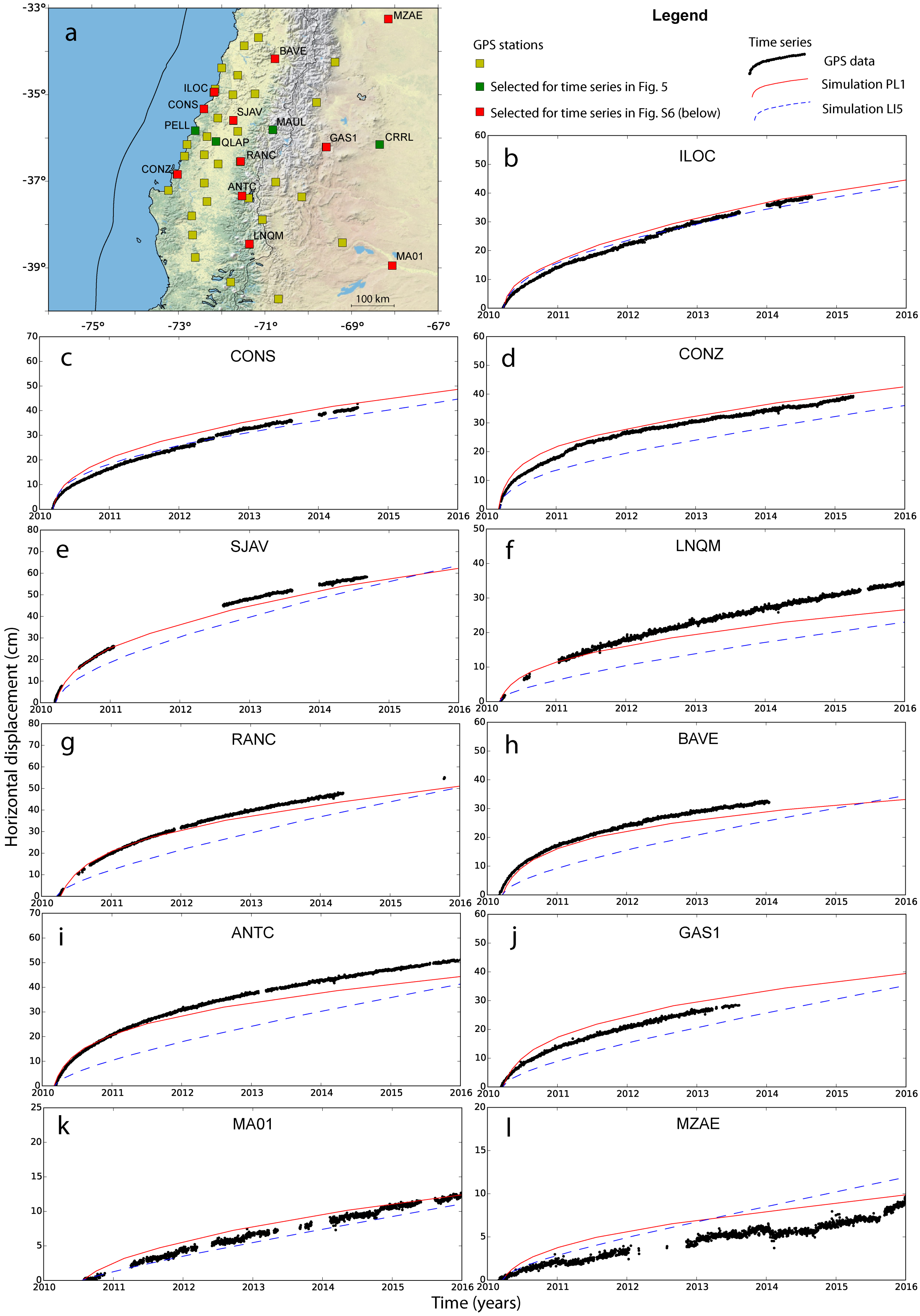

Fig. A.6 GPS Time series. a shows location of 15 time series used in this study. Time series from stations PELL, QLAP, MAUL and CRRL are shown in the main text in Figure 5, while the other 11 are shown from b to l.

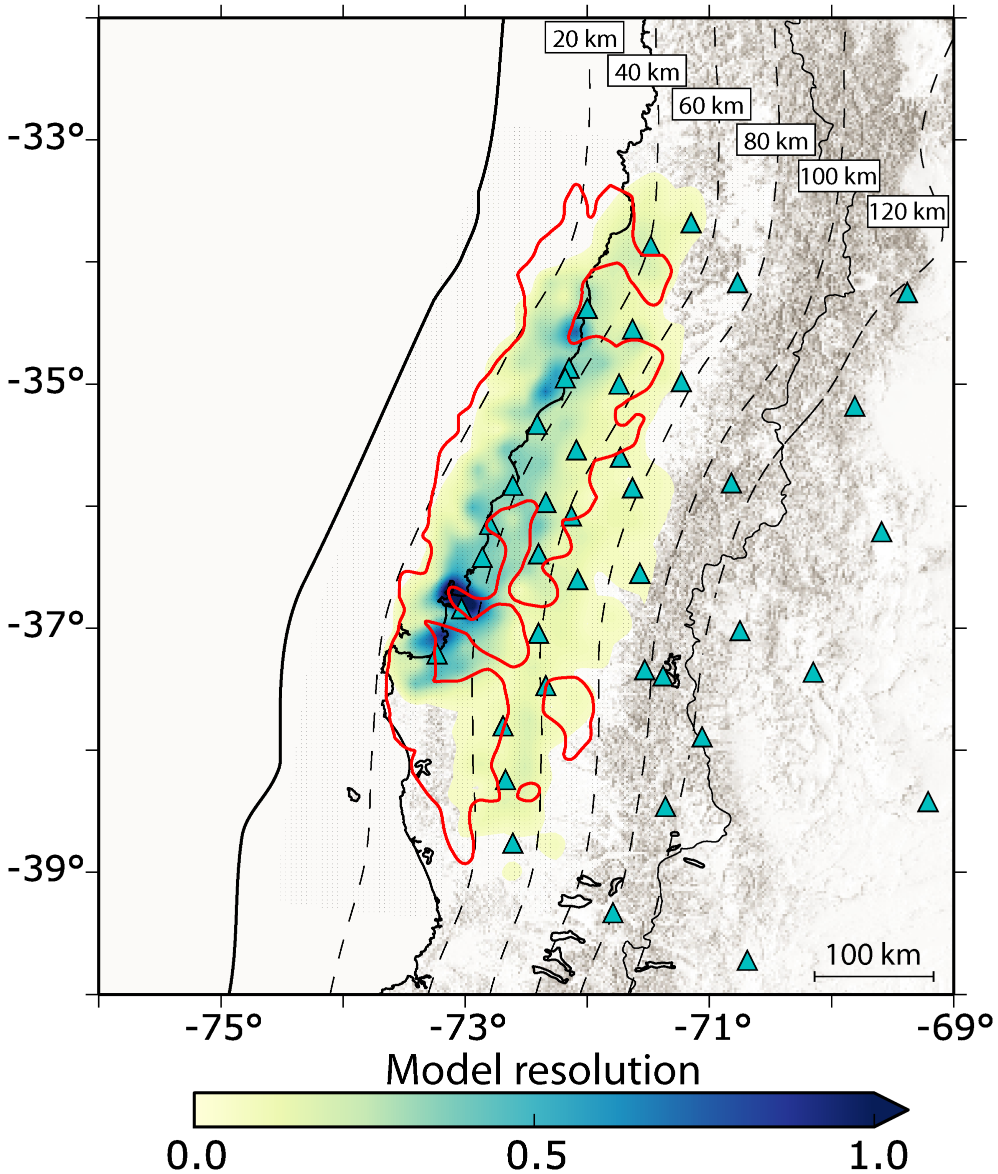

Fig. A.7 Model resolution matrix R calculated as G'G (Tsang et al., 2016). G represents the matrix wtih Green's functions. The color-coded shows the diagonal elements of the matrix R. Red contour lines show the afterslip distribution > 0.3 m from our preferred simulation.

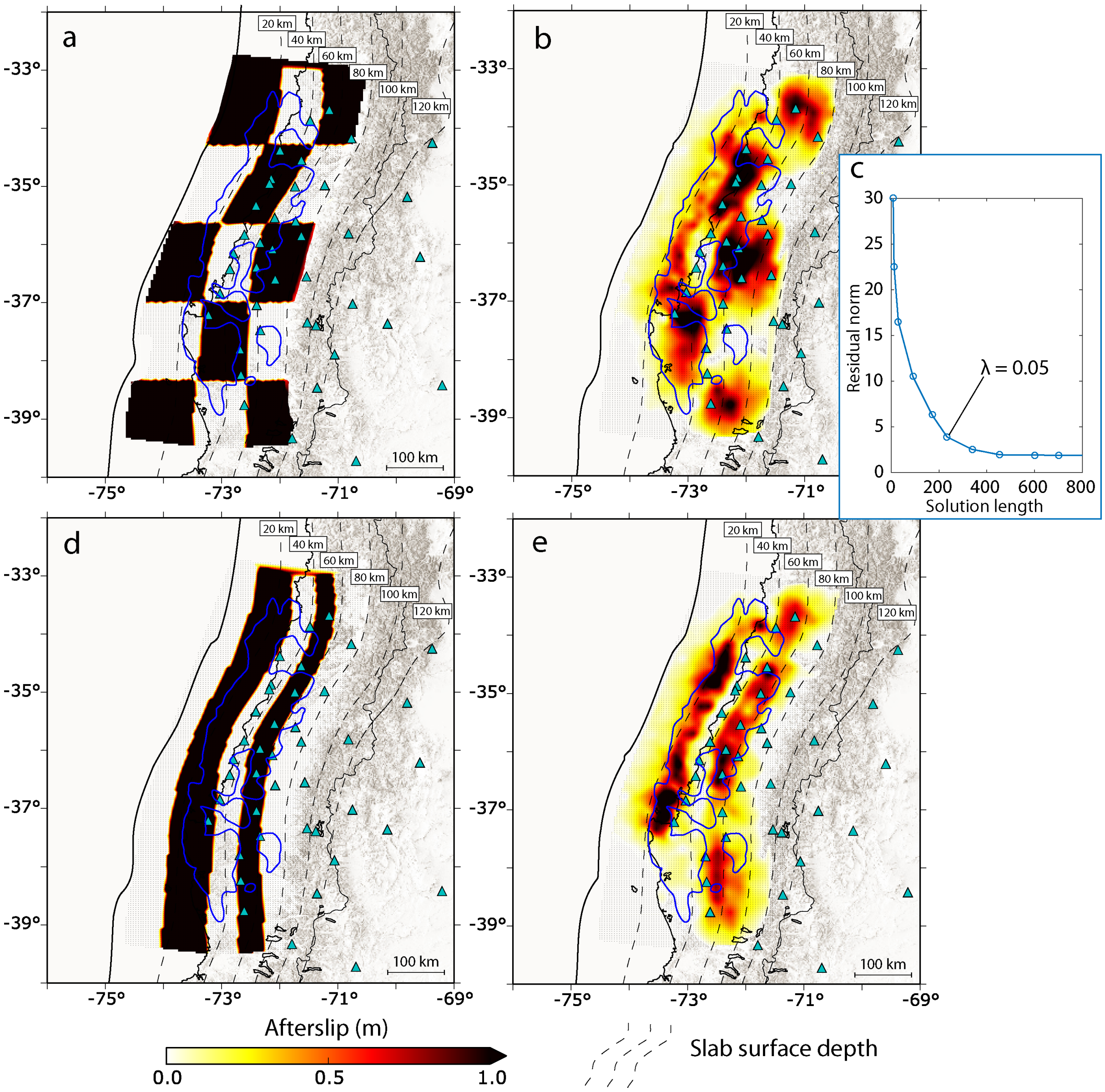

Fig. A.8 Checkerboard tests to investigate our capability of resolving fault patches. Blue contour lines show the afterslip distribution > 0.3 m from our preferred simulation. In a, d can be seen the afterslip input, which is recovered in b, e. c shows the smoothing constant as a function of the Residual Norm and the Solution length. The latter is $\sum |s|$, where s corresponds to the afterslip inverted on each sub-fault (Masterlark, 2003). Following the L-curve criteria (e.g. Bedford et al., 2013; Masterlark, 2003), we selected a smoothing constant value of 0.05.

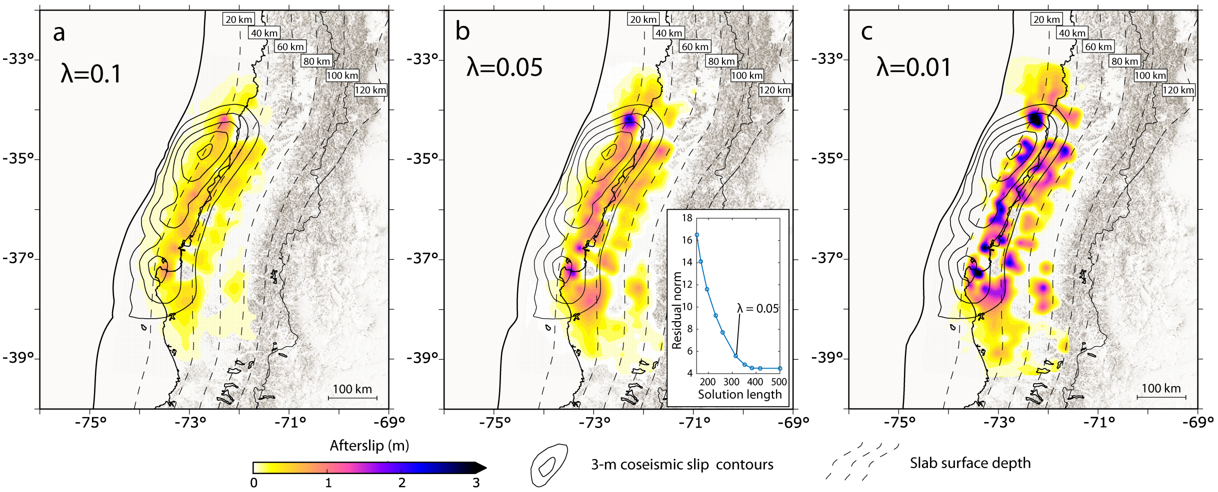

Fig. A.9 Effect of smoothing constant on preferred afterslip distribution.

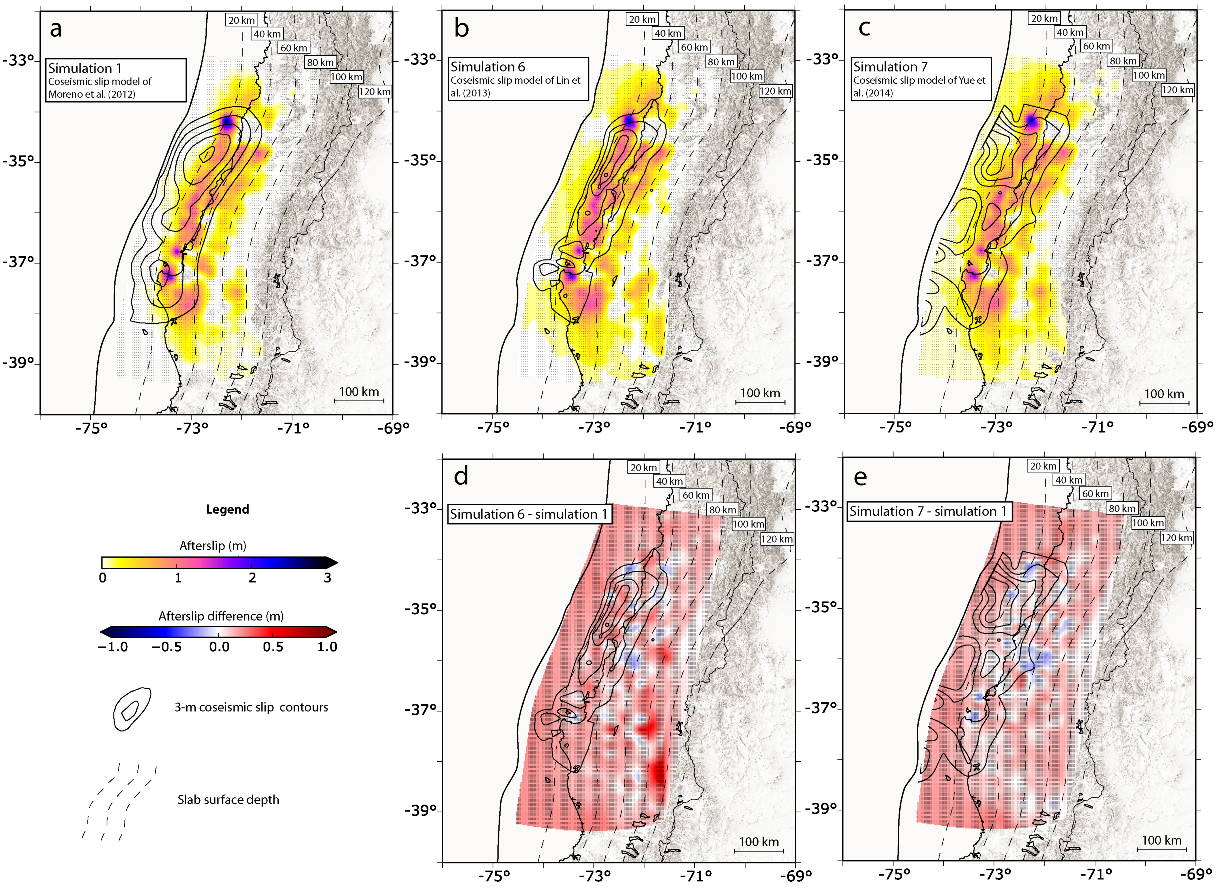

Fig. A.10 Effect of coseismic slip on afterslip distribution on our preferred simulation 1 (PL1). b and c consider the same elastic and creep parameters as our preferred simulation, but b and c consider the coseismic slip from Lin et al. (2013)(simulation 6) and Yue et al. (2014)(simulation 7), respectively. d and e correspond to afterslip differences between simulations 6-7 and simulation 1. Note that the overall deviation from simulation is small. The main deviations from simulation 1 (PL1) and 6 in the southern, deeper segment might probably be because of the fault geometry implementation (two planar fault with different dip and strike angles to resemble variation on the fault interface) and data used during the inversion approach by Lin et al. (2013).

Appendix B

Curriculum Vitae

For reasons of data protection, the Curriculum Vitae is not published in the electronic version.

Acknowledgements

First of all, I would sincerely like to thank my supervisors, Onno Oncken and Oliver Heidbach, for giving me the chance to be part of the Freie Berlin Universität and Helmholtz GFZ-Potsdam Centre. I want to express my sincere gratitude to Oliver for his day-to-day guidance, support, and insightful discussions. I thank Onno for his thoughtful comments, which made me grow considerably scientifically. It has truly been a pleasure to work for you. I would also like to thank the bilateral scholarship granted by the German Academic Exchange Service (DAAD) and the National Commission for Scientific and Technological Research (CONICYT-Becas Chile). I also want to express my gratitude to the Initiative and Networking Fund of the Helmholtz Association through the project "Advanced Earth System Modelling Capacity (ESM)".

Secondary, I would like to acknowledge Marcos Moreno, Jonathan Bedford, Moritz Ziegler, and Andrés Tassara for their illuminating comments on my work. A special thanks go to Marcos Moreno. He guided much of the work, always providing innovative ideas and support in the scientific and personal aspects. My deepest gratitude to Klaus Bataille and Juan Carlos Báez for pushing me, when I was a student in Chile, to continue my career in the old continent. I thank colleagues (and friends) of sections 2.1 and 2.6 (Ayleen Gaete, Malte Ziebarth, Carla Valenzuela, Henning Lilienkamp, and more) and from other sections and all over the world (Hugo Soto, Sriram Reddy, Toño Bayona, Felipe Vera, Camila Novoa, Carlos Conejero, Shaoyang Li, Fabién Salgado, Melany Muñoz, Camilo Márquez, Natalia Carmona, among many others) for the welcoming atmosphere and the great time having scientific and *Feierabend* meetings. In addition, I could not have completed this dissertation without the support of my *non–geosciences* friends (Lesly Vargas, Hermán Martínez, Moritz Voges, Sebastián Zuñiga, SV Solidarität, and and many others), who provided stimulating discussions as well as happy distractions to rest my mind outside of my research. I also wish to thank Uwe Lemgo, Dorina Kroll, Solveig Strutzke, Franziska Alberg, and Susanne Köster for their assistance in administrative and technical concerns.

Last but not least, I would like to extend warm thanks to my parents, Raúl and Cármen, my sister, Alexandra, and the rest of my family for their endless love. In particular, to my grandma Rebeca, of whom I have healthy envy, as she has experienced several earthquakes from almost one century; and to Adriana, *mi rolita*, for her patient, wisdom, and filling each of my days with her wholehearted love.

¡Gracias Totales!

Declaration

I hereby declare that, except where specific reference is made to the work of others, the contents of this dissertation are original and have not been submitted in whole or in part for consideration for any other degree or qualification in this, or any other university. This dissertation is my own work and contains nothing which is the outcome of work done in collaboration with others, except as specified in the text and Acknowledgements. This dissertation contains fewer than 65,000 words including appendices, bibliography, footnotes, tables and equations and has fewer than 150 figures.

Carlos Peña Hormazábal
October 2020

References

Agata, R., Barbot, S. D., Fujita, K., Hyodo, M., Iinuma, T., Nakata, R., Ichimura, T., and Hori, T. (2019). Rapid mantle flow with power-law creep explains deformation after the 2011 tohoku mega-quake. *Nature communications*, 10(1):1385.

Aguirre, L., Bataille, K., Novoa, C., Peña, C., and Vera, F. (2019). Kinematics of subduction processes during the earthquake cycle in central chile. *Seismological Research Letters*.

Agurto, H., Rietbrock, A., Ryder, I., and Miller, M. (2012). Seismic-afterslip characterization of the 2010 mw 8.8 maule, chile, earthquake based on moment tensor inversion. *Geophysical Research Letters*, 39(20).

Agurto-Detzel, H., Font, Y., Charvis, P., Régnier, M., Rietbrock, A., Ambrois, D., Paulatto, M., Alvarado, A., Beck, S., and Courboulex, F. (2019). Ridge subduction and afterslip control aftershock distribution of the 2016 mw 7.8 ecuador earthquake. *Earth and Planetary Science Letters*, 520:63–76.

Anderson, D. L. (1975). Accelerated plate tectonics. *Science*, 187(4181):1077–1079.

Avouac, J.-P. (2015). From geodetic imaging of seismic and aseismic fault slip to dynamic modeling of the seismic cycle. *Annual Review of Earth and Planetary Sciences*, 43:233–271.

Barbot, S. (2018a). Asthenosphere flow modulated by megathrust earthquake cycles. *Geophysical Research Letters*, 45(12):6018–6031.

Barbot, S. (2018b). Asthenosphere flow modulated by megathrust earthquake cycles. *Geophysical Research Letters*, 45(12):6018–6031.

Barbot, S. (2020). Frictional and structural controls of seismic super-cycles at the japan trench. *Earth, Planets and Space*, 72:1–25.

Barrientos, S. E., Plafker, G., and Lorca, E. (1992). Postseismic coastal uplift in southern chile. *Geophysical Research Letters*, 19(7):701–704.

Barrientos, S. E. and Ward, S. N. (1990). The 1960 Chile earthquake: inversion for slip distribution from surface deformation. *Geophysical Journal International*, 103(3):589–598.

Bedford, J., Moreno, M., Baez, J., Lange, D., Tilman, F., Rosenau, M., Heidbach, O., Oncken, O., Ryder, I., Bevis, M., Bartsch, M., and Vigny, C. (2013). A high-resolution, time-variable afterslip model for the 2010 maule mw=8.8, chile megathrust earthquake. *Earth Planet. Sci. Lett.*, 383:doi: 10.1016/j.epsl.2013.09.020, 26–36.

Bedford, J., Moreno, M., Li, S., Oncken, O., Baez, J. C., Bevis, M., Heidbach, O., and Lange, D. (2016). Separating rapid relocking, afterslip, and viscoelastic relaxation: An application of the postseismic straightening method to the maule 2010 cgps. *Journal of Geophysical Research: Solid Earth*, 121(10):7618–7638.

References

Ben-Menahem, A. (1995). A concise history of mainstream seismology: Origins, legacy, and perspectives. *Bulletin of the Seismological Society of America*, 85(4):3087–3101.

Bevis, M., Brooks, B., Smalley, R., Baez, J., Parra, H., Kendrick, E., Foster, J., Blanco, M., Simons, M., Caccamise, D., et al. (2010). The 2010 (m 8.8) maule, chile earthquake: an overview of the emergency geodetic response and some of its early findings. *AGUFM*, 2010:U21B–04.

Bevis, M. and Brown, A. (2014). Trajectory models and reference frames for crustal motion geodesy. *Journal of Geodesy*, 88(3):283–311.

Bilak, A., Cardona-Fox, G., Ginnetti, J., Rushing, E. J., Scherer, I., Swain, M., Walicki, N., and Yonetani, M. (2016). *Global report on internal displacement*. International Displacement Monitoring Centre.

Blewitt, G. (2018). Nevada geodetic laboratory station id: Coso. *Data set at: http://geodesy. unr. edu/NGLStationPages/stations/COSJ. sta.*

Bookhagen, B., Echtler, H. P., Melnick, D., Strecker, M. R., and Spencer, J. Q. (2006). Using uplifted holocene beach berms for paleoseismic analysis on the santa maría island, south-central chile. *Geophysical Research Letters*, 33(15).

Brace, W. and Kohlstedt, D. (1980). Limits on lithospheric stress imposed by laboratory experiments. *Journal of Geophysical Research: Solid Earth*, 85(B11):6248–6252.

Brasse, H. and Soyer, W. (2001). A magnetotelluric study in the southern chilean andes. *Geophysical Research Letters*, 28(19):3757–3760.

Burgers, J. (1935). Mechanical considerations-model systems-phenomenological theories of relaxation and of viscosity. *First report on viscosity and plasticity*, 1.

Bürgmann, R. and Dresen, G. (2008). Rheology of the lower crust and upper mantle: Evidence from rock mechanics, geodesy and field observations. *Ann. Review of Earth and Planet. Sc.*, 36:531–567.

Carter, N. L. and Kirby, S. H. (1978). Transient creep and semibrittle behavior of crystalline rocks. In *Rock Friction and Earthquake Prediction*, pages 807–839. Springer.

Chlieh, M., Avouac, J.-P., Hjorleifsdottir, V., Song, T.-R. A., Ji, C., Sieh, K., Sladen, A., Hebert, H., Prawirodirdjo, L., and Bock, Y. (2007). Coseismic slip and afterslip of the great m w 9.15 sumatra–andaman earthquake of 2004. *Bulletin of the Seismological Society of America*, 97(1A):S152–S173.

Chopra, P. N. (1997). High-temperature transient creep in olivine rocks. *Tectonophysics*, 279(1-4):93–111.

Christensen, N. I. (1996). Poisson's ratio and crustal seismology. *Journal of Geophysical Research: Solid Earth*, 101(B2):3139–3156.

Contreras-Reyes, E., Grevemeyer, I., Flueh, E. R., and Reichert, C. (2008). Upper lithospheric structure of the subduction zone offshore of southern arauco peninsula, chile, at 38 s. *Journal of Geophysical Research: Solid Earth*, 113(B7).

Cordell, D., Unsworth, M. J., Diaz, D., Reyes-Wagner, V., Currie, C. A., and Hicks, S. P. (2019). Fluid and melt pathways in the central chilean subduction zone near the 2010 maule earthquake (35°-36° s) as inferred from magnetotelluric data. *Geochemistry, Geophysics, Geosystems*.

Courant, R. (1943). Variational methods for the solution of problems of equilibrium and vibrations. *Bulletin of the American Mathematical Society*, 49(1-23).

Daniell, J. E., Daniell, K. A., Daniell, T. M., Khazai, B., et al. (2010). A country level physical and community risk index in the asia-pacific region for earthquakes and floods. In *5th Civil Engineering Conference in the Asian Region and Australasian Structural Engineering Conference 2010, The*, page 610. Engineers Australia.

Diao, F., Xiong, X., Wang, R., Zheng, Y., Walter, T. R., Weng, H., and Li, J. (2014). Overlapping post-seismic deformation processes: Afterslip and viscoelastic relaxation following the 2011 m w 9.0 tohoku (japan) earthquake. *Geophysical Journal International*, 196(1):218–229.

Dielforder, A., Hetzel, R., and Oncken, O. (2020). Megathrust shear force controls mountain height at convergent plate margins. *Nature*, 582(7811):225–229.

Dragert, H., Wang, K., and James, T. S. (2001). A silent slip event on the deeper cascadia subduction interface. *Science*, 292(5521):1525–1528.

Farías, M., Comte, D., Charrier, R., Martinod, J., David, C., Tassara, A., Tapia, F., and Fock, A. (2010). Crustal-scale structural architecture in central chile based on seismicity and surface geology: Implications for andean mountain building. *Tectonics*, 29(3).

Feng, G., Li, Z., Shan, X., Zhang, L., Zhang, G., and Zhu, J. (2015). Geodetic model of the 2015 april 25 m w 7.8 gorkha nepal earthquake and m w 7.3 aftershock estimated from insar and gps data. *Geophysical journal international*, 203(2):896–900.

Freed, A. M. (2005). Earthquake triggering by static, dynamic, and postseismic stress transfer. *Annu. Rev. Earth Planet. Sci.*, 33:335–367.

Freed, A. M. and Bürgmann, R. (2004). Evidence of power-law flow in the mojave desert mantle. *Nature*, 430(6999):548.

Freed, A. M., Hashima, A., Becker, T. W., Okaya, D. A., Sato, H., and Hatanaka, Y. (2017). Resolving depth-dependent subduction zone viscosity and afterslip from postseismic displacements following the 2011 tohoku-oki, japan earthquake. *Earth and Planetary Science Letters*, 459:279–290.

Freed, A. M., Hirth, G., and Behn, M. D. (2012). Using short-term postseismic displacements to infer the ambient deformation conditions of the upper mantle. *Journal of Geophysical Research: Solid Earth*, 117(B1).

Freed, A. M. and Lin, J. (2001). Delayed triggering of the 1999 hector mine earthquake by viscoelastic stress transfer. *Nature*, 411(6834):180–183.

Ghan, S., Crawford, J., Langematz, U., Leung, R., Li, Z., Russell, L., Steiner, A., and Zhang, C. (2016). Author contributions can be clarified. *Journal of Geophysical Research: Atmospheres*, 121(14):8155–8155.

Gokhale, N. S. (2008). *Practical finite element analysis*. Finite to infinite.

González-Vidal, D., Obermann, A., Tassara, A., Bataille, K., and Lupi, M. (2018). Crustal model of the southern central andes derived from ambient seismic noise rayleigh-wave tomography. *Tectonophysics*, 744:215–226.

Govers, R., Furlong, K., Van de Wiel, L., Herman, M., and Broerse, T. (2018). The geodetic signature of the earthquake cycle at subduction zones: Model constraints on the deep processes. *Reviews of Geophysics*, 56(1):6–49.

References

Griggs, D. and Blacic, J. (1965). Quartz: anomalous weakness of synthetic crystals. *Science*, 147(3655):292–295.

Hardebeck, J. L. and Loveless, J. P. (2018). Creeping subduction zones are weaker than locked subduction zones. *Nature Geoscience*, 11(1):60–64.

Hayes, G. P., Wald, D. J., and Johnson, R. L. (2012). Slab1. 0: A three-dimensional model of global subduction zone geometries. *Journal of Geophysical Research: Solid Earth*, 117(B1).

Heidarzadeh, M., Murotani, S., Satake, K., Ishibe, T., and Gusman, A. R. (2016). Source model of the 16 september 2015 illapel, chile, mw 8.4 earthquake based on teleseismic and tsunami data. *Geophysical Research Letters*, 43(2):643–650.

Heki, K. and Mitsui, Y. (2013). Accelerated pacific plate subduction following interplate thrust earthquakes at the japan trench. *Earth and Planetary Science Letters*, 363:44–49.

Hergert, T. and Heidbach, O. (2006). New insights in the mechanism of postseismic stress relaxation exemplified by the june 23rd 2001 mw = 8.4 earthquake in southern peru. *Geophysical Research Letters*, 33(L02307):doi:1029/2005GL024585.

Hirth, G. and Kohlstedt, D. (2003). Inside the subduction factory. *Rheology of the Upper Mantle and the Mantle Wedge: A View From the Experimentalists, Geophys. Monogr. Ser*, 138:83–105.

Hirth, G. and Kohlstedt, D. L. (1996). Water in the oceanic upper mantle: implications for rheology, melt extraction and the evolution of the lithosphere. *Earth and Planetary Science Letters*, 144(1-2):93–108.

Hirth, G. and Tullis, J. (1994). The brittle-plastic transition in experimentally deformed quartz aggregates. *Journal of Geophysical Research*, 99(B6):11731–11747.

Hrennikoff, A. (1941). Solution of problems of elasticity by the framework method. *J. appl. Mech.*

Hsu, Y.-J., Simons, M., Avouac, J., Galetzka, J., Sieh, K., Chlieh, M., Natawidjaja, D., Prawirodirdjo, L., and Bock, Y. (2006). Frictional afterslip following the 2005 nias-simeulue earthquake, sumatra. *Science*, 312:1921–1926.

Hu, Y., Bürgmann, R., Uchida, N., Banerjee, P., and Freymueller, J. T. (2016). Stress-driven relaxation of heterogeneous upper mantle and time-dependent afterslip following the 2011 tohoku earthquake. *Journal of Geophysical Research: Solid Earth*, 121(1):385–411.

Hu, Y., Bürgmann, R., Freymueller, J. T., Banerjee, P., and Wang, K. (2014). Contributions of poroelastic rebound and a weak volcanic arc to the postseismic deformation of the 2011 tohoku earthquake. *Earth, Planets and Space*, 66(1):106.

Hu, Y. and Wang, K. (2012). Spherical-earth finite element model of short-term postseismic deformation following the 2004 sumatra earthquake. *Journal of Geophysical Research: Solid Earth*, 117(B5).

Hu, Y., Wang, K., He, J., Klotz, J., and Khazaradze, G. (2004). Three-dimensional viscoelastic finite element model for postseismic deformation of the great 1960 chile earthquake. *Journal of Geophysical Research: Solid Earth*, 109(B12).

Hughes, K., Masterlark, T., and Mooney, W. (2010). Poroleastic stress-triggering of the 2005 m8.7 nias earthquake by the 2004 m9.2 sumatra-andaman earthquake. *Earth Planet. Sci. Lett*, page doe:10.1016/j.epsl.2010.02.043.

Isacks, B., Oliver, J., and Sykes, L. R. (1968). Seismology and the new global tectonics. *Journal of Geophysical Research*, 73(18):5855–5899.

Jolivet, R., Simons, M., Duputel, Z., Olive, J.-A., Bhat, H., and Bletery, Q. (2020). Interseismic loading of subduction megathrust drives long-term uplift in northern chile. *Geophysical Research Letters*, 47(8):e2019GL085377.

Karato, S. (1986). Does partial melting reduce the creep strength of the upper mantle? *Nature*, 319(6051):309–310.

Karato, S.-i. (1998). A dislocation model of seismic wave attenuation and micro-creep in the earth: Harold jeffreys and the rheology of the solid earth. *Pure and Applied Geophysics*, 153(2-4):239–256.

Karato, S.-i. (2010). Rheology of the earth's mantle: A historical review. *Gondwana Research*, 18(1):17–45.

Karato, S.-i. and Wu, P. (1993). Rheology of the upper mantle: A synthesis. *Science*, 260(5109):771–778.

Kato, N. (2007). Expansion of aftershock areas caused by propagating post-seismic sliding. *Geophysical Journal International*, 168(2):797–808.

Khazaradze, G., Wang, K., Klotz, J., Hu, Y., and He, J. (2002). Prolonged post-seismic deformation of the 1960 great chile earthquake and implications for mantle rheology. *Geophysical Research Letters*, 29(22):7–1–7–4.

King, G. C., Stein, R. S., and Lin, J. (1994). Static stress changes and the triggering of earthquakes. *Bulletin of the Seismological Society of America*, 84(3):935–953.

Kirby, S. H. and Kronenberg, A. K. (1987). Rheology of the lithosphere: Selected topics. *Reviews of Geophysics*, 25(6):1219–1244.

Klein, E., Fleitout, L., Vigny, C., and Garaud, J. (2016). Afterslip and viscoelastic relaxation model inferred from the large-scale post-seismic deformation following the 2010 m w 8.8 maule earthquake (chile). *Geophysical Journal International*, 205(3):1455–1472.

Klotz, J., Abolghasem, A., Khazaradze, G., Heinze, B., Vietor, T., Hackney, R., Bataille, K., Maturana, R., Viramonte, J., and Perdomo, R. (2006). Long-term signals in the present-day deformation field of the central and southern andes and constraints on the viscosity of the earth's upper mantle. In *The Andes*, pages 65–89. Springer.

Klotz, J., Angermann, D., Michel, G. E., Porth, R., Reigber, C., Reinking, J., Viramonte, J., Perdomo, R., Rios, V. H., Barrientos, S., Barriga, R., and Cifuentes, O. (1999). Gps-derived deformation of the central andes including the 1995 antofagasta mw=8.0 earthquake. *Pure and Applied Geophysics*, 154:709–730.

Lambert, V. and Barbot, S. (2016). Contribution of viscoelastic flow in earthquake cycles within the lithosphere-asthenosphere system. *Geophysical Research Letters*, 43(19):10–142.

Lamontagne, M. and Ranalli, G. (1996). Thermal and rheological constraints on the earthquake depth distribution in the charlevoix, canada, intraplate seismic zone. *Tectonophysics*, 257(1):55–69.

Lange, D., Bedford, J., Moreno, M., Tilmann, F., Baez, J., Bevis, M., and Krueger, F. (2014). Comparison of postseismic afterslip models with aftershock seismicity for three subduction-zone earthquakes: Nias 2005, maule 2010 and tohoku 2011. *Geophysical Journal International*, 199(2):784–799.

References

Lange, D., Tilmann, F., Barrientos, S. E., Contreras-Reyes, E., Methe, P., Moreno, M., Heit, B., Agurto, H., Bernard, P., Vilotte, J.-P., and Beck, S. (2012). Aftershock seismicity of the 27 february 2010 mw 8.8 maule earthquake rupture zone. *Earth and Planetary Science Letters*, 317-318:413–425.

Lay, T., Kanamori, H., Ammon, C. J., Koper, K. D., Hutko, A. R., Ye, L., Yue, H., and Rushing, T. M. (2012). Depth-varying rupture properties of subduction zone megathrust faults. *Journal of Geophysical Research: Solid Earth*, 117(B4).

Lay, T., Kanamori, H., Ammon, C. J., Nettles, M., Ward, S. N., Aster, R. C., Beck, S. L., Bilek, S. L., Brudzinski, M. R., Butler, R., et al. (2005). The great sumatra-andaman earthquake of 26 december 2004. *Science*, 308(5725):1127–1133.

Li, S., Bedford, J., Moreno, M., Barnhart, W. D., Rosenau, M., and Oncken, O. (2018). Spatiotemporal variation of mantle viscosity and the presence of cratonic mantle inferred from 8 years of postseismic deformation following the 2010 maule, chile, earthquake. *Geochemistry, Geophysics, Geosystems*, 19(9):3272–3285.

Li, S., Moreno, M., Bedford, J., Rosenau, M., Heidbach, O., Melnick, D., and Oncken, O. (2017). Postseismic uplift of the andes following the 2010 maule earthquake: Implications for mantle rheology. *Geophysical Research Letters*, 44(4):1768–1776.

Lin, Y. N., Sladen, A., Ortega-Culaciati, F., Simons, M., Avouac, J., Fielding, E. J., Brooks, B. A., Bevis, M., Genrich, J., and Rietbrock, A. (2013). Coseismic and postseismic slip associated with the 2010 maule earthquake, chile: Characterizing the arauco peninsula barrier effect. *Journal of Geophysical Research: Solid Earth*, 118(6):3142–3159.

Loveless, J., Pritchard, M., and Kukowski, N. (2009). Testing mechanisms of subduction zone segmentation and seismogenesis with slip distributions from recent andean earthquakes. *Tectonophysics*, page doi:10.1016/j.tecto.2009.05.008.

Loveless, J. P. and Meade, B. J. (2010). Geodetic imaging of plate motions, slip rates, and partitioning of deformation in japan. *Journal of Geophysical Research: Solid Earth*, 115(B2).

Loveless, J. P. and Meade, B. J. (2016). Two decades of spatiotemporal variations in subduction zone coupling offshore japan. *Earth and Planetary Science Letters*, 436:19–30.

Lowry, A. (2006). Resonant slow fault slip in subduction zones forced by climatic load stress. *Nature*, 442:10.1038/nature05055.

Mandal, P. (2018). Evidence of a large triggered event in the nepal himalaya following the gorkha earthquake: Implications toward enhanced seismic hazard. *Pure and Applied Geophysics*, 175(8):2807–2819.

Marone, C., Scholz, C., and Bilham, R. (1991). On the mechanics of earthquake afterslip. *Journal of Geophysical Research*, 96(B5):8441–8452.

Masterlark, T. (2003). Finite element model predictions of static deformation from dislocation sources in a subduction zone : Sensitivities to homogeneous, isotropic, poission-solid, and half-space assumptions. *Journal of Geophysical Research*, pages doi: 10.1029/2002JB002296 1–17.

Masterlark, T., DeMets, C., Wang, H., Sanchez, O., and Stock, J. (2001). Homogeneous vs heterogeneous subduction zone models: Coseismic and postseismic deformation. *Geophysical research letters*, 28(21):4047–4050.

Masuti, S., Barbot, S. D., Karato, S.-i., Feng, L., and Banerjee, P. (2016a). Upper-mantle water stratification inferred from observations of the 2012 indian ocean earthquake. *Nature*, 538(7625):373–377.

Masuti, S., Barbot, S. D., Karato, S.-i., Feng, L., and Banerjee, P. (2016b). Upper-mantle water stratification inferred from observations of the 2012 indian ocean earthquake. *Nature*, 538(7625):373.

Maxwell, J. C. (1867). Iv. on the dynamical theory of gases. *Philosophical transactions of the Royal Society of London*, (157):49–88.

McCloskey, J., Nalbant, S. S., and Steacy, S. (2005). Earthquake risk from co-seismic stress. *Nature*, 434(7031):291–291.

Melnick, D. (2016). Rise of the central andean coast by earthquakes straddling the moho. *Nature Geoscience*, 9(5):401–407.

Melnick, D., Moreno, M., Quinteros, J., Baez, J. C., Deng, Z., Li, S., and Oncken, O. (2017). The super-interseismic phase of the megathrust earthquake cycle in chile. *Geophysical Research Letters*, 44(2):784–791.

Menke, W. (2018). *Geophysical data analysis: Discrete inverse theory*. Academic press.

Michell, J. (1761). Conjectures concerning the cause and observations upon the phenomena of earthquakes. *Philos. Transact. Royal Soc. London.*, 51:2.

Montesi, L. (2004). Controls of shear zone rheology and tectonic loading on postseismic creep. *Journal of Geophysical Research*, 109(B10404):doi:10.1029/2003JB002925.

Montési, L. G. and Hirth, G. (2003). Grain size evolution and the rheology of ductile shear zones: from laboratory experiments to postseismic creep. *Earth and Planetary Science Letters*, 211(1-2):97–110.

Moore, J. D., Yu, H., Tang, C.-H., Wang, T., Barbot, S., Peng, D., Masuti, S., Dauwels, J., Hsu, Y.-J., and Lambert, V. (2017). Imaging the distribution of transient viscosity after the 2016 mw 7.1 kumamoto earthquake. *Science*, 356(6334):163–167.

Moreno, M. (2010). Active deformation in the southern andes from gps and fem models.

Moreno, M., Li, S., Melnick, D., Bedford, J., Baez, J., Motagh, M., Metzger, S., Vajedian, S., Sippl, C., Gutknecht, B., et al. (2018). Chilean megathrust earthquake recurrence linked to frictional contrast at depth. *Nature Geoscience*, 11(4):285–290.

Moreno, M., Melnick, D., Rosenau, M., Baez, J., Klotz, J., Oncken, O., Tassara, A., Chen, J., Bartaille, K., Bevis, M. G., Socquet, A., Bolte, J., Vigny, C., Ryder, L., Grund, V., Smalley, B., Carrizo, D., Bartsch, M., and Hase, H. (2012). Toward understanding tectonic contrl on the mw 8.8 2010 maule chile earthquake. *Earth Planet. Sci. Lett.*, pages doi: 10.1016/j.epsl.2012.01.006 152–165.

Moreno, M., Melnick, D., Rosenau, M., Bolte, J., Klotz, J., Echtler, H., Baez, J., Bataille, K., Chen, J., and Bevis, M. (2011). Heterogeneous plate locking in the south–central chile subduction zone: Building up the next great earthquake. *Earth and Planetary Science Letters*, 305(3-4):413–424.

Moreno, M., Rosenau, M., and Oncken, O. (2010). 2010 maule earthquake slip correlates with pre-seismic locking of andean subduction zone. *Nature*, 467(7312):198.

Muto, J., Moore, J. D. P., Barbot, S., Iinuma, T., Ohta, Y., and Iwamori, H. (2019). Coupled afterslip and transient mantle flow after the 2011 tohoku earthquake. *Science Advances*, 5(9):eaaw1164.

Muto, J., Shibazaki, B., Iinuma, T., Ito, Y., Ohta, Y., Miura, S., and Nakai, Y. (2016). Heterogeneous rheology controlled postseismic deformation of the 2011 tohoku-oki earthquake. *Geophysical Research Letters*, 43(10):4971–4978.

Métois, M., Socquet, A., and Vigny, C. (2012). Interseismic coupling, segmentation and mechanical behavior of the central chile subduction zone. *Journal of Geophysical Research: Solid Earth*, 117(B3).

Nakajima, J., Matsuzawa, T., Hasegawa, A., and Zhao, D. (2001). Three-dimensional structure of vp, vs, and vp/vs beneath northeastern japan: Implications for arc magmatism and fluids. *Journal of Geophysical Research: Solid Earth*, 106(B10):21843–21857.

Noda, A., Takahama, T., Kawasato, T., and Matsu'ura, M. (2018). Interpretation of offshore crustal movements following the 2011 tohoku-oki earthquake by the combined effect of afterslip and viscoelastic stress relaxation. *Pure and Applied Geophysics*, 175(2):559–572.

Oeser, E. (1992). *Historical earthquake theories from Aristotle to Kant*. Geologische Bundesanstalt.

Ohzono, M., Yabe, Y., Iinuma, T., Ohta, Y., Miura, S., Tachibana, K., Sato, T., and Demachi, T. (2012). Strain anomalies induced by the 2011 tohoku earthquake (m w 9.0) as observed by a dense gps network in northeastern japan. *Earth, planets and space*, 64(12):17.

Okada, A. (1960). Land deformation of the southern part of the kui peninsula, southwestern japan. *Bull. Earthq. Res. Inst*, 38:113–124.

Okada, A. and Nagata, T. (1953). Land deformation of the neighbourhood of muroto point after the nankaido great earthquake in 1946. *Bull. Earthq. Res. Inst. Univ. Tokyo*, 31:169–177.

Okada, Y. (1985). Surface deformation due to shear and tensile faults in a half-space. *Bulletin of the seismological society of America*, 75(4):1135–1154.

Oleskevich, D., Hyndman, R., and Wang, K. (1999). The updip and downdip limits to great subduction earthquakes: Thermal and structural models of cascadia, south alaska, sw japan, and chile. *Journal of Geophysical Research*, 104(B7):14965–14991.

Omori, F. (1894). On after-shocks of earthquakes. *J. Fact. Sci. Univ. Tokyo*, 7:111–120.

Ozawa, S., Nishimura, T., Suito, H., Kobayashi, T., Tobita, M., and Imakiire, T. (2011). Coseismic and postseismic slip of the 2011 magnitude-9 tohoku-oki earthquake. *Nature*, 475(7356):373.

Pacheco, J. F. and Sykes, L. R. (1992). Seismic moment catalog of large shallow earthquakes, 1900 to 1989. *Bulletin of the Seismological Society of America*, 82(3):1306–1349.

Peng, Z. and Gomberg, J. (2010). An integrated perspective of the continuum between earthquakes and slow-slip phenomena. *Nature geoscience*, 3(9):599–607.

Peng, Z. and Zhao, P. (2009). Migration of early aftershocks following the 2004 parkfield earthquake. *Nature Geoscience*, 2(12):877.

Perfettini, H. and Avouac, J. (2007). Modeling afterslip and aftershocks following the 1992 landers earthquake. *Journal of Geophysical Research: Solid Earth*, 112(B7).

Perfettini, H., Avouac, J.-P., Tavera, H., Kositsky, A., Nocquet, J.-M., Bondoux, F., Chlieh, M., Sladen, A., Audin, L., Farber, D., and Soler, P. (2010). Seismic and aseismic slip on the central peru megathrust. *Nature*, 465:10.1038/nature09062.

Perfettini, H., Frank, W., Marsan, D., and Bouchon, M. (2018). A model of aftershock migration driven by afterslip. *Geophysical Research Letters*, 45(5):2283–2293.

Peña, C., Heidbach, O., Moreno, M., Bedford, J., Ziegler, M., Tassara, A., and Oncken, O. (2019). Role of lower crust in the postseismic deformation of the 2010 maule earthquake: Insights from a model with power-law rheology. *Pure and Applied Geophysics*.

Peña, C., Heidbach, O., Moreno, M., Bedford, J., Ziegler, M., Tassara, A., and Oncken, O. (2020). Impact of power-law rheology on the viscoelastic relaxation pattern and afterslip distribution following the 2010 mw 8.8 maule earthquake. *Earth and Planetary Science Letters*, 542:116292.

Pollitz, F. F. (2003). Transient rheology of the uppermost mantle beneath the mojave desert, california. *Earth and Planetary Science Letters*, submitted.

Pollitz, F. F., Banerjee, P., Bürgmann, R., Hashimoto, M., A. A., and Choosakul, N. (2006a). Stress changes along the sunda trench following the 26 december 2004 sumatra-andaman and 28 march 2005 nias earthquakes. *Geophysical Research Letters*, 33(L06309):doi:10.1029/2005GL024558.

Pollitz, F. F., Bürgmann, R., and Banerjee, P. (2006b). Post-seismic relaxation following the great 2004 sumatra-andaman earthquake on a compressible self-gravitating earth. *Geophysical Journal International*, 167(1):397–420.

Qiu, Q. and Chan, C.-H. (2019). Coulomb stress perturbation after great earthquakes in the sumatran subduction zone: Potential impacts in the surrounding region. *Journal of Asian Earth Sciences*, 180:103869.

Qiu, Q., Moore, J. D., Barbot, S., Feng, L., and Hill, E. M. (2018). Transient rheology of the sumatran mantle wedge revealed by a decade of great earthquakes. *Nature communications*, 9(1):1–13.

Ranalli, G. (1995). *Rheology of the Earth*. Springer Science Business Media.

Ranalli, G. (1997). Rheology and deep tectonics. *Annals of Geophysics*, 40(3).

Rebischung, P., Griffiths, J., Ray, J., Schmid, R., Collilieux, X., and Garayt, B. (2012). Igs08: the igs realization of itrf2008. *GPS solutions*, 16(4):483–494.

Reid, H. F. (1910). The mechanics of the earthquake. *The California earthquake of April 18, 1906, Report of the State Earthquake Investigation Commission*.

Remy, D., Perfettini, H., Cotte, N., Avouac, J.-P., Chlieh, M., Bondoux, F., Sladen, A., Tavera, H., and Socquet, A. (2016). Postseismic relocking of the subduction megathrust following the 2007 pisco, peru, earthquake. *Journal of Geophysical Research: Solid Earth*, 121(5):3978–3995.

Rietbrock, A., Ryder, I., Hayes, G., Haberland, C., Comte, D., Roecker, S., and Lyon-Caen, H. (2012). Aftershock seismicity of the 2010 maule mw= 8.8, chile, earthquake: Correlation between co-seismic slip models and aftershock distribution? *Geophysical Research Letters*, 39(8).

Rollins, C., Barbot, S., and Avouac, J.-P. (2015). Postseismic deformation following the 2010 $m = 7.2$ el mayor-cucapah earthquake: Observations, kinematic inversions, and dynamic models. *Pure and Applied Geophysics*, 172(5):1305–1358.

Rosenberg, C. and Handy, M. (2005). Experimental deformation of partially melted granite revisited: implications for the continental crust. *Journal of metamorphic Geology*, 23(1):19–28.

Rousset, B., Barbot, S., Avouac, J., and Hsu, Y. (2012a). Postseismic deformation following the 1999 chi-chi earthquake, taiwan: Implication for lower-crust rheology. *Journal of Geophysical Research: Solid Earth*, 117(B12).

Rousset, B., Barbot, S., Avouac, J.-P., and Hsu, Y.-J. (2012b). Postseismic deformation following the 1999 chi-chi earthquake, taiwan: Implication for lower-crust rheology. *Journal of Geophysical Research: Solid Earth*, 117(B12).

Ruiz, S., Klein, E., del Campo, F., Rivera, E., Poli, P., Metois, M., Christophe, V., Baez, J. C., Vargas, G., Leyton, F., et al. (2016). The seismic sequence of the 16 september 2015 m w 8.3 illapel, chile, earthquake. *Seismological Research Letters*, 87(4):789–799.

Ruiz, S. and Madariaga, R. (2018). Historical and recent large megathrust earthquakes in chile. *Tectonophysics*, 733:37–56.

Rundle, J. B. (1978). Viscoelastic crustal deformation by finite quasi-static sources. *Journal of Geophysical Research: Solid Earth*, 83(B12):5937–5945.

Rybacki, E. and Dresen, G. (2000). Dislocation and diffusion creep of synthetic anorthite aggregates. *Journal of Geophysical Research: Solid Earth*, 105(B11):26017–26036.

Scholz, C. (1988). The brittle-plastic transition and the depth of seismic faulting. *Geologische Rundschau*, 77(1):319–328.

Scholz, C. H. (1998). Earthquakes and friction laws. *Nature*, 391(6662):37.

Schurr, B., Asch, G., Hainzl, S., Bedford, J., Hoechner, A., Palo, M., Wang, R., Moreno, M., Bartsch, M., Zhang, Y., Oncken, O., Tilmann, F., Dahm, T., Victor, P., Barrientos, S., and Vilotte, J.-P. (2014). Gradual unlocking of plate boundary controlled initiation of the 2014 iquique earthquake. *Nature*, 512:299.

Shi, Q., Barbot, S., Wei, S., Tapponnier, P., Matsuzawa, T., and Shibazaki, B. (2020a). Structural control and system-level behavior of the seismic cycle at the nankai trough. *Earth, Planets and Space*, 72(1):1–31.

Shi, Q., Barbot, S., Wei, S., Tapponnier, P., Matsuzawa, T., and Shibazaki, B. (2020b). Structural control and system-level behavior of the seismic cycle at the nankai trough. *Earth, Planets and Space*, 72(1):1–31.

Sobolev, S. V. and Muldashev, I. A. (2017). Modeling seismic cycles of great megathrust earthquakes across the scales with focus at postseismic phase. *Geochemistry, Geophysics, Geosystems*, 18(12):4387–4408.

Springer, M. (1999). Interpretation of heat-flow density in the central andes. *Tectonophysics*, 306(3-4):377–395.

Stein, R. S. (1999). The role of stress transfer in earthquake occurrence. *Nature*, 402(6762):605–609.

Stromeyer, D., Heidbach, O., and Ziegler, M. (2020). *Tecplot 360 Add-on GeoStress v2.0.* GFZ Data Service.

Suito, H. and Freymueller, J. T. (2009). A viscoelastic and afterslip postseismic deformation model for the 1964 alaska earthquake. *Journal of Geophysical Research: Solid Earth*, 114(B11).

Sun, T. and Wang, K. (2015). Viscoelastic relaxation following subduction earthquakes and its effects on afterslip determination. *Journal of Geophysical Research: Solid Earth*, 120(2):1329–1344.

Sun, T., Wang, K., Iinuma, T., Hino, R., He, J., Fujimoto, H., Kido, M., Osada, Y., Miura, S., and Ohta, Y. (2014). Prevalence of viscoelastic relaxation after the 2011 tohoku-oki earthquake. *Nature*, 514(7520):84–87.

Takeuchi, C. S. and Fialko, Y. (2012). Dynamic models of interseismic deformation and stress transfer from plate motion to continental transform faults. *Journal of Geophysical Research: Solid Earth*, 117(B5).

Takeuchi, C. S. and Fialko, Y. (2013). On the effects of thermally weakened ductile shear zones on postseismic deformation. *Journal of Geophysical Research: Solid Earth*, 118(12):6295–6310.

Tang, C.-H., Hsu, Y.-J., Barbot, S., Moore, J. D., and Chang, W.-L. (2019). Lower-crustal rheology and thermal gradient in the taiwan orogenic belt illuminated by the 1999 chi-chi earthquake. *Science advances*, 5(2):eaav3287.

Tassara, A., Götze, H., Schmidt, S., and Hackney, R. (2006). Three-dimensional density model of the nazca plate and the andean continental margin. *Journal of Geophysical Research: Solid Earth*, 111(B9).

Tassara, A., Soto, H., Bedford, J., Moreno, M., and Baez, J. C. (2016). Contrasting amount of fluids along the megathrust ruptured by the 2010 maule earthquake as revealed by a combined analysis of aftershocks and afterslip. *Tectonophysics*, 671:95–109.

Thatcher, W. (1984). The EarthquakeD eformationC ycle at the Nankai Trough, Southwest Japan. *Journal of Geophysical Research*, 89(B5):3087–3101.

Tichelaar, B. and Ruff, L. (1993). Depth os seismic coupling along subduction zones. *Journal of Geophysical Research*, 98(B2):2017–2037.

Tilmann, F., Zhang, Y., Moreno, M., Saul, J., Eckelmann, F., Palo, M., Deng, Z., Babeyko, A., Chen, K., Baez, J., et al. (2016). The 2015 illapel earthquake, central chile: A type case for a characteristic earthquake? *Geophysical Research Letters*, 43(2):574–583.

Toda, S., Lin, J., and Stein, R. S. (2011a). Using the 2011 m w 9.0 off the pacific coast of tohoku earthquake to test the coulomb stress triggering hypothesis and to calculate faults brought closer to failure. *Earth, planets and space*, 63(7):39.

Toda, S., Stein, R. S., and Lin, J. (2011b). Widespread seismicity excitation throughout central japan following the 2011 m= 9.0 tohoku earthquake and its interpretation by coulomb stress transfer. *Geophysical Research Letters*, 38(7).

Tomita, F., Kido, M., Osada, Y., Hino, R., Ohta, Y., and Iinuma, T. (2015). First measurement of the displacement rate of the pacific plate near the japan trench after the 2011 tohoku-oki earthquake using gps/acoustic technique. *Geophysical Research Letters*, 42(20):8391–8397.

Trubienko, O., Garaud, J.-D., and Fleitout, L. (2014). Models of postseismic deformation after megaearthquakes: The role of various rheological and geometrical parameters of the subduction zone. *Solid Earth Discussions*, 6(1):427–466.

Tsang, L. L. H., Hill, E. M., Barbot, S., Qiu, Q., Feng, L., Hermawan, I., Banerjee, P., and Natawidjaja, D. H. (2016). Afterslip following the 2007 mw 8.4 bengkulu earthquake in sumatra loaded the 2010 mw 7.8 mentawai tsunami earthquake rupture zone. *Journal of Geophysical Research: Solid Earth*, 121(12):9034–9049.

Tung, S. and Masterlark, T. (2018). Delayed poroelastic triggering of the 2016 october visso earthquake by the august amatrice earthquake, italy. *Geophysical Research Letters*, 45(5):2221–2229.

Van Der Elst, N. J. and Brodsky, E. E. (2010). Connecting near-field and far-field earthquake triggering to dynamic strain. *Journal of Geophysical Research: Solid Earth*, 115(B7).

Vigny, C., Simons, W., Abu, S., Bamphenyu, R., Satirapod, C., Choosakul, N., Subarya, C., Socquet, A., Omar, K., Abidin, H., et al. (2005). Insight into the 2004 sumatra–andaman earthquake from gps measurements in southeast asia. *Nature*, 436(7048):201–206.

Vigny, C., Socquet, A., Peyrat, S., Ruegg, J.-C., Métois, M., Madariaga, R., Morvan, S., Lancieri, M., Lacassin, R., Campos, J., Carrizo, D., Bejar-Pizarro, M., Barrientos, S., Armijo, R., Aranda, C., Valderas-Bermejo, M.-C., Ortega, I., Bondoux, F., Baize, S., Lyon-Caen, H., Pavez, A., Vilotte, J. P., Bevis, M., Brooks, B., Smalley, R., Parra, H., Baez, J.-C., Blanco, M., Cimbaro, S., and Kendrick, E. (2011). The 2010 mw 8.8 maule megathrust earthquake of central chile, monitored by gps. *Science*, 332(6036):1417–1421.

Völker, D., Grevemeyer, I., Stripp, M., Wang, K., and He, J. (2011). Thermal control of the seismogenic zone of southern central chile. *Journal of Geophysical Research*, pages doi: 10.1029/2011JB008247 1–20.

Wada, I., He, J., Hasegawa, A., and Nakajima, J. (2015). Mantle wedge flow pattern and thermal structure in northeast japan: effects of oblique subduction and 3-d slab geometry. *Earth and Planetary Science Letters*, 426:76–88.

Wang, K. and Fialko, Y. (2014). Space geodetic observations and models of postseismic deformation due to the 2005 m7. 6 kashmir (pakistan) earthquake. *Journal of Geophysical Research: Solid Earth*, 119(9):7306–7318.

Wang, K. and Fialko, Y. (2018). Observations and modeling of coseismic and postseismic deformation due to the 2015 mw 7.8 gorkha (nepal) earthquake. *Journal of Geophysical Research: Solid Earth*, 123(1):761–779.

Wang, K., Hu, Y., and He, J. (2012). Deformation cycles of subduction earthquakes in a viscoelastic earth. *Nature*, 484(7394):327.

Watanabe, S.-i., Sato, M., Fujita, M., Ishikawa, T., Yokota, Y., Ujihara, N., and Asada, A. (2014). Evidence of viscoelastic deformation following the 2011 tohoku-oki earthquake revealed from seafloor geodetic observation. *Geophysical Research Letters*, 41(16):5789–5796.

Weiss, J. R., Qiu, Q., Barbot, S., Wright, T. J., Foster, J. H., Saunders, A., Brooks, B. A., Bevis, M., Kendrick, E., and Ericksen, T. L. (2019). Illuminating subduction zone rheological properties in the wake of a giant earthquake. *Science Advances*, 5(12):eaax6720.

Wesson, R. L., Melnick, D., Cisternas, M., Moreno, M., and Ely, L. L. (2015). Vertical deformation through a complete seismic cycle at isla santa maria, chile. *Nature Geoscience*, 8(7):547–551.

Yamagiwa, S., Miyazaki, S., Hirahara, K., and Fukahata, Y. (2015). Afterslip and viscoelastic relaxation following the 2011 tohoku-oki earthquake (mw9. 0) inferred from inland gps and seafloor gps/acoustic data. *Geophysical Research Letters*, 42(1):66–73.

Young, T. (1807). *A course of lectures on natural philosophy and the mechanical arts: in two volumes*, volume 2. Johnson.

Yue, H., Lay, T., Rivera, L., An, C., Vigny, C., Tong, X., and Báez Soto, J. C. (2014). Localized fault slip to the trench in the 2010 maule, chile mw= 8.8 earthquake from joint inversion of high-rate gps, teleseismic body waves, insar, campaign gps, and tsunami observations. *Journal of Geophysical Research: Solid Earth*, 119(10):7786–7804.

Yuzariyadi, M. and Heki, K. (2020). Enhancement of interplate coupling after recent megathrust earthquakes. In *EGU General Assembly Conference Abstracts*, page 2550.

Zhao, B., Bürgmann, R., Wang, D., Tan, K., Du, R., and Zhang, R. (2017). Dominant controls of downdip afterslip and viscous relaxation on the postseismic displacements following the mw7. 9 gorkha, nepal, earthquake. *Journal of Geophysical Research: Solid Earth*, 122(10):8376–8401.

Zienkiewicz, O. C., Taylor, R. L., and Zhu, J. Z. (2005). *The finite element method: its basis and fundamentals*. Elsevier.

Ziv, A. and Rubin, A. M. (2000). Static stress transfer and earthquake triggering: No lower threshold in sight? *Journal of Geophysical Research: Solid Earth*, 105(B6):13631–13642.